8-2011

MIXTURE FRACTION IMAGING BASED ON PHOTODISSOCIATION SPECTROSCOPY AND TWO PHOTON LASER INDUCED FLUORESCENCE

Yan Zhao
Clemson University, zhao2@clemson.edu

MIXTURE FRACTION IMAGING BASED ON PHOTODISSOCIATION SPECTROSCOPY AND TWO PHOTON LASER INDUCED FLUORESCENCE

A Dissertation
Presented to
the Graduate School of
Clemson University

In Partial Fulfillment
of the Requirements for the Degree
Doctor of Philosophy
Mechanical Engineering

---

by
Yan Zhao
August 2011

Accepted by:
Lin Ma, Committee Chair
Donald Beasley
Richard Miller
Chenning Tong

Abstract

The study of turbulent combustion calls for new diagnostics that can measure multidimensional mixture fraction under a wide range of flame conditions. A laser diagnostic technique based on photodissociation spectroscopy (PDS) is proposed to address this need. This thesis describes the concept of the PDS-based diagnostic, reports its experimental demonstration in a non-premixed jet flame, and assesses its performance and applicable range. The two-photon laser induced fluorescence (TPLIF) technique used in conjugate with the PDS is analyzed numerically in line and planar imaging configuration.

The new mixture fraction imaging technique is centered around the creative use of photodissociation (PD) for flow visualization. A carefully chosen PD precursor is seeded into the flow of interest to measure mixture fraction. The precursor is chosen such that 1) both the precursor itself and the products formed from the precursor (if it reacts) can be completely and rapidly photodissociated; thus one of the photofragments forms a conserved scalar and can be used to infer the mixture fraction, and 2) the target photofragment offers friendly spectroscopic properties (e.g., strong laser induced fluorescence signals and/or simple signal interpretation) so multidimensional imaging can be readily obtained. Molecular iodine (I_2) was identified as a precursor satisfying both requirements and was seeded into a carbon monoxide (CO)/air jet flame for single-shot two-dimensional imaging of mixture fraction. This demonstration illustrates the potential of the PDS-based technique to overcome the limitations of existing techniques, and to provide multidimensional measurements of mixture fraction in a variety of reactive flows.

The thesis also analyzes the imaging applications of TPLIF, which is a promising technique in the planar imaging of mixture fraction. Models are developed based on rate equation approximations

and Monte Carlo simulation, with a focus on the effect of amplified spontaneous emission (ASE) on TPLIF signal interpretation. Results obtained are expected to also enhance the accuracy and applicable range of TPLIF technique in other flow imaging applications, beyond the mixture fraction imaging considered in this research.

Acknowledgements

I owe my deepest gratitude to my supervisor, Dr. Ma, who really brought me up to this level. His encouragement, guidance and support, both in academics and personal life, are greatly appreciated. I would like to thank Drs. Chenning Tong, Richard S. Miller and Donald Beasley for serving on my advisory committee.

I would thank all of my colleagues in Dr. Ma's group, with whom I learned through stimulating discussions. They are Dr. Weiwei Cai, David Ewing, Xuesong Li and many others. I would like to show my gratitude to my colleagues in the Department of Mechanical Engineering, Jian Cai, Guang Feng, Jie Kou, and many others for invaluable discussions. They made my life in graduate school much more enjoyable.

I am greatly indebted to my family, to my parents for their expectations that shaped my dream, and to my wife for her support throughout these years. Better days are yet to come.

Table of Contents

Table of Contents (Continued)

Page

List of Tables

Page

List of Figures

Page

Chapter 1

Introduction

1.1 Motivation

Turbulent combustion drives our world today. According to Ref. [1], 86% of the total worldwide energy consumption was derived from the combustion of fossil fuels in 2004, mostly under turbulent conditions. The reliable modeling and the optimal design of such combustors rely heavily on the fundamental turbulent combustion theories. Unfortunately, current theories do not yet provide satisfactory science-based solutions for these engineering problems[2]. This is due to the theoretical difficulties in understanding turbulence itself and its coupling with chemical reactions, and the experimental challenges in obtaining reliable data in turbulent combustion flows. At the current stage, experimental work is extremely valuable for model development and validation, and hence for the future advances of the turbulent combustion theories. Much progress has been made during the past two decades in this research area, featured by the intimate collaboration between the theorists and the experimentalists, and by the development of a portfolio of advanced laser diagnostics [3, 4].

Laser diagnostics have enabled numerous advancements in combustion and many of them have now become standard tools, for example, Rayleigh scattering, Raman scattering and laser induced fluorescence techniques [5, 6]. In spite of their impressive capabilities, the study of turbulent combustion continuously poses new challenges, where spatially- and temporally-resolved measurements are desired [3, 4]. One notable example is the measurement of two key quantities, the mixture fraction and the scalar dissipation rate, which describe the mixing status in turbulent flame and the coupling between the chemical reaction and the turbulence. Various techniques have been developed to measure these two quantities in turbulent flames, since they were set as research priorities for theoretical advances in the early 1980s [7]. For the mixture fraction measurement at a spatial point or along a line, there are relatively mature diagnostics yielding valuable statistics [8-12]. However, for the planar imaging of the mixture fraction, where the spatial structure of the turbulent flame can be better investigated, all the existing diagnostics suffer certain limitations [13-20].

In this work, a novel flow visualization technique for combustion flow is proposed, stressing its potential for circumventing several critical limitations of previous planar imaging techniques for the mixture fraction [21, 22]. To facilitate the discussion in later chapters, the next two sections are devoted to the basics and backgrounds on the laser light scattering techniques and on the concept and diagnostics of the mixture fraction in combustion flows, respectively.

1.2 Laser light scattering techniques

Laser light scattering techniques are widely used for flow imaging purposes[3, 4, 23, 24]. In such experiments, a laser sheet with sub-millimeter thickness at selected wavelength is used to illuminate the target flow, and various scattering signals can be collected at the 90-degree angle to

infer flow properties. Three laser light scattering techniques commonly used for species concentration imaging are briefly reviewed in this section. They are Rayleigh scattering, Raman scattering and laser induced fluorescence (LIF).

Rayleigh scattering describes the elastic scattering of photon from atoms, molecules, as well as particles with diameters much less than the wavelength of the incident light [24]. A classical picture is usually sufficient to explain this phenomenon: the electrons in the atoms, molecules and small particles are forced to oscillate by the external electromagnetic field, radiating like dipole "antennas". Therefore, the “radiated” or scattered light appears at the same time instance and wavelength as the incident light, i.e. the process is instantaneous and elastic. Because the scattered signals from different species are indiscernible, the Rayleigh scattering technique is only capable of measuring the total number density of the molecules in a flow, provided that the species composition and the scattering cross-sections of all species are known. Rayleigh scattering is also often used to measure the flame temperature [25], under the assumption of inverse relationship between the number density of molecules and temperature under ideal gas law.

In contrast, Raman scattering is inelastic, i.e., the incident photons exchange energy with the scattering molecules and change the wavelength. Based on the mode of energy exchanges, there are vibrational and rotational Raman scatterings. Vibrational Raman scattering is usually used for species-specific measurements in flames, because the wavelength shift of the signal is specific to the chemical bonds and symmetry of molecules, and the signals are easily separable for different major species in the flame [23]. Despite this advantage over Rayleigh scattering, the scattering cross section of vibrational Raman scattering is roughly three orders of magnitude smaller than

that of Rayleigh scattering. Therefore, in practice, dedicated equipments are required to detect the weak Raman signal and to suppress all possible interfering signals [26].

As oppose to the above two instantaneous scattering phenomenon that happen at all incident laser wavelengths, LIF is not instantaneous and happens only when the incident laser wavelength is tuned to a specific transition of the target atom or molecule [27]. In such a process, the atom or molecule is pumped to an actual excited energy level, where it may persist for a finite time before the molecule emits a photon and decays to a lower energy level, a process called *spontaneous emission*. In two-photon absorption LIF (TPLIF), the *spontaneous emission* may be amplified strongly enough to cause interference, which will be the focus of Chapter 4. Other fates of the excited state are possible, for example, a non-radiative transition to another energy level through collisional energy transfer. Such a process is called *quenching* and is the major complication in the quantitative LIF signal interpretation. As a method capable of species-specific measurement, LIF is usually preferred compared to Raman scattering due to its much higher signal.

1.3 Mixture fraction and its diagnostics

Chemical reaction occurs only when the fuel and the oxidizer are mixed on the molecular level. In a non-premixed or a partially premixed flame, a progress variable for such mixing is defined as mixture fraction (ξ). Intuitively, mixture fraction can be viewed as "the fraction of fuel" at a certain location, imagining that the fuel is not reacted at all. Combining the spatial derivative of mixture fraction and the molecular diffusivity at a certain location, the local scalar dissipation rate (χ) can be calculated. The scalar dissipation rate defines a characteristic diffusion time scale imposed by the mixing field [28]. Through these concepts, the effects of turbulent mixing and chemical reactions on the local thermo-chemical state, i.e., the local species composition and

temperature, can be separated. Such separation is critical in turbulent flame modeling. Both the laminar flamelet paradigm and the conditional moment closure paradigm for the numerical simulation of non-premixed turbulent flame are built upon the concept of mixture fraction [2]. In the stationary laminar flamelet model, flame reaction zones are assumed to be thin, such that a pre-calculated database of temperature, composition, reaction rates mapped over mixture fraction under certain strain rate can be used to obtain the closure for turbulent-chemistry interaction. The strain rate is related to scalar dissipation rate. In the CMC model, quantities involved in the turbulent modeling are all conditioned over mixture fraction. Therefore, the concepts of mixture fraction and scalar dissipation hold the central position in turbulent combustion modeling. There is a strong motivation for advanced laser diagnostics regarding these two parameters.

From the experiment point of view, mixture fraction is usually not a naturally existing quantity in the flames. It can be defined using the mass fraction of one or several elements originating from the fuel stream [7, 29]. One definition frequently used in the literature is that of Bilger's [7]:

$$\xi_{Bilger} = \frac{\frac{1}{2}\frac{Z_H}{W_H} + 2\frac{Z_C}{W_C} - \frac{Z_O - Z_{O,ox}}{W_O}}{\frac{1}{2}\frac{Z_{H,f}}{W_H} + 2\frac{Z_{C,f}}{W_C} - \frac{Z_{O,f} - Z_{O,ox}}{W_O}} \tag{1.1}$$

where Z is the mass fraction of a species, W the molecular weight. Subscript *ox* and *f* denote the oxidation stream and the fuel stream, respectively and subscript H, C, O denote corresponding elements. It is assumed that no C and H related species exist in the oxidizer stream. More generally, any conserved scalar β, which is free from the chemical reaction source term, can be normalized to define the mixture fraction, such that it has a value of 1 in the pure fuel stream and 0 in the pure oxidizer stream:

$$\xi = \frac{\beta - \beta_{ox}}{\beta_f - \beta_{ox}} \tag{1.2}$$

Together with the scalar dissipation (χ), which is defined through the spatial derivatives of mixture fraction, they hold the central position in non-premixed turbulent combustion theories [2, 28].

Measuring the mixture fraction in a flame is challenging. Following the Bilger definition, essentially all major species in the flame have to be measured. In a methane/air flame, for example, the simultaneous measurement of at least five species (CH_4, CO_2, CO, H_2O and H_2) is required in order to obtain reasonably accurate results for the mixture fraction. Following this approach, successful measurements have been demonstrated for point and line imaging in turbulent hydrogen flames [30] and methane flames [10], using the combined Raman/Rayleigh/CO-LIF technique. More recently, the addition of cross-planar imaging of OH radical enabled an estimation of three dimensional scalar dissipation[12]. This method still represents the most accurate measurement for mixture fraction.

The planar imaging of mixture fraction yields richer information on the spatial structure of turbulent flame than the line imaging. The interaction of turbulence and chemical reaction can be better studied with such information, for example, the extinction and reignition process. Unfortunately, the combined Raman/Rayleigh/CO-LIF technique cannot be extended to planar imaging. The prohibiting difficulties include the inherent low signal level of Raman scattering and the need to imaging all major species containing C and H simultaneously on a single shot basis. Several planar imaging attempts were made to circumvent these difficulties, but all with limited success. They are summarized here into two categories:

Methods in the first category measure the naturally existing species in the flame as in the line imaging, but seek a conserved scalar other than mass fraction of elements to define the mixture fraction. In order to avoid imaging multiple scalars, Starner et al. [13] suggest a conserved scalar based on the fuel enthalpy assuming a one-step chemistry and equal Lewis number:

$$\xi_{2-scalar} = \frac{Y_{fuel} + (c_p T - c_{p,2} T_2)/q}{Y_{fuel,1} + (c_{p,1} T_1 - c_{p,2} T_2)/q} \tag{1.3}$$

where, Y_{fuel} is the mass fraction of fuel species, c_p is heat capacity, q is the lower heat of combustion per unit mass of fuel, and subscripts *1* and *2* designate the fuel and oxidizer streams, respectively. The method is sometimes called the "two-scalar" method, in which the fuel concentration field and the Rayleigh scattering signal field are used to infer mixture fraction. A third scalar, the N_2 concentration filed, can be added to increase the accuracy near the stoichiometric mixture fraction [19]. Although the method has attracted many research efforts, the underlying one-step chemistry assumption usually cannot be satisfied especially near the stoichiometric contour, and is invalid in the presence of local extinction. Also, the use of Raman scattering for the fuel concentration measurement causes several limitations: 1) only weak signal level is available even with powerful laser; 2) it is not applicable to less Raman friendly fuel types.

The state-of-art diagnostic in this category is the "three-scalar" method demonstrated by Frank et al.[16]. In this method, the two-step chemistry assumption ameliorates the previous over-simplified chemistry with the help of the newly added CO concentration field. The conserved scalar is constructed as:

$$\xi_{3-scalar} = \frac{Y_{fuel} + q_2 / qY_{CO} + (c_p T - c_{p,2} T_2) / q}{Y_{fuel,1} + (c_{p,1} T_1 - c_{p,2} T_2) / q} \tag{1.4}$$

where Y_{CO} is the mass fraction of CO, q_2 is the lower heat of combustion per unit mass of CO. Also, a polarization/depolarization Rayleigh scattering technique [20] is adopted for the fuel concentration measurement. The Raleigh scattering pair and the CO two-photon LIF offer much stronger signal than that of Raman scattering. Despite these advantages, the Polarization/depolarization Rayleigh scattering scheme is restricted to symmetrical molecules, hence only to methane (CH_4) fuel, and requires optimized fuel compositions to maximize the difference between two types of Rayleigh signals [16]. It is therefore of limited applicable range. In addition, the CO two-photon LIF signal is suspected of photodissociation interference from CO_2 at high laser radiance, adding difficulties in data reduction [9].

The second category of the methods measure the concentration of a seeded inert tracer (e.g. a fuel marker such as acetone [15], nitric oxide (NO) [17] or krypton [18]) and then infer ξ using the tracer concentration field and the Rayleigh scattering field. These methods exploit the much stronger LIF signal for 2D imaging of fuel marker. The major challenge in these methods is to ensure the tracers to be truly "inert". Therefore, acetone is not a competent tracer, since it is plagued by pyrolysis, especially near the stoichiometric contour [15], a most important region of interest. By comparison, NO is found to be a viable tracer under limited conditions [17, 31]. Specifically, it is strictly restricted to dry carbon monoxide-air (CO/air) flames under relatively low temperature, where NO remains passive in absence of the fast reactions with H and CH radical and free from thermal dissociation. The most successful technique in this category is based on krypton atom is demonstrated as a very promising tracer [18]. Chemically, krypton is an attractive candidate because it does not participate chemical reaction, and is foreign to the combustion flow. Therefore, it is immune to all of the shortcomings of the previously in proposed

tracers. Spectroscopically, the detection of krypton is more demanding than other tracers as it requires the two photon absorption excitation scheme at short UV wavelength. Due to the small absorption cross sections of Kr's two photon transitions [32], a relative high seeding level is needed in order to achieve reasonable signal to noise ratio. The possible distortion of the TPLIF signal due to amplified spontaneous emission (ASE) under higher seeding level is to be further studied in detail, such that high signal and low distortion can be achieved simultaneously.

In summary, most existing methods for planar imaging of mixture fraction, except for the most recently proposed Kr based method, are restricted to certain fuel conditions (fuel types and compositions) and to certain purposes (with or without extinction).

1.4 Objectives and outline of the Dissertation

The primary objective of the present research is to seek an alternative multidimensional diagnostic technique for mixture fraction that can overcome the limitations discussed in the previous section. Our studies have suggested that a new flow visualization technique, using the fragments of molecules produced by photodissociation, offers a promising perspective for imaging the mixture fraction [21, 22, 33]. To facilitate the discussion, we name the technique *photodissociation spectroscopy* (PDS). The new technique utilizes PDS to avoid using the weak Raman signal and exploit the much stronger LIF signal to enable multi-dimensional imaging measurements of ξ under expanded flame conditions. The other objective of this research is to develop a deeper understanding of the TPLIF technique, with a focus on the ASE distortion. The generation of ASE in TPLIF measurement tends to prevent imaging with simultaneously high signal and low distortion. Such analysis is expected to enhance the capability of TPLIF as a

quantitative tool for a wide range of flame and plasma diagnostics, besides the immediate relevance in mixture fraction imaging.

The rest of the work is organized as follows. In Chapter 2, the concept of the technique is first introduced, followed by detailed numerical and experimental assessments of the prerequisites and an estimation of the performance. Then in Chapter 3, the experimental demonstration is presented, and sources for the possible errors are discussed. In Chapter 4, the ASE generate during TPLIF imaging is studied numerically, using methods including Monte Carlo simulation. The final chapter summarizes the work contained within this thesis and recommends topics for further study.

Chapter 2

Concept and assessment of PDS

In this chapter, the concept of PDS technique for planar imaging of mixture fraction is first introduced. The feasibility and applicable range of the PDS technique is then analyzed using molecular iodine (I_2) as a PD precursor example. The key aspects of the new technique, in terms of its detectivity, spatial resolution, and signal strength, are assessed.

2.1 Concept of PDS technique for mixture fraction measurement

Molecules can be dissociated into fragments by absorbing photons, a process named photodissociation (PD). Such photofragments, when in atomic form, are especially attractive for imaging by planar laser induced fluorescence (PLIF) because of their strong LIF transition strength and structural simplicity. A possible approach to utilize PD for flow imaging is conceptually depicted in Figure 2-1. A precursor (molecular iodine, I_2, is used here) is seeded into the flow of interest. A laser pulse, labeled as the "PD Laser Pulse", photodissociate the precursor (and the products formed from the precursor if it reacts) into photofragments (atomic I) within the pulse duration. A target photofragment (atomic I), with attractive spectroscopic properties, then can be exploited as a tracer and imaged (e.g., via LIF as shown in Figure 2-1) to infer various

properties of the flow. Meanwhile, a Rayleigh scattering measurement can be obtained with either of the laser pulses for the imaging of the total molecular number density field, and hence the temperature. The timing scheme at the lower part of Figure 2-1 summarizes the measurement sequence and the diagnostic concept.

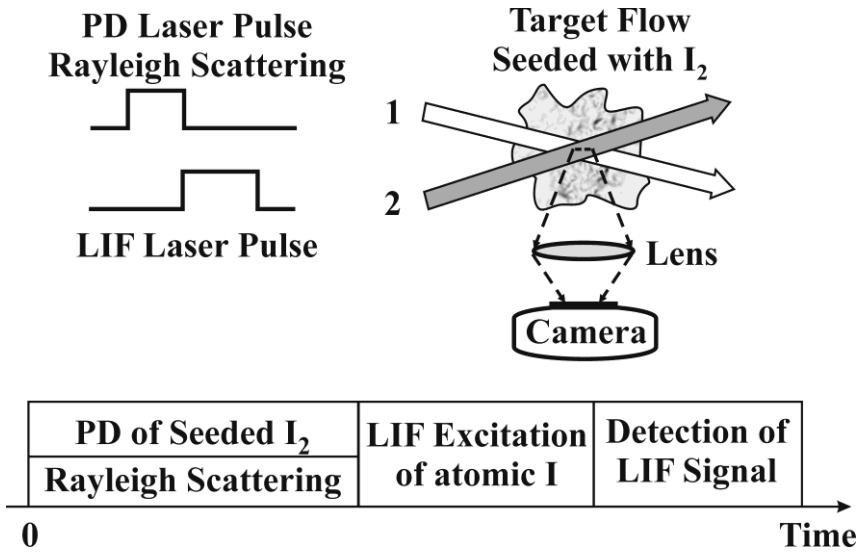

Figure 2-1. Illustration of the diagnostic concept based on PDS.

When certain requirements are satisfied, the concentration of the target photofragment forms a conserved scalar, from which the mixture fraction of the flow can be inferred. These requirements include:

1. The precursor (and the products formed from the precursor if it reacts) must be *completely* photodissociated into a single photofragment.

2. Quantitative imaging of the photofragment concentration should be possible, yielding sufficient signal-to-noise ratio (SNR).

3. Both the PD and the subsequent detection of the target photofragment must be completed within a timescale shorter than the characteristic turbulent and chemistry timescale of the flow, so that flow remains "frozen" during the imaging.

4. If the ξ derived from the target photofragment is intended to represent/approximate ξ defined otherwise (e.g., defined based on another element in the flow), the precursor and its associated products must have adequate diffusion properties. Otherwise, differential diffusion occurs and causes measurement uncertainties.

Our studies have identified two iodine species precursors, I_2 and HI, to satisfy the first two requirements under a wide range of flame conditions [21, 22, 33]. For instance, I_2 as a precursor has the desired physical, chemical and spectroscopy properties. Physically, its large vapor pressure allows a high seeding level of up to 1% volume fraction at 350 K and atmospheric pressure. Chemically, the seeding of I_2 or HI in CO/air or hydrocarbon-air flames results in only four dominate iodine-containing species: molecular and atomic iodine (I_2 and I), hydrogen iodide (HI) and methyl iodide (CH_3I). Spectroscopically, all the above iodine containing molecules can be completely photodissociated within a few nanoseconds by commercially available lasers across a reasonably large field-of-view. The pyrolysis product and photofragment, I, can be probed through a two-photon LIF scheme. The timescale for the PLIF excitation and detection is typically less than tens of nanoseconds [5]. Hence the total measurement time is mostly defined by the interval between PD and PLIF probes, which turns out to be smaller than 0.5 μs and sufficient to resolve the smallest timescale encountered in almost all turbulent flames. In the following sections, these favorable properties are examined in more detail regarding to the requirements listed above.

2.2 Assessment of iodine chemistry

In order for the photofragment iodine mass fraction to form a conserved scalar, all iodine containing molecules have to be completely photodissociated. In this section, we identify these major species to be photodissociated in representative flames. Specifically, a calculation for opposed-flow diffusion flame is performed to map out the species mole fractions throughout the flame.

A CH_4/air partially premixed flame is chosen as a representative case. The fuel composition is 25% CH_4 and 75% air seeded with 0.1% I_2, similar to the Sandia Flame series that are widely adopted for turbulent combustion study both experimentally and numerically. The OPPDIF code of the ChemKin package is used to perform the calculation under atmospheric pressure with I_2 as the seeding molecule. The reaction mechanisms used are the GRI 3.0 [34] with nitrogen chemistry omitted. Neglecting nitrogen chemistry reduces the stiffness of the system yet has no appreciable effect on the accurate prediction of the iodine species. The iodine chemistry and thermal/transport properties are adapted from previous researches where the effect of the iodine addition on flame speeds was well reproduced [35-37]. The two sets of mechanisms combined thus contain 36 species and 217 reactions for hydrocarbon chemistry, and nine species (I_2, I, HI, CH_3I, CH_2I, C_2H_5I, C_2H_3I, IO and IOH) and 60 reactions for the iodine chemistry. Due to the complexity of the chemistry, convergence of the calculation may not easily be obtained, especially when low error bounds is set in the code. The procedure of the calculation is briefly summarized here. First, a restart file is generated from a calculation without the iodine seeding. Then new calculations are performed with the restart file generated from last run as input, with successively more complicated reaction mechanisms and more strict accuracy requirements.

Convergence will be obtained in the end under the full iodine chemistry, with a relative tolerance of 10^{-6} and an absolute tolerance of 10^{-8}.

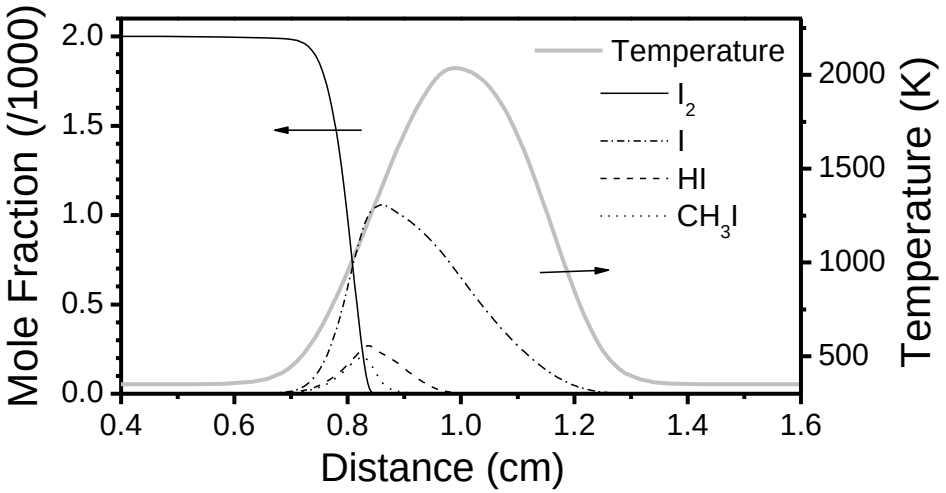

Figure 2-2. The mole fractions of major iodine containing species in a CH_4/air flame at 1 atm with an inlet temperature of 350 K, a strain rate of 40s^{-1} and an I_2 seeding level of 0.1% by mole fraction.

A set of sample results under a strain rate of 40 sec^{-1} is presented in Figure 2-2 and Figure 2-3. The major iodine-containing species are I_2, I, HI and CH_3I, consistent with the analysis given by Luo [37]. In Figure 2-2, the major species are plotted together with the flame temperature as a function of physical distance. In the fuel rich region, iodine element exists as the seeding molecule (I_2). Toward the flame front, I_2 thermal dissociation becomes significant at a local temperature of about 700 K, and completes at a temperature of ~ 1200 K. HI and CH_3I appear simultaneously with the appearance of atomic iodine at lower mole fractions, and reach their peaks both near 1300K. Further into the flame front, the fraction of atomic iodine among iodine

containing species increases and reaches to close to one at the peak flame temperature. Calculation at different strain rates and different iodine seeding levels show similar features.

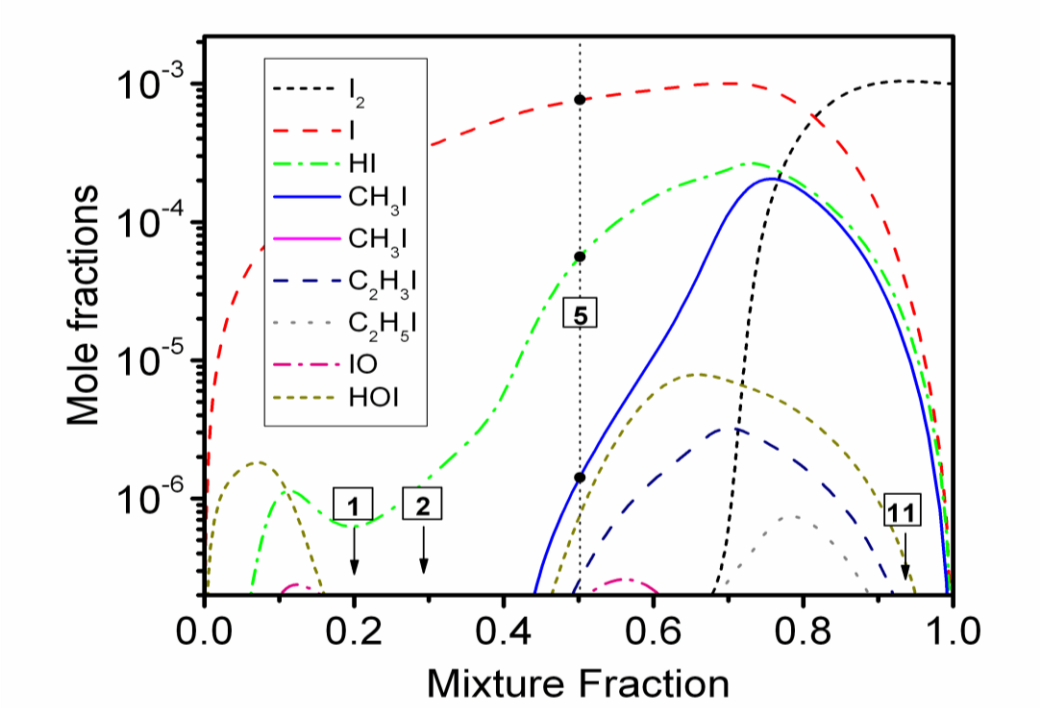

Figure 2-3. The mole fraction of all iodine containing species in log scale as a function of mixture fraction.

In Figure 2-3, all the iodine containing species are plotted in log scale to show their relative magnitudes as function of mixture fraction. The dominance of the four major species(I_2, I, HI and CH_3I) is obvious. And the five minor species altogether contributes less than 1% of the entire iodine element except at vanishingly small mixture fractions. At the left end of the mixture fraction axis, I_2 seeding is too diluted to obtain reasonable signal and is not of practical interest.

Although there are three species to be photodissociated, the dissociation may be realized with a single laser pulse at a carefully selected wavelength. In the case of our first demonstration, a

CO/air flame, the chemistry is much simpler in absence of hydrogen related species. The thermal dissociation of I_2 is the only iodine related reaction of interest and I_2 is the only species that requires photodissociation. Further analysis on this special case is presented in the next chapter.

2.3 Assessment of complete photodissociation

The key requirement in our PDS technique is the complete photodissociation of the tracer molecule and its reaction products into a single species. The target molecules to be dissociated were identified in the previous section. In this section, their favorable spectroscopic properties regarding the above requirement are discussed and evaluated. Based on an analysis of the fundamental photophysics, a numerical model is developed and validated by experiments to predict the photodissociation process. Calculations show that the complete photodissociation of these target species can be readily achieved at a large field of view for 2D imaging, with commercially available lasers.

Before the quantitative evaluation, an introduction on the background physics is necessary. Photodissociation is the process of breaking the chemical bond through the absorption of photons[38]. Before the absorption of the photon, chemical bond is formed by sharing electrons among atoms to lower the total energy of the molecule. Usually, the molecule resides in its ground state characterized by a certain electron configuration. An incident photon may excite the molecule to some excited state, changing the electron configuration. If the excited state is a repulsive (anti-bonding) state, dissociation happens rapidly within one vibrational period. The potential curves of different electronic levels provide illustrative pictures of bonding and anti-bonding states. (See state B in Figure 2-5 for an example of bonding state, while C and A' for

examples of anti-bonding states) According to the above description, the efficient photodissociation relies on two properties: the existence of the repulsive excited state(s) and the high probability of absorbing the excitation photons, i.e. a large absorption cross section. The three iodine containing target spices under consideration, I_2, HI and CH_3I, all have repulsive states easily accessible with UV excitation, and all with appreciable absorption cross sections. I_2 even has repulsive states accessible under visible wavelength excitation. In the following texts, these favorable properties are discussed in more detail for I_2 and HI respectively, under three common laser wavelengths: 532 nm in the visible range, and 266 nm and 248 nm in the UV range. They corresponds to the second and the fourth harmonic output of ND:YAG laser, and the output of KrF excimer laser, respectively. The scenario for CH_3I is very similar to that of HI due to the similarity between the H- and C_3H-bonding partners.

2.3.1 Photodissociation of I_2 at 532 nm

The unique feature of I_2 electronic levels offers the possibility of efficient photodissociation at the visible wavelength, which is analyzed below starting from an introduction of the I_2 electronic structures.

Molecular iodine has broad absorption bands in both the visible and UV wavelength range, as shown in Figure 2-4. In the visible, significant PD starts around 700 nm, peaks at 533 nm, and extends to ~ 422 nm [39]. In the ultraviolet (UV), PD of I_2 has been demonstrated at 193 [40] and 266 nm [41]. The electronic states of I_2 responsible for these absorptions are denoted by a four digits number and the term symbol following Mulliken [42]. The electronic configurations of these valence states are described as: $\sigma_g^2\sigma_u^2\sigma_g^m\pi_u^p\pi_g^q\pi_u^n$, with $m+p+q+n=10$ to indicate the assignment of the last 10 electrons. Among the large number of electronic states, five of them are most relevant to the photodissociation process considered in this research, and are shown in

Figure 2-5 (Calculated according to [43]). These states are the ground electronic state denoted as 2440 $^1\Sigma 0_g^+$ (or the X state); two 532 nm accessible excited states with the electronic configuration of 2431: the repulsive state: $^1\Pi_u$.(or the A' state) and bounded states $^3\Sigma 0_u^+$ (or the B state); and the 266 nm and 248 nm accessible 1441 $^1\Sigma_u^+(1_u)$ state (or the C state).

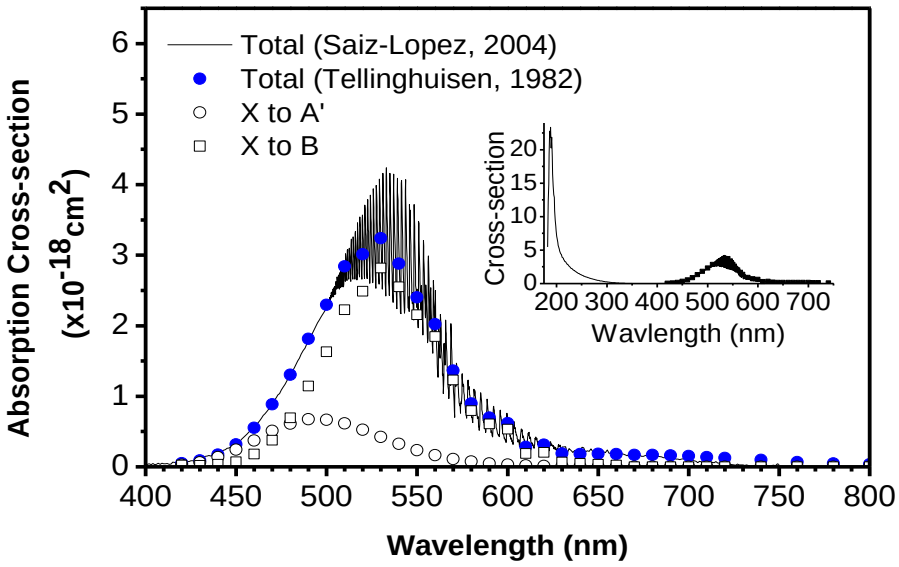

Figure 2-4.Absorption cross-section of iodine molecule and its decomposition to transitions with different upper electronic levels at atmosphere pressure and room temperature.

Two considerations motivate the study of 532 nm photodissociation. The first consideration is the simplicity of the photofragment and its subsequent probing. As can be seen from Figure 2-5, two kinds of photofragments may be generated under 266 nm PD: the ground state atom *I* ($^2P_{3/2}$) or the spin-orbitally excited atom *I* ($^2P_{1/2}$). Following literature convention, they are denoted as *I* and *I**, respectively. The relative amount of these two types of photofragments depends on the dissociation channel followed and complicates the probing and analysis of the signal. In contrast

to 266 nm PD, only I atoms are produced for the dissociation through A' state, under visible light excitation. The second consideration for favoring 532 nm over 266 nm is the higher efficiency. On the one hand, the absorption cross section of I_2 is larger at 532 nm; on the other hand, the 532 nm output offers approximately ten times higher photon flux compared to that of 266 nm, for the same ND:YAG laser.

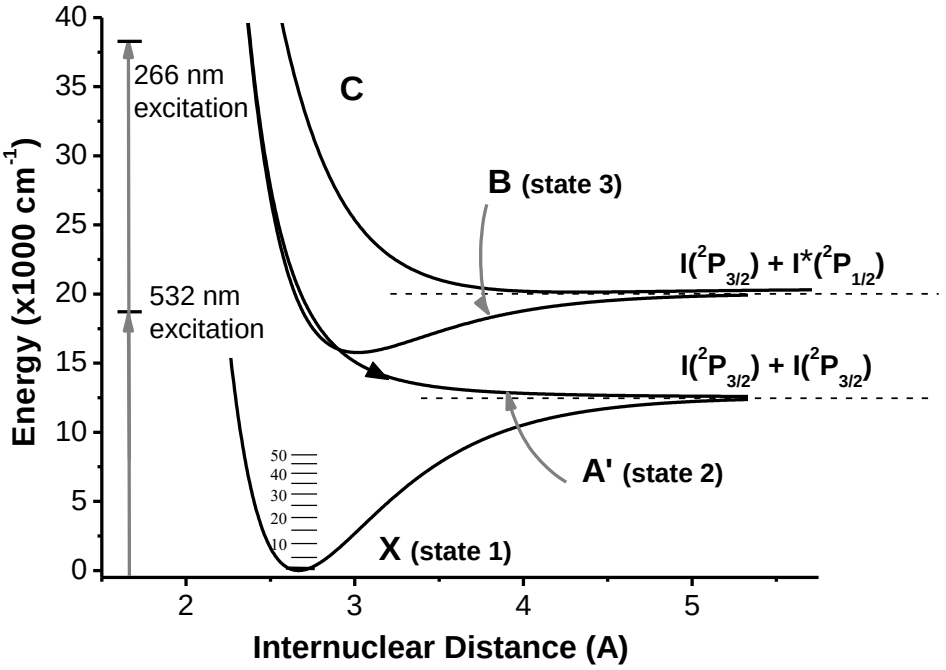

Figure 2-5. Potential curves of I_2 relevant to the PD at 532 nm and 266 nm.

Here we summarize the detailed physical process of 532 nm photodissociation, and describe a six-level model for the quantitative evaluation. Upon the absorption of a photon, I_2 molecule is excited to either the A' state or the B state [44]. For the former case, I_2 promptly dissociates into two I atoms within ~ 100 femto-seconds [45, 46]. For the latter case, the excited I_2 molecule I in the state B has multiple fates. First, since only several vibrational-rotational levels are populated,

the excited molecules are quickly relaxed into lower vibrational-rotational levels through collisions, and decoupled from the absorption/stimulated emission between the ground levels and the laser excited levels. Second, the collisional de-excitation process is companied by the broadband fluorescence, from the large number of vibrational-rotational levels in the B state toward the X state. This radiative decay is a minor channel for the depopulation of B state because of the relatively long fluorescence lifetime (~1 μs at 532 nm) of this triplet-singlet transition [47]. Third, predissociation happens when molecules are relaxed to the lower vibrational levels (near v' =6~10), where the B state crosses with A' state. Molecules may "hop into" the repulsive state and undergo fast dissociation [43]. Another fate, with much smaller possibility, of the B state molecule is the collisional induced dissociation. At higher excitation photon energy, e.g., at 515 nm excitation, this channel contributes about half of the B state dissociation, because molecules are pumped to ~3kT below the B state dissociation limit [48].

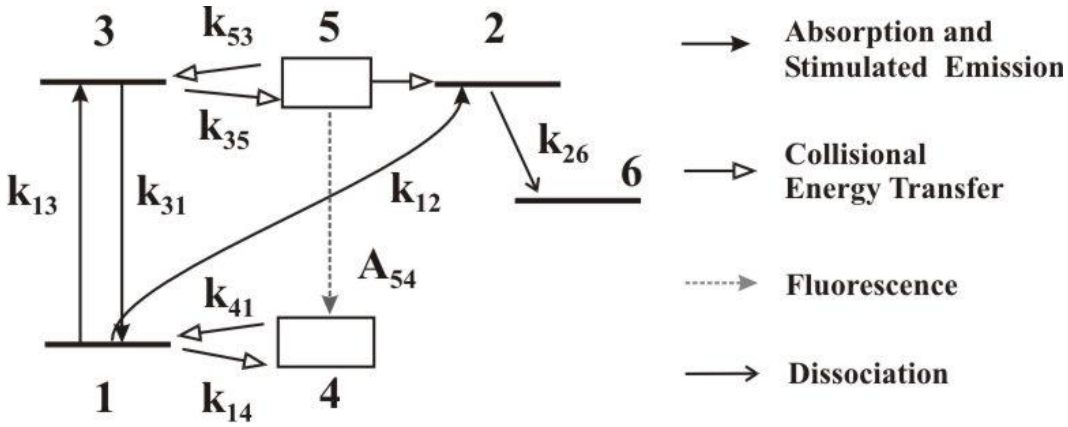

Figure 2-6. Schematics of the rate equation model for I_2 PD and LIF.

The above analysis leads to a six-level rate equation model as shown in Figure 2-6, extending our previous four-level model [21]. Compared to the previous model, the six-level model is able to explain the LIF signal from I_2 and its photodissociation at lower PD laser energies. The state 1-3 in Figure 2-6 are also noted in Figure 2-5. State 4 and 5 are the vibrational-rotational levels in the X and B states that are not directly coupled to the laser transition. These two states are coupled with the specific vibrational-rotational levels involving the laser transition through collisional energy transfer, and serve as bathing states. State 6 represent the photodissociated iodine. With the fractions of the iodine molecules or atoms on states 1 to 6 denoted as: N_1, N_2, … N_6, the following system of ODEs describes the photodissociation dynamics:

$$\begin{aligned}
\frac{dN_1}{dt} &= -\left(k_{13}+k_{12}\right)N_1 + k_{31}N_3 + k_{41}N_4 \\
\frac{dN_2}{dt} &= k_{12}N_1 - k_{26}N_2 + k_{52}N_5 \\
\frac{dN_3}{dt} &= k_{13}N_1 - \left(k_{31}+k_{35}+A_{34}\right)N_3 + k_{53}N_5 \\
\frac{dN_4}{dt} &= k_{14}N_1 - k_{41}N_4 + A_{54}N_5 \\
\frac{dN_5}{dt} &= k_{35}N_3 - \left(k_{52}+k_{53}+A_{54}\right)N_5 \\
\frac{dN_6}{dt} &= k_{26}N_2
\end{aligned} \tag{2.1}$$

with the initial conditions:

$$N_4\big|_{t=0} = 1, \text{and } N_i\big|_{t=0} = 0, \text{ where } i = 1,2,3,5,6 \tag{2.2}$$

In the calculation of fraction, two I atoms were counted as one I_2 molecule. The rate coefficients k_{ij} in sec^{-1} denotes the rate for transition from state i to state j. The rates corresponding to excitation, stimulated emission are calculated as follows:

$$k_{12} = \frac{I\sigma_{12}}{h\nu};\ k_{13} = \frac{I\sigma_{13}}{h\nu};\ k_{31} = \frac{g_1}{g_3}k_{13}; \tag{2.3}$$

where, I the laser radiance (W/cm^2); h and ν Planck constant and frequency of the transition; σ_{ab} and σ_{ac} the absorption cross-section (cm^2) for the transition from State a to b and a to c, respectively; g_1, g_2, and g_3 the degeneracy of State 1, 2, and 3, respectively. The transition from state 2 to 1 is too low, therefore k_{21} is not included into the model. For the absorption cross-sections involved, we take the total absorption cross-section measured by Saiz-Lopez et al. and decompose it into two components corresponding to two upper electronic levels following Tellinghuisen's assignment [39, 44, 49], as illustrated in Figure 2-4. The parameters estimated are: σ_{12} =4×10^{-19} cm^2 and σ_{13} = 1×10^{-18} cm^2, respectively. The absorption cross section to state 3 depends on the specific overlapping of 532 nm laser lines and the specific vibrational transition lines. However, for iodine molecule, these lines are very close at room temperature, and do not cause a significant fluctuation of the absorption across the spectrum. An overlap fraction of 0.4 is assumed to include this effect. Due to the large rotational quantum number involved in the transition at second harmonic output of ND:YAG laser, g_1/g_2 =1 and g_1/g_3=1 are assumed in our calculation[50].

For the rate of dissociation within the state A', following value is adopt according to[45, 46]:

$$k_{26} \cong 10^{13}\ \text{sec}^{-1} \tag{2.4}$$

The relaxation from a specific vibrational-rotational level is usually fast, with the rates on the order of 5×10^{-10}cm^3/s in the B state [51] and X state[52]. Under standard condition, this leads to a value of ~1.2×10^{10}s^{-1} for k_{14} and k_{35}, which is adopted for calculation in this research. From the argument of equilibrium, k_{41} and $k_{53\ \text{should}}$ assume the same value. The fluorescence transition rate, A_{54}, is taken as 10^6 s^{-1}, considering the typical B state lifetime of 1μs [47]. The rate of collisional-

induced crossing from the bathing state 5 to the repulsive state 6 can be inferred from the fluorescence quenching rate usually measured, which is ~$5\times10^{9}s^{-1}$ under 532 nm excitation [53].

To study the completeness of the photodissociation, Equation (2.1) is solved, with the following parameters to simulate a practical experimental condition. The incident laser beam used has a Gaussian temporal profile with duration of 5 ns, and top-hat spatial profile with a cross section of 0.5 mm^2. The calculation yields the temporal evolution of the population in each state. The completeness of the photodissociation is indicated by the dissociated fraction of N_6 at the end of the simulation duration. In Figure 2-7. the calculation is compared with the experiment. The solid curve represents the results of such calculation under different pulse energies of the PD laser, ranging from 0.2 to 80 mJ. The increase of photodissociated fraction is observed, reaching complete dissociation near 20 mJ. The squares points represent the normalized experimental data under the same condition, with the atomic photofragment concentration, i.e. N_6, measured using TPLIF. It can be seen that the overall trend of signal from the experiment and the calculation agrees. The saturation laser energies, representing complete photodissociation, both locate around 20 mJ. Because the photodissociation of I_2 at 532 nm is the most complicated among the cases considered in this research, such agreement also adds our confidence in numerically predicting other photodissociation processes.

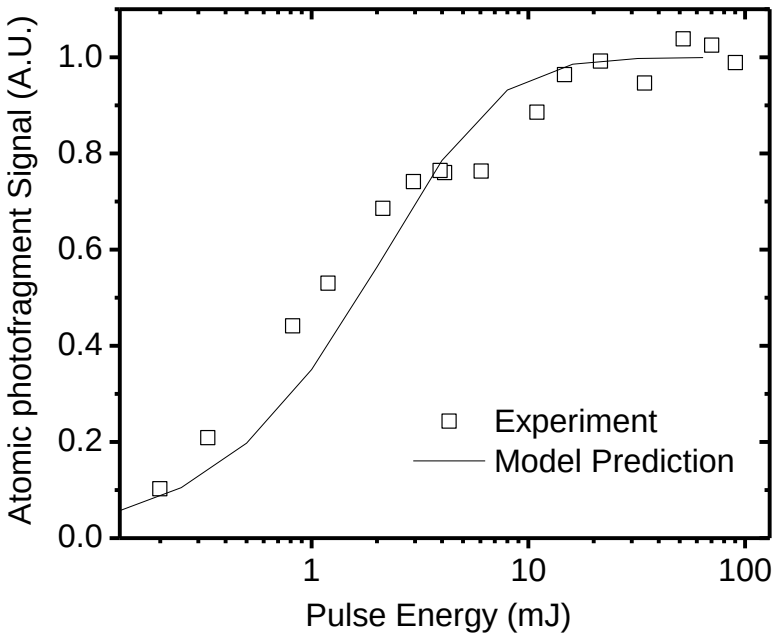

Figure 2-7. The calculated photodissociation completeness of I_2 at different pulse energies under 532 nm laser, compared with experimental data. The completeness is represented by the signal from the atomic photofragment I, measured using two-photon LIF.

Besides the photodissociation process, our model also describes the LIF phenomenon of I_2. The comparison between the model calculation and the experiment is shown in Figure 2-8. Such prediction is useful for the simultaneous imaging of I_2 LIF and I TPLIF in later chapters. Due to large absorption cross section, the LIF saturates at low laser irradiance [54]. With a laser beam cross section of ~0.05 cm^2, both our experiments and model show a linear range up to ~1mJ, and the saturation occurs afterward. The experiment and model also agree well up to ~ 10 mJ, where the model predicts a complete saturation of the LIF signal. At higher pulse energies, experiments show a steady increase of LIF signal, while model predicts a slow decrease. This discrepancy is

mainly due to the "saturation wing effect" in the experiment rather than the inability of the model. Specifically, in the practical experiment, the laser beam cross section has a Gaussian radial distribution in laser irradiance, while the calculation assumed a top hat profile. When pulse energy is further increased after saturation happens, the low irradiance wings become strong enough to produce comparable signal at the core. This is equivalent to an increased probe volume, and is the main reason for the steady increase of LIF signal observed in the experiment.

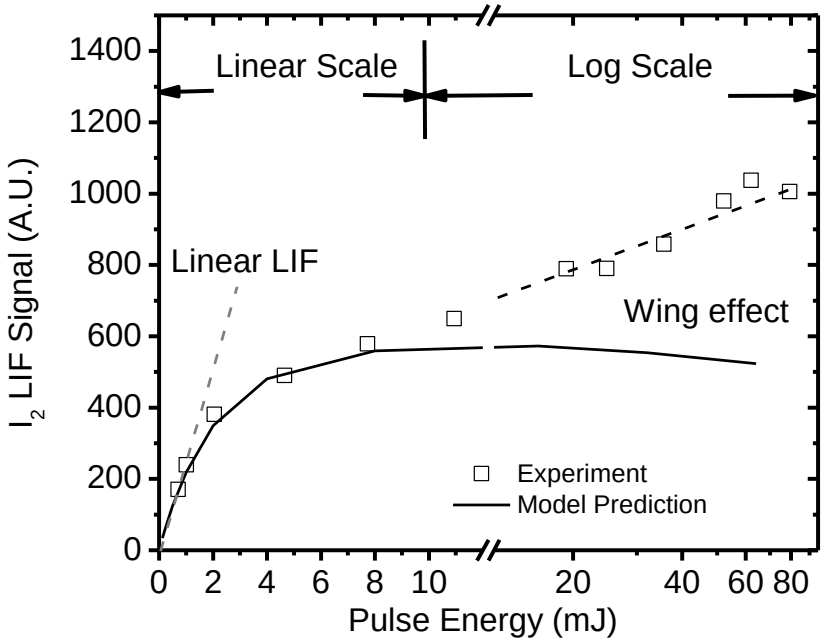

Figure 2-8. The calculated LIF signal from I_2 under 532 nm laser irradiation, compared with experimental data.

2.3.2 Photodissociation of I_2, HI at 266 nm and 248 nm

Compared to the photodissociation at 532 nm, the physics is simpler at the UV wavelengths near 248 nm and 266 nm for both I_2, HI and CH_3I. There is no bounding state but only repulsive states for all these molecules at these wavelengths, therefore a simple two level model suffices to describe the photodissociation process.

For I_2, the 266 nm and 248 nm photodissociation occurs within the first absorption continuum entering the UV regime, i.e. the C band that centers around 270 nm. Though with some controversy at the beginning, the designation of the C states was pinned down to 1441 $^1\Sigma_u^+(1_u)$ state by two experiments at 266 nm [41] and 304 nm[55]. Further into the vacuum UV, there are transitions to the bonded D state and higher Rydberg states, which do not affect the photodissociation considered in this research.

For HI and CH_3I, significant PD starts near 300 nm, reaches a maximum around 222 nm and 258 nm, respectively, and both extends to vacuum UV [56, 57]. Specifically, the first absorption continuum of HI starts from around 300 nm and peaks near 220 nm. In this so called A band, the $a^3\Pi_1$, $A^3\Pi_{0+}$ and $a^1\Pi_1$ electronic states are sequentially populated with increasing excitation photon energies. At the short wavelength end (~200 nm) of the absorption spectrum, the $t^3\Sigma_1$ state also starts to contribute. Alkyl iodide RI(R=CH_3, C_2H_5, etc) has similar photodissociation characteristics within the scope of the current research. For example, the three major states responsible for A-band absorption of CH_3I are named as $^3Q_1(E)$, $^3Q_{0+}(A_1)$, $^1Q\ (E)$, in analogy with those of HI [58]. The absorption spectrum of CH_3I is shifted for ~ 40 nm, peaking near 260 nm. The study on HI photodissociation here serves as a good example for other RI type molecules.

The repulsive excited states lead to prompt dissociation, producing two types of possible fragments, I and I^*, as discussed earlier. For I_2, the two channels are shown in Figure 2-5:

$$I_2 + h\nu \longrightarrow \begin{array}{ll} I(^2P^o_{3/2}) + I(^2P^o_{3/2}) & for \quad {}^1\Pi_u \text{ and B state predissociation} \\ I(^2P^o_{3/2}) + I(^2P^o_{1/2}) & for \quad \text{C state} \end{array} \tag{2.5}$$

and for HI, there are the following dissociation channels:

$$HI + h\nu \longrightarrow \begin{array}{ll} H(^2S) + I(^2P^o_{3/2}) & for \quad A^1\Pi_1, a^3\Pi_1 \\ H(^2S) + I(^2P^o_{1/2}) & for \quad a^3\Pi_{0+}, t^3\Sigma_1 \end{array} \tag{2.6}$$

The relative amount of I is indicated with the quantum yield, defined as $\Phi_{I^*} = [I^*]/([I]+[I^*])$. For I_2, a $\Phi_{I^*} = 0.5$ was experimentally verified [55]. For HI, extensive theoretical and experimental study exists, but a considerable spread of data remains. Experimentally, the peak $\Phi_{I^*} = 0.50 \pm 0.05$ occurs near 250 nm. At 266 nm, the wavelength of interest to the current research, the four more recent experiments give values of: 0.38 [59], 0.42[60] , 0.44[61] and 0.49[62]. Theoretically, *ab initio* investigation [56] over estimates Φ_{I^*} to be 0.56 at 266 nm, while fitting potential energy curves and transition with experimental data, a $\Phi_{I^*} = 0.41$ was reported [63]. Issues regarding I^* will be further discussed in the next section. In this section, the completeness of the dissociation is evaluated, using a rate equation description similar to the more complex six-level model in the last section.

With the above understanding on photophysics and models, Figure 2-9 summarizes the analysis for the PD of I_2 and HI at different wavelengths. These results provide the dimension of the field-of-view for imaging atomic I using different PD lasers. Here, the pulse energy is set at 500 mJ at 532 nm, 100 mJ at 266 nm and 300 mJ at 248 nm. Take I_2 photodissociation for example, for a fixed pulse energy (500 mJ per pulse) and temporal profile of the pulse, the laser radiance depends only on the cross-section area of the laser sheet. The time for 99% of the molecules to the photodissociated is denoted as $t_{99\%}$. Obviously, $t_{99\%}$ quantifies the rapidness to achieve

"complete" PD – a small $t_{99\%}$ indicates that the complete PD requires a short period of time, and vice versa. Our study shows that $t_{99\%}$ depends strongly on the laser radiance and the absorption cross-sections, and weakly on the temporal profile of the laser pulse, evidenced by the insensitivity of $t_{99\%}$ with respect to the FWHM of the Gaussian profiles used. As can be seen from Figure 2-9, $t_{99\%}$ decreases with the cross-section area of the laser sheet, due to the enhanced transition rates brought about by the increased radiance. Figure 2-9 shows that a $t_{99\%}$ of 6 ns corresponds to a cross-section area of about 3.7 mm^2 in this case. Therefore, at a typical laser sheet thickness of 0.2 mm, 99% PD of I_2 can be achieved within 6 ns across a height of ~ 18 mm using a laser with moderate power, which provides a quite large field-of-view for subsequent imaging.

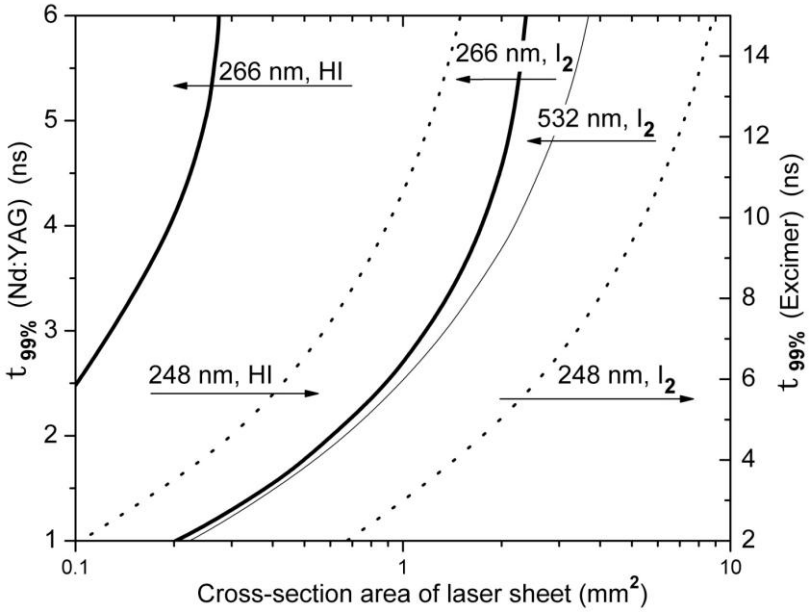

Figure 2-9. Time to reach 99% PD of I_2 and HI at different wavelengths. Temporal profile of laser pulses is assumed to be Gaussian with parameters provided by laser manufacturers.

At the wavelengths used here, the PD of HI limits this dimension. The 248 nm laser pulses offers a substantially larger field-of-view compared to that of 266 nm laser, due to the enhanced PD cross-section of HI and the increased pulse energy generated by excimer lasers than by Nd:YAG lasers. With the 248 nm laser, a $t_{99\%}$ of 15 ns corresponds to a cross-section area of 1.5 mm^2 for HI, corresponding to a height of 7.5 mm at a thickness of 0.2 mm, which provides a reasonably large field-of-view for flow visualization. Also, the 300 mJ pulse energy used here is a conservative estimation. For example, the commercially available LPXpro® series laser (Coherent Inc.) offers a maximum of 1100mJ/pulse with 10Hz repetition rate, enabling a field-of-view larger than 20 mm.

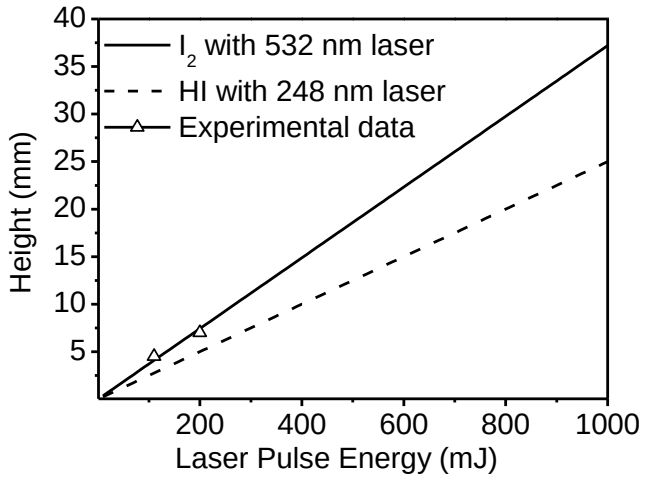

Figure 2-10. Relation between Laser pulse energy and achievable laser sheet height, assuming 0.2 mm laser sheet thickness and a pulse duration of 6 ns for ND:YAG laser or 15 ns for KrF laser. Marked data points are experimental data under two laser powers.

Based on the above discussions, the use of 532 nm ND:YAG laser is performed when I_2 alone is to be photodissociated, while 248 nm KrF laser is recommended in presence of both I_2 and HI. A relationship between the large field-of-view and laser power would be more intuitive in application, and is shown in Figure 2-10. Other parameters are the same as those in Figure 2-9. Also plotted are the two data points tested in the experiments, where the I_2 seeded in air is photodissociated with 532 nm ND:YAG laser. Good agreement is shown between the experiment and the calculation, verifying our model presented here.

2.4 Assessment of photofragment kinetics

As discussed in previous sections, there will be two possible iodine photofragments from the seeded tracer and the chemical reaction products in a hydrocarbon flame, I and I^*. However, we need the total concentration of iodine element to infer the mixture fraction. The approach to realize such conversion is discussed in this section.

One immediate possibility for evaluating the concentration of iodine element is to image both I and I^* using LIF technique with two laser pulses, respectively. Unfortunately, this approach is not only complicated but also inaccurate. Specifically, if a first pulse is used to probe I (or I^*) atom, the collisional quenched excited states would increase the concentration of I^*(or I), resulting in interference with the second pulse measuring I^*(or I). Therefore, we seek another possibility, which requires only a single imaging laser pulse and is more accurate. The essence of this approach is to utilize quenching that deactivates the I^* generated from PD before appreciable chemical reactions occur. As discussed in the previous section, the energy difference between I and I^*, 7601 cm^{-1}, is much larger than the average kinetic energy of the collisional partners

(characterized by *kT*). Therefore, collisional energy transfer happens in the I^* to I direction alone, except for the case of resonant energy transfer to be discussed later. If the nascent I^* from PD is completely quenched into I before appreciable chemical reaction consumption of iodine atoms, then a single probe of I concentration represents the total iodine element concentration. The applicability and accuracy of this approach is then determined by how these two processes compete with each other: the collisional quenching of I^* into I, and the chemical reactions from atomic iodine to iodine containing molecules. In a flame, the local quenching/reaction partners and temperature vary significantly, which makes the evaluation less intuitive. However, in order for the scheme to work, two requirements should be satisfied 1) a universal optimal delay time should exist for all possible compositions and temperatures across the flame; 2) the error caused by the competition of I^* relaxation and I chemical removal process is small throughout the flame. Before numerically evaluating the above requirements, relevant physical backgrounds are summarized on the two aspects of the problem: the quenching of I^* and the chemical consumption of I.

Regarding the I^* quenching, ideally, the quenching from electronically excited states may be estimated from hard sphere collision rate, which far exceeds the chemical reaction rate. However, the collisional quenching rates from I^* to I are small for most collisional partners except for O_2 and H_2O, as shown in Table 2-1[64]. As a forbidden transition, the radiative decay from I^* to I also has a very long lifetime of ~0.14 s, meaning that the radiative decay is also slow[65]. The most effect transition is the quenching of I^* by ground state O_2, which is studied in detail here.

A near-resonant electronic energy transfer exists between I^* and O_2, generating an excited oxygen molecule from each collision:

$$I(^2P_{3/2}) + O_2(a^1\Delta_g) \underset{k^-}{\overset{k^+}{\rightleftarrows}} I(^2P_{1/2}) + O_2(X\,^3\Sigma_g^-) \tag{2.7}$$

with the forward reaction (k^+) being only 279 cm^{-1} endothermic and the backward reaction (k^-) representing the quenching process. The further excitation of oxygen molecule is possible through: $I(^2P_{1/2}) + O_2(a^1\Delta_g) \longrightarrow I(^2P_{3/2}) + O_2(c^1\Sigma_g)$, but with a rate that is nearly 3 orders of magnitude smaller than the above one [66]. This process is negligible because the quenching of $O_2(c^1\Sigma_g)$ back to $O_2(a^1\Delta_g)$ is usually more effective than its production. The equilibrium constant for Eq. (2.7) can be approximated by: $K_{eq} = \frac{k^+}{k^-} = \frac{3}{4}\exp(\frac{\Delta E}{kT})$ for temperatures higher than 100 K, where ΔE denotes the activation energy [67]. Due to this temperature dependence, the excitation of I back to I* produced by $O_2(a^1\Delta_g)$ is smaller at higher temperatures.

Regarding the chemical consumption of I and I^*, the dominant reaction after the photodissociation of I_2 is simply the recombination between I atoms.

$$I + I \xrightarrow{M} I_2(X) \tag{2.8}$$

Another reaction, which is one order of magnitude slower than the above process, also contributes to the recombination [64]:

$$I + I^* \xrightarrow{M} I_2(B) \longrightarrow I_2(X) + h\nu \tag{2.9}$$

The chemical reactions after HI photodissociation are more complicated, due to the generation of H radical. The H radical triggers a series of reactions, including the generation of OH through reaction between H and O_2 and the generation of H_2O_2 through reaction between H and H_2O. These additional radicals complicate the recombination between H and I photofragments. The reaction kinetics soon exceed several simple rate equations, and become difficult to track unless

using dedicated codes. Therefore, the homogeneous reactor in the ChemKin package is used to calculate the evolution of species, once the initial condition, i.e. the temperature and species concentrations right after the PD event, is known.

Based on the above understanding in quenching and chemical consumption of iodine photofragments, we now move on to the numerical evaluations. The goal is to identify an optimal delay time between PD and LIF laser pulse, such that at different locations of flame, i.e., at different mixture factions, the fraction of iodine element existing as I atom dominates. Specifically, we wish to find out the optimal delay time and quantify the dominance of ground state I atom.

The evaluation is performed again with a fuel/air composition of the Sandia flames (i.e., fuel is a mixture of 25% CH_4 and 75% air, and oxidizer is air). The iodine is assumed to be seeded in the fuel stream at a level of 0.1% (mole fraction). Based on the OPPDIF calculations presented in Section 2.2, the species concentrations, together with the temperature, such as those shown previously in Figure 2-3, are used as input for simulating the temporal evolution of I^* and I atoms under the corresponding mixture fraction. Simulations were conducted at eleven mixture fractions ranging from 0.2 to 0.95 (these chosen mixture fractions were labeled 1, 2, …14 as shown in Figure 2-3). The concentration of all species and the corresponding temperature at each chosen mixture fraction were used as the initial conditions for the simulation of the deactivation of I^* to I atoms at this mixture fraction.

Model parameter		Notes
I* quenching rate constant (cm^3/molecule·s)		
N_2	1.5×10^{-16}	Values shown are at the temperature of 300 K.
CH_4	1.0×10^{-13}	
I_2	3.1×10^{-11}	
CO_2	1.3×10^{-16}	
H_2O	2.1×10^{-12}	
I atom/O_2 equilibrium ($A/\beta/E_a$)		
$I^* + O_2 \rightarrow I + O_2(^1\Delta)$	$1.87 \times 10^{16}/-1.0/797.2$	All reaction rate constants in this work are expressed as $A \cdot T^{\beta} \cdot e^{-E_a/(RT)}$, where the unit systems for A and E_a are, respectively: A (cm^3, mole, and s) and E_a (cal/mole).
$I + O_2(^1\Delta) \rightarrow I^* + O_2$	$1.40 \times 10^{16}/-1.0/0.0$	
Other relevant reactions between iodine-containing species and O_2 (both ground and $^1\Delta$ states)		
Iodine reactions		
$I_2 + M \leftrightarrow I + I + M$	$8.240 \times 10^{13}/0.0/30300.0$	For temperature range of 800–2000 K, used in flame calculation.
$I + I + M \leftrightarrow I_2 + M$	$2.360 \times 10^{14}/0.0/-1500.0$	For temperature range of 290∼1250 K, used to fit data.
Other 59 relevant reactions concerning 9 iodine species		
Hydrocarbon reaction mechanism		
Reactions between non-iodine-containing species and O_2 ($^1\Delta$)		
I* quantum yield from photodissociation		
I_2 @ 266 nm	0.5	
HI @ 266 nm	0.38∼0.56	

Table 2-1. Constants and rate coefficients used during the calculation of iodine quenching and chemical reactions.

In the calculation, the reaction rates for the recombination reaction of I atoms into I_2 was taken from [35] and [37]. The quenching rate of I^* by O2 (i.e., Eq. (4)) was taken from [66], and the quenching rates by other species taken from [64]. All other parameters in the model were taken from past literature. In the present simulation of the kinetics, the reaction mechanisms were taken from GriMech 3.0 [34] for hydrocarbon reactions, from [35] and [37] for iodine reactions, and from [66] and [68] for singlet oxygen related reactions. GRIMech 3.0 is optimized for natural gas combustion and is therefore suitable for the simple fuels considered in the current work. These rate coefficients, constants, and mechanisms are also summarized in Table 2-1.

Several simplifications/assumptions were invoked in these simulations based on the full dynamics discussed here. First, recognizing the rapidness of the PD (within 10 ns) compared with chemical kinetics, these simulations assumed that the PD is instantaneously completed at time zero. Second, the branching ratios at 266 nm were taken to be 0.5 for I_2 and HI [63], and 0.8 for CH_3I[69]. Overestimating the branching ratios provides a conservative estimation of the accuracy. Third, the flow was assumed to be frozen during the simulation because the plateau region of interest is expected to end within a few μs. Therefore, essentially, each simulation at a chosen mixture fraction represented a closed homogenous reactor, in which the initial temperature was the temperature provided by the OPPDIF calculation. The initial I and I^* concentrations were taken to be those obtained after complete PD of the major iodine containing species (i.e., I_2, I, HI, and CH_3I, as shown for the 5^{th} chosen mixture fraction in Figure 2-3 of Section 2.2), and the initial concentrations of other species were taken as those provided by the OPPDIF calculation.

These simulations will be representative if the local species composition and temperature only depend on the mixture fraction. In reality, the local species composition and temperature depend

both on mixture fraction and scalar dissipation rates[8]. Therefore in this work, the simulations were performed at representative mixture fractions and strain rates to take the effects of scalar dissipations rates into consideration. Results at two strains rates are presented here: 40 sec^{-1} and 400 sec^{-1}. Since strain rate scales with scalar dissipation rate under the steady flamelet assumption, the low strain rate corresponds to the flame regions near equilibrium, and the high strain rate corresponds to flame regions near local extinction.

Figure 2-11 shows the evolutions of the iodine element fraction existing as I atom, obtained under the low strain rate of 40 sec^{-1}. Here, eleven simulations were conducted, each for a chosen mixture fraction. The label of evolution history lines corresponds to the mixture fraction index in Figure 2-3. As can be seen, results at all mixture fractions exhibit the plateau behavior observed in the experiments. More importantly, the plateau regions all occur in a temporal window between ~300 ns to 1 μs, because the quenching of I* into I atoms occurs at a shorter time scale than chemical reactions over a wide range of conditions (in terms of local species composition and temperature). Furthermore, in this plateau region, the fraction of the ground state I ($^2P_{3/2}$) atoms out of iodine atoms in both states (I and I*) and all possible species (such as I_2, HI, CH_3I, etc.) is actually maintained at a level close to 100%. Figure 2-12 shows the I atom fraction at a delay time of 500 ns for all 11 chosen mixture fractions. The index of points corresponds to the index of lines in Figure 2-11. The I atom fraction remains above 95% throughout, and is above 99% at the stoichiometric mixture fraction of 0.375. The reasons for such a consistent high I atom fraction are threefold. First, as discussed in earlier, the high T in flames shifts the equilibrium of reaction (2.7) towards the products (more I atoms). Second, both the fuel and oxidizer contain a relatively high level of O_2, which also help to shift the equilibrium of reaction (2.7) towards the products. Third, in flame regions (i.e., the flame front) where the O_2 level is low, the high T in these regions causes significant thermal dissociation of I_2 molecules, generating only ground state

I atoms. Furthermore, the H_2O level is high in flame regions; and H_2O molecules are also effective collisional partners to deactivate I^* into I atoms (about 10 times less effective than O_2, but 1~3 orders of magnitude more effective than other species in flame[64]). Figure 2-13 and Figure 2-14 show similar results obtained under a high strain rate of 400 sec^{-1}, close to local extinction. Again, all the chosen mixture fractions share a common plateau region in a temporal window between ~300 ns to 1 μs (Figure 2-13); and at a delay time of 500 ns, the I atom fraction remains above 96% for all chosen mixture fractions (Figure 2-14). These results suggest that the approach of imaging I atom alone is a viable and simple way of implementing the PDS for imaging concentration field across a wide range of flame conditions with good accuracy. In the particular flame configurations examined above, only the I atoms need to be imaged, at a delay time between 300 ns to 1 μs relative to the PD laser pulse; and the image of the I atoms represents the concentration field with less than 5% error over a wide range of mixture fraction and strain rate.

To further validate the numerical analysis present here, experiments under room temperature was conducted. The experimental data obtained agree well with our numerical procedure shown here, and the comparisons are presented in the next chapter that focuses on the experiments.

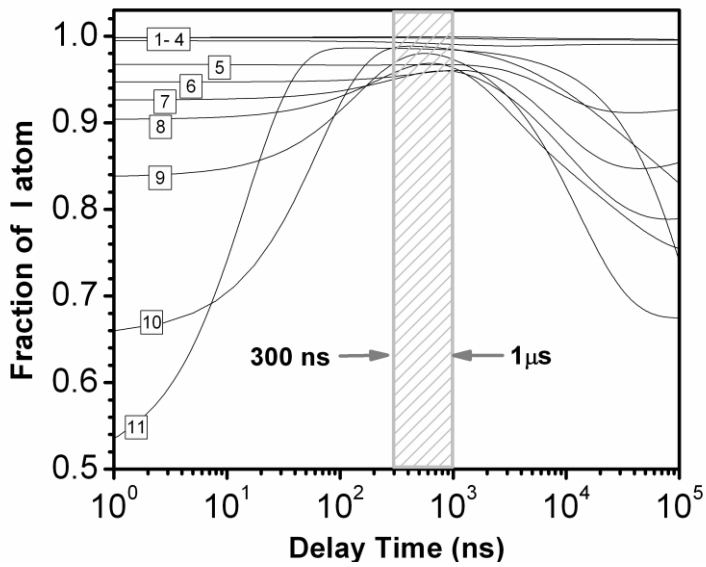

Figure 2-11. Evolution of the fraction of I atom at a strain rate of 40 s^{-1}.

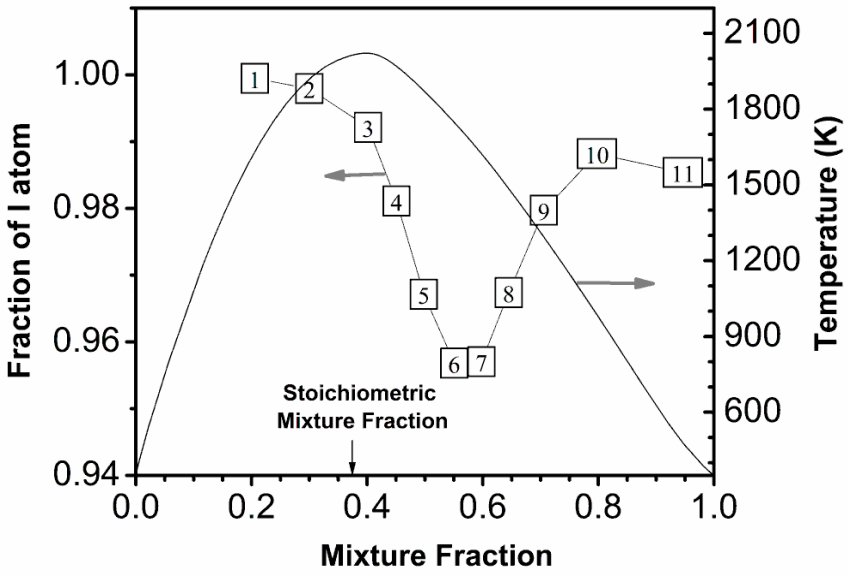

Figure 2-12. Fraction of I atom at a delay time of 500 ns relative to the PD pulse (Strain rate = 40 s^{-1}).

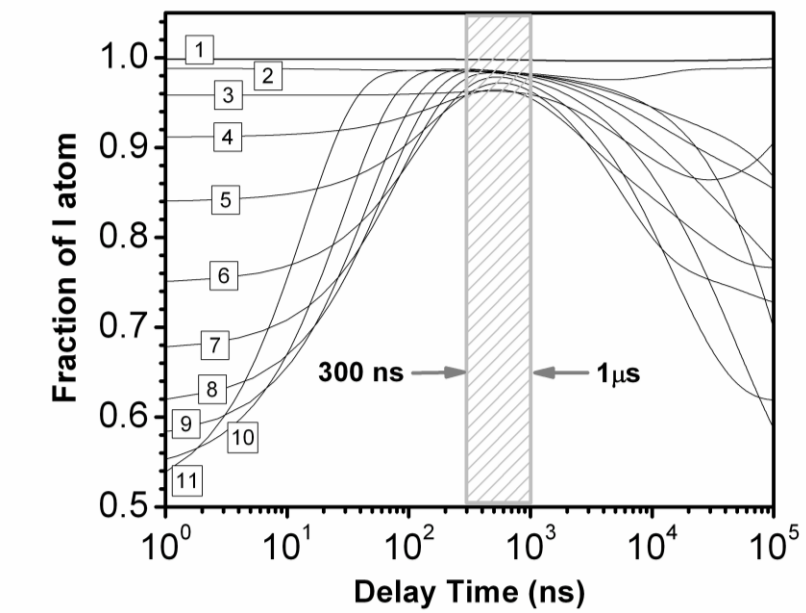

Figure 2-13. Evolution of the fraction of I atom at a strain rate of 400 s^{-1}.

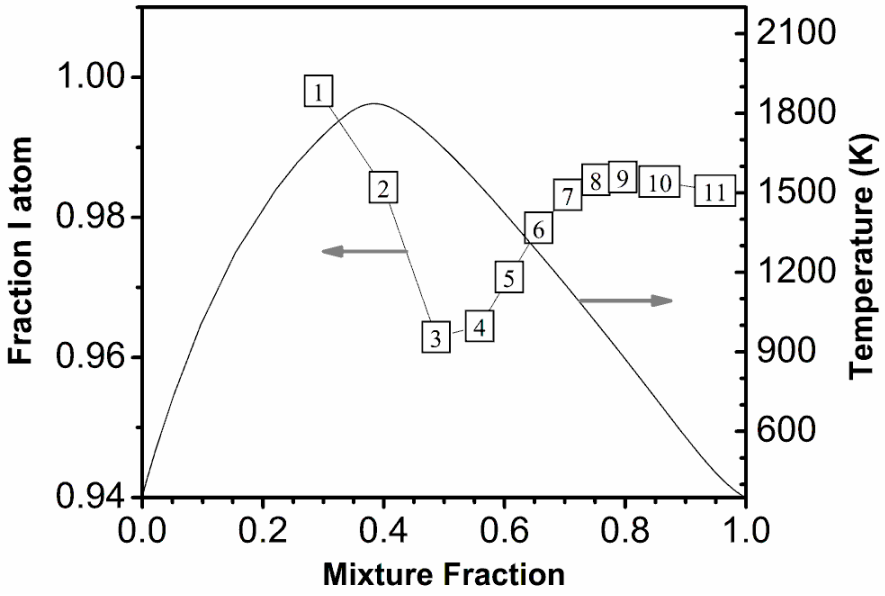

Figure 2-14. Fraction of I atom at a delay time of 500 ns relative to the PD pulse (Strain rate = 400 s^{-1}).

2.5 Assessment of photofragment imaging

This section assesses the imaging of the target photofragment, atomic iodine, generated by the PD process, in terms of the detection limit, spatial resolution, signal strength, and the size of the field-of-view. Atomic I has been detected using resonance enhanced multi-photon ionization [70], vacuum UV LIF [71] and two-photon LIF (TPLIF)[72, 73]. A survey of these techniques concluded that TPLIF provides the optimal strategy to image atomic I in practice because TPLIF avoids the use of vacuum UV wavelengths and provides a wide spectral separation between the LIF and the excitation wavelength[5].

Significant two-photon absorption transitions of I between 277 and 313 nm have been studied by Jung et al. [70]. However, the relative strengths of these transitions were not compared. For the imaging of the ground state I atom, we choose the transition from the $5p^2P^0{}_{3/2}$ state to the $6p^2P^0{}_{3/2}$ state at 298.2 nm for three reasons. First, a relatively large signal was experimentally observed at this transition [73]. Second, the fluorescence photons emitted at 804.6 nm for this transition are suitable for detection. It is widely separated with possible interference LIF signal in the visible range from other flame generated species. Third, commercial Gen III ICCD has a reasonable sensitivity at this wavelength. From the two photon excited state $6p^2P^0{}_{3/2}$, iodine atoms can further absorb a third photon, ionized into three

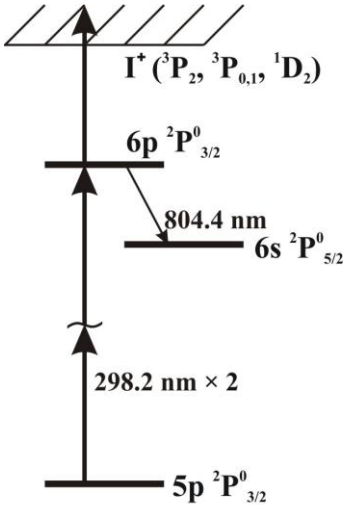

Figure 2-15. The TPLIF transition used in this research for I atom imaging.

possible singly ionized states, as shown in Figure 2-15 [70]. The other type of photofragment I^* may also be detected using TPLIF. The excitation transition from $5p^2P^0_{1/2}$ to $6p^2D^0_{3/2}$ at 306.7 nm had been used [73], giving fluorescence signals at 550.3 nm and 598.3 nm.

A summary of the TPLIF theory is provided here to facilitate the assessment. The rate at which TPLIF photons are collected by an imaging system, *R* (photons/sec), is expressed as:

$$R(T) = \eta \cdot \frac{\Omega}{4\pi} \cdot V \cdot N_I \cdot W_{2\nu}(T) \cdot \frac{A}{A+Q+W_i(T)} \tag{2.10}$$

where *T* represents time, η the quantum efficiency of the imagine system; Ω the collection solid angle; *V* the collection volume (cm^3); N_I the number density of I atoms (cm^{-3}); W_{2v} the two-photon absorption rate coefficient (sec^{-1}); *A* the Einstein coefficient for spontaneous emission from the fluorescencing state to the final state under consideration (sec^{-1}); *Q* the collisional quenching rate coefficient (sec^{-1}); and W_i the photonionization rate coefficient (sec^{-1}). Obviously, *R* directly represents the imaging signal level. Moreover, W_{2v} and W_i are expressed as:

$$W_{2v}(T) = \frac{i^2(T) \cdot \alpha_{2v} \cdot \Phi \cdot \lambda}{hc} \quad and \; W_i = \frac{i(T) \cdot \sigma_i \cdot \lambda}{hc} \tag{2.11}$$

where *i(T)* is the radiance of the excitation laser pulse (W/cm^2), $\alpha_{2\nu}$ the two-photon absorption cross-section (cm^4/W), Φ the spectral overlap function, λ the excitation wavelength length (nm), and σ_i the photoionization cross-section (cm^2). When the laser pulse exhibits a top-hat temporal profile, the radiance, *i*, remains constant during the pulse duration and is simply given by $i=E/(H \cdot t \cdot \Delta T)$, where *E* is the pulse energy (J); ΔT the duration of the laser pulse (ns); *H* the height of the laser sheet (mm). The product, $H \cdot t$, represents the cross-section area of the laser sheet (mm^2).

From geometrical optics, the following two relations can be derived for the collection angle (Ω) and the collection volume per pixel (V, cm^3):

$$\frac{\Omega}{4\pi} = \frac{1}{16 f_{\#}^2} \cdot \frac{M^2}{(M+1)^2}; \qquad V = \frac{s^2}{M^2} t; \tag{2.12}$$

where $f_{\#}$ is the lens number of the imaging system, M the magnification factor, s the pixel size of the imaging camera (μm), and t the thickness of the excitation laser sheet (mm).

The number of TPLIF photons collected per pixel is then obtained by integrating $R(T)$ over the collection time as shown below:

$$N_P = \int_{T=0}^{\Delta T} R(T) dT \tag{2.13}$$

In practice, the collection time is usually gated to be on the same length as the pulse width (ΔT) of the excitation pulse to minimize interference emission.

Finally, under shot-noise-limited detection, the signal-to-noise ratio (*SNR*) of the imaging is determined by N_p and the quantum efficiency of the CCD (η_C) as :

$$SNR = \sqrt{\eta_C N_p} \tag{2.14}$$

According to Eqs. (2.11) to (2.14), the assessment of the TPLIF imaging technique involves a series of convoluted tradeoffs. This assessment focuses on the detection limit (*SNR*), signal strength (N_P), spatial resolution (t), and size of the field-of-view (H) under a given laser and imaging configuration (i.e., fixed $i(T)$, ΔT, η, $f_{\#}$, M, and s), with a certain TPLIF transition (i.e., fixed A, σ_{2v}, σ_i, and λ) and seeding density (i.e., fixed N_I). We first examine the dependence of N_P on the thickness (t) and height (H) of the laser sheet. A small t and large H are desirable to enhance the spatial resolution and field-of-view, respectively. However, a small t diminishes the

collection volume and a large H reduces the radiance. Both effects reduce N_P, and consequently *SNR*. The assessment is further complicated by the relative magnitude of Q and W_i, as indicated by Eqs. (2.11) and (2.12) at different radiance levels.

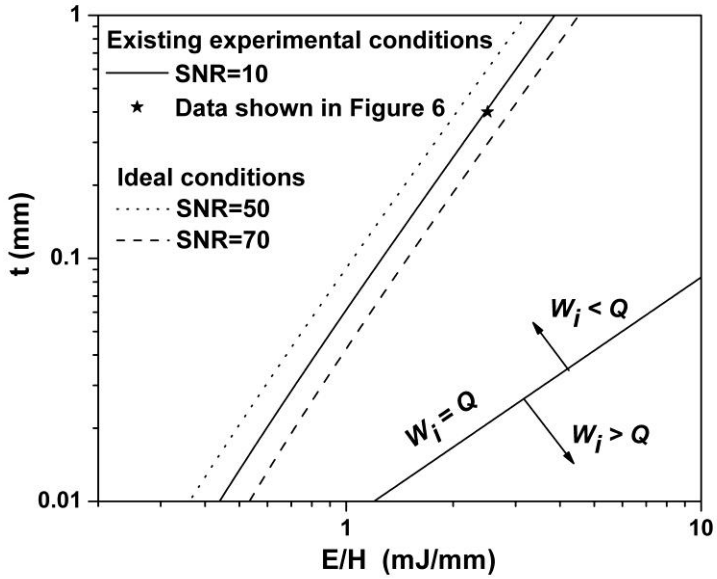

Figure 2-16. Performance estimation of TPLIF imaging of atomic I.

We found a parameterized approach effective in mapping out such intertwined relationships. To illustrate the parameterized analysis, the performance of TPLIF imaging of atomic I was analyzed in the case of a top-hat excitation pulse profile. In this case, the dependence of N_P on E and H can be grouped into the dependence on their ratio, E/H, as shown in Figure 2-16. Figure 2-16 illustrates the relationships between the spatial resolution (t), the pulse energy and the size of the field-of-view (E/H), at different signal levels (*SNR*). Parameters used for calculation are: η_{eff}=13%, Φ=0.2, N_I=2.5×10^{16} cm^{-3} (corresponding to a mole fraction of 0.1% at a temperature of 300 K), Q=5×10^{9} sec^{-1} (hard-sphere calculation at a temperature of 300 K), A=1×10^{7} sec^{-1}, α_{2v}=1×10^{-28}

cm^4/W (estimated from [73]), $\sigma_i=2.3\times10^{-18}$ cm^2 (taken from[74]), λ=298 nm, $f_{\#}$=1.4, M=1.6, s=26 μm, ΔT=8 ns. The spectral overlap function was estimated using the method described in [75] with the linewidth of the laser taken to be 0.05 cm^{-1} and the linewidth of the TPLIF transition to be 0.17 cm^{-1} [76].

Also marked in Figure 2-16 is experimental SNR in our air jet experiment, which will be presented in the next chapter together with other experimental results. As seen in the figure, the signal level agrees well with calculation shown in this chapter. However, our prediction of relative importance of quenching and ionization rates turns out to be inconsistent with experimental results. For the transition involved here, atomic I exhibits a relatively large ionization cross-section (σ_i). An experimentally fitted data (2.3×10^{-18} cm^2) from another transition is used here [74]. But this value represents a conservative estimation, because the cross section for our transition should be higher than this value according to theoretical calculations [77]. Therefore, the experiment condition should be much closer to ionization dominating region. In any case, the ionization cross section of iodine is supposed to be much larger than that of oxygen and hydrogen.

An ionization dominated experimental can potentially enable quenching free measurements, eliminating the usual complexity in LIF techniques due to the temperature- and species-dependent quenching process. Eq. (2.11) suggest that 1) the TPLIF signal (R) depends on the collisional quenching rate Q, which is difficult to determine in practice due to its dependence on both temperature and the concentrations of all collisional partners, and 2) the dependence of R on Q can be removed when the photonionization rate (W_i) dominates Q. Such dominance can be realized by increasing the radiance of the excitation laser pulse (i). However, the increase of i is practically limited by the laser equipment available, and fundamentally limited by the concern of

photochemical interference (i.e., the artificial production of the target species via photochemistry). The use of atomic I overcomes both limitations. The relatively large σ_i of atomic I renders the dominance of W_i over Q achievable at relatively low laser radiance; and the use of atomic I, a species foreign to most combustion flows, is immune to photochemical interference. Note that the above discussion assumed that the stimulated emission is negligible. When considered, the stimulated emission renders R independent of Q at a lower laser radiance than when photonionization is considered alone.

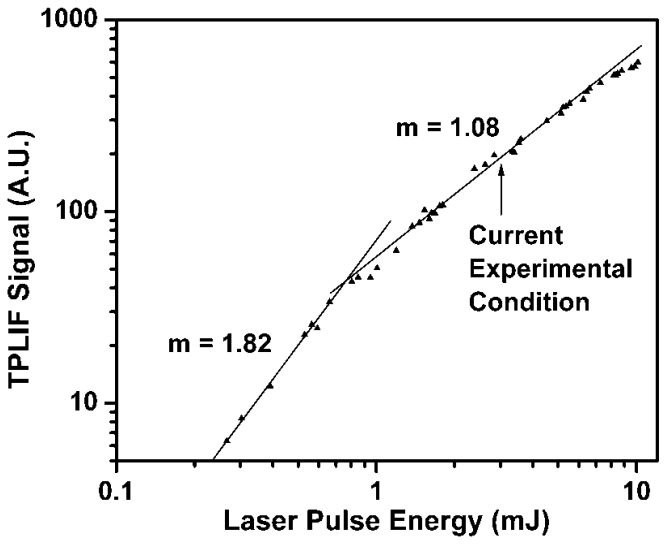

Figure 2-17. The TPLIF signal of atomic I as a function of excitation energy, indicating the feasibility of obtaining quenching-free measurements. Measurements performed at a temperature of 298K.

These discussions are illustrated in the results shown in Figure 2-17, where the TPLIF signals from atomic I are shown at various levels of the excitation pulse energy. These results were obtained using the setup shown in Figure 3-5 in the next Chapter using a steady air jet seeded

with I_2 vapor. The pulse energy of the dye laser output at 298 nm was varied from 0.25 to 11 mJ. Note that in these measurements, the laser was focused into a beam with a waist diameter of ~0.35 mm. With the size of the beam fixed, the change of pulse energy corresponded to a change of the excitation laser radiance. As can be seen from Eqs. (2.11) and (2.12), the TPLIF signal scales as i^n, with $1 < n < 2$. This trend is clearly observed in Figure 2-17, when the TPLIF signals were separated into two regions (one corresponding to pulse energy from 0.2 to 0.8 mJ and the other from 1 to 10 mJ) and were fitted to a power-law relationship. In the first region, n was fitted to be 1.82, indicating the dominance of the quenching rate; and in the second region, n was fitted to be 1.08, indicating the independence of the quenching rate. As shown in Figure 2-17, the excitation radiance falls in the quenching-free region in the imaging measurements conducted here. Therefore, no correction of quenching rate was performed for the results obtained.

From the calculation and experimental data presented in this chapter, it can be seen that with a well-chosen precursor, the PDS-based technique enables several fundamental advantages for measuring mixture fraction despite its peculiar requirements listed above. Firstly, the technique circumvents the need of monitoring multiple species simultaneously. Secondly, the target photofragment usually offers more friendly spectroscopic characteristics than species that naturally exist in flames, allowing measurement with relatively high signal strength. These advantages are generally valid for PDS-based diagnostics, and are critical advantages for the multidimensional measurements of flow properties with single-shot temporal resolution.

Chapter 3

Application of PDS for imaging mixture fraction

Having justified I_2 as a promising precursor for imaging mixture fraction, this chapter presents experimental demonstration of the PDS technique in combustion flows. First an experimental studying the iodine photofragment kinetics is presented, which further supports the numerical analysis presented in section 2.4. Then the technique is implemented first in an air jet and later in a non-premixed CO/air flame. For the air jet, instantaneous 2D images of atomic iodine concentration field in a turbulent flow are presented. Besides demonstrating the 2D imaging capability and the achievable SNR, the data obtained helped verify the numerical assessment presented in section 2.3 and 2.5. For the demonstration of the concept in an actual flame, CO/air flame is chosen due to the simple iodine chemistry involved and the readily availability of the PD laser in our lab with the required pulse energy for 2D imaging.

3.1 Experimental study of photofragment kinetics

In this experiment, the two types of atomic iodine photofragments are intentionally generated with a known fraction. Then the TPLIF signal from the I atoms is probed at various delay times between the TPLIF and PD pulses. Such measurements, as discussed in detail in Section 2.4, elucidates the chemical, PD, and spectroscopic dynamics involved in the PDS technique. Specifically, by comparing the data from controlled experiments and its corresponding simulation, the validity of the simulation approach is confirmed. Hence, the results presented in Section 2.4 for flame measurement are supported.

3.1.1 Experimental setup

The three experiments presented in this chapter share the same laser systems as shown in Figure 3-1 and Figure 3-5, respectively. Two laser systems were used to produce the PD Laser Pulse and the LIF Laser Pulse, respectively. The output at 532 nm or 266 nm from the first laser (Brilliant B Nd:YAG) acted as the "PD Laser Pulse" to photodissociate I_2 or HI, respectively. The pulse energy of the laser was up to 170 mJ at 532 nm and 30 mJ at 266 nm, respectively. The pulse duration is around 8 ns in both cases. The output at 532 nm from the second laser (Quanta-ray Nd:YAG) was used to pump a dye laser (Sirah Cobra-Stretch) to generate the LIF Laser Pulse at 298 nm. The dye laser generated pulses with energy up to 17 mJ with a duration of ~ 7 ns. The I atoms produced were imaged by the two-photon LIF (TPLIF) process as shown in Figure 2-15, with TPLIF photons emitted at 804 nm. An intensified CCD (ICCD) camera (Andor Technologies, DH734) was used to register the TPLIF photons.

Experimental details regarding the actual pulse energies used, the seeding method, the beam alignment and the collection optics differ for each of the three experiments, and are addressed in

corresponding sections. The configurations to study photofragment dynamics are described below. The forth harmonic output of the PD laser is used to photodissociate either I_2 or HI, generating both I and I^* under certain quantum yields as discussed in section 2.3. The pulse energy was maintained at ~30 mJ. The TPLIF laser is generated after a time delay relative to the PD pulse, at pulse energy of ~2 mJ which yields sufficient signal. Each laser beam was focused with a spherical lens (f =750 mm), respectively. The two beams were then crossed near their beam waists to yield a small probe volume, with a dimension of ~ 0.3 mm in the radial direction and ~1 mm in the longitudinal direction. We chose to cross the laser pulses instead of aligning them to spatially overlap. By reducing the path length of TPLIF laser beam in the PD volume, the possible SE effect can be avoided, and hence the linear relationship between the I atom concentration and the TPLIF signal can be insured. At the crossing point, the TPLIF pulse has a smaller size than the PD pulse to ensure that complete PD is achieved within the entire probed volume, and also to minimize influence of flow transport and misalignment issues. The signal is collected using the ICCD with a combination of a Zeiss lens (f/1.4, 85 mm) and a close up lens (f = 250 mm).

Accurate timing is important for this experiment. The operation of the PD pulse, TPLIF pulse, and ICCD is synchronized by a digital delay generator (DG, Berkeley Nucleonic, Model 575). The DG has a 250 ps delay resolution and 200 ps internal jitter, sufficiently accurate for the time scales involved in this work. The DG triggers the flash lamps and Q-switches of both ND:YAG lasers to control the relative delay between the TPLIF and PD pulses. Calibration experiment is performed by register the times for different lasers' arrival, using LIF/TPLIF signal at the probe location from I_2 tracer. This calibration eliminates the effect of internal delays of different equipments and laser beam travel time. Good repeatability on the pulse arrival time and duration was found on the order of 2 ns.

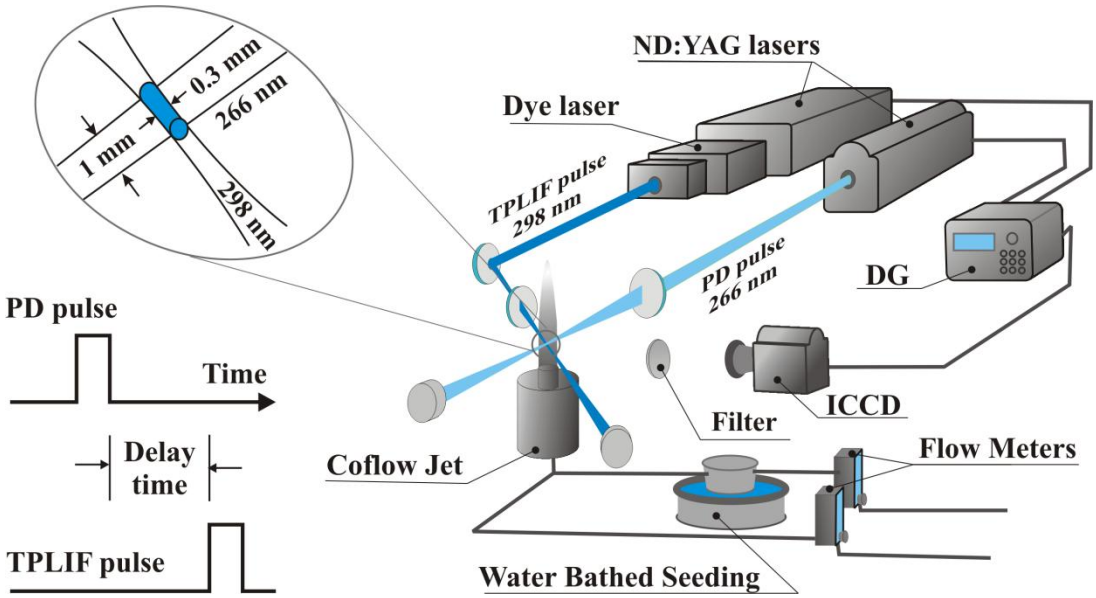

Figure 3-1 Experimental setup to study the kinetics of photofragments, I and I^*, under quenching and chemical reactions

In our experiment, the I_2 or HI molecules are delivered to the probe region by a jet flow seeded with I_2 or HI. In the case of I_2 seeding, a carrier gas (industrial nitrogen) passes through a long PTFE tube with solid iodine beads to bring the I_2 vapor into the jet. Drying agents were placed at the inlet of the tube to ensure that the incoming flow was free of water vapor to prevent forming hydriodic acid and coating the I_2 beads, which inhibits the vaporization of the beads. A particle filter was placed at the outlet of the tube to remove I_2 dust to prevent interference Mie scattering in the experiments. To enhance and stabilize the seeding level, the PTFE tube is immersed into a water bath at a constant temperature of 40 ^oC. The seeding level is adjusted by varying the flow rate of the carrier gas, and a maximum seeding level of ~0.5% (mole fraction) can be achieved in our experiments. In the case of HI seeding, the carrier gas passes through hydroiodic acid (Sigma Aldrich). Again the acid container is immersed in a water bath at 70^oC to enhance and stabilize the seeding level. Although the saturated vapor pressure of HI at this temperature is quite high, a

low level of seeding level is obtained in practice due to the azeotrope nature of the acid (mixture of HI and water), i.e., the HI and H_2O molecules evaporate with a fixed ratio. The evaporated HI and H_2O molecules quickly associate into a complex: $HI\cdot(H_2O)_4$ above the liquid surface, and the complex further aggregates to small droplets. This significantly reduces the amount of seeded HI molecules in the gaseous phase. Because of this low seeding level, the final TPLIF signal level obtained with HI seeding was 5~10× lower compared to that obtained with I_2 seeding.

As mentioned in Section 2.4, O_2 is the major collisional partner to quench I^* into I. To study the effects of this quenching process, the carrier gas was mixed with varying amounts of dry air controlled by another flow meter to adjust the mole fraction of O_2 in the jet, as shown in Figure 3-1. In particular, experiments were performed with relatively high and low O_2 concentrations. At low O_2 concentration, the flow meter for dry air was closed; but trace amounts of O_2 could still diffuse into the probed region from ambient air and this effect was taken into consideration in our model fitting. We performed experiments at a total of 33 delay times uniformly distributed in the range of zero to ~1 ms in log scale. The TPLIF photons from I atoms were measured by the ICCD camera to infer the mole fraction of I atoms, and measurements were repeated 50 times at each delay time, with both the PD and TPLIF pulses operated at a 5 Hz repetition rate.

3.1.2 Results and discussion

Figure 3-2 shows a typical set of data obtained with I_2 tracer at high O_2 concentration, in comparison with model fitting. The TPLIF signal from I atoms was measured to infer the mole fraction of I atoms using the model described in Section 2.4. As mentioned earlier, measurement of the TPLIF signal was repeated 50 times at each delay time; and both the average and the variation of these 50 measurements are shown in the following figures. The entire set of measurements at all delays times were repeated twice and shown in Figure 3-2 (labeled as

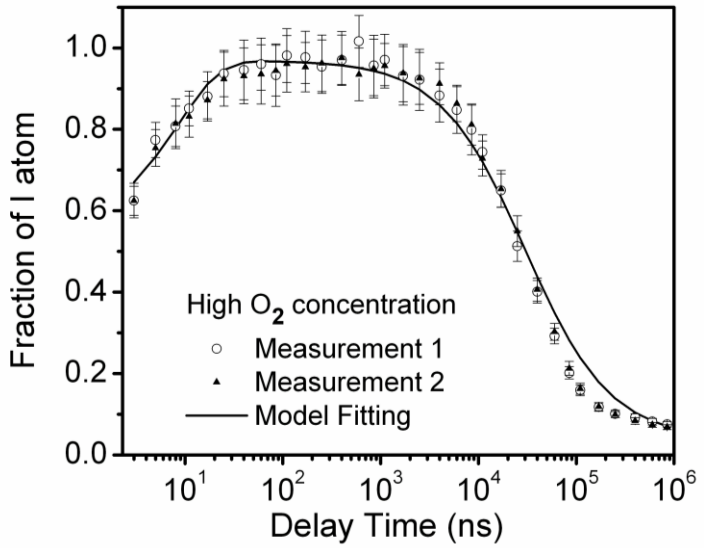

Figure 3-2. Fraction of I atoms at various delay times under high O2 concentration

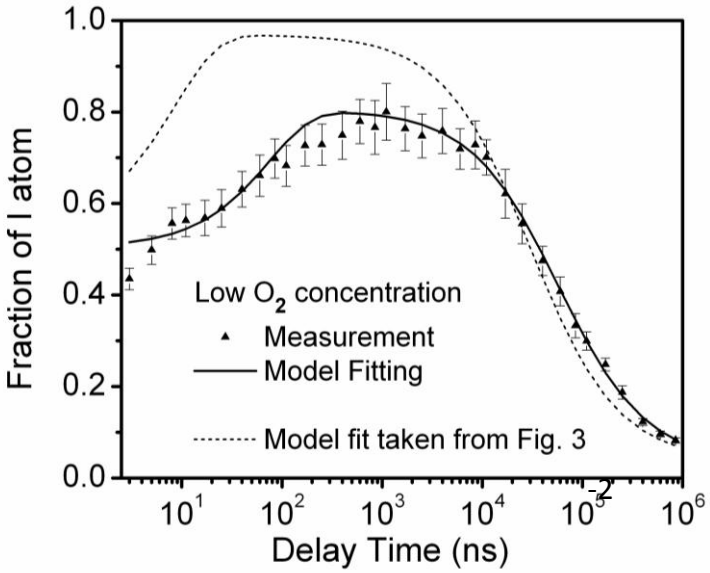

Figure 3-3. Fraction of I atoms at various delay times under low O2 concentration

Measurement 1 and 2) to illustrate the reproducibility of the measurements. Time zero is defined as the time when the PD pulse arrives at the probe volume.

Figure 3-2 elucidates the various dynamics involved in the PDS technique. At a zero delay time, the TPLIF pulse arrives at the probed volume simultaneously with the PD pulse. Therefore, the TPLIF pulse excites I atoms as they are generated by the PD process. In comparison, with an increasing delay time, the TPLIF pulse excites both the I atoms generated by the PD process and the I atoms generated by the subsequent deactivation of I^* atoms (which are also generated by the PD process), resulting in a corresponding increasing signal. The signal reaches a plateau with a delay time in the 40 to 2000 ns range, indicating that all the I^* atoms have been deactivated into I atoms after ~40 ns, but chemical reactions are not rapid enough to significantly consume I atoms until ~ 2000 ns. For these reasons, such a plateau is also observed under other experimental conditions.

Figure 3-2 also shows the best fit (in the least square sense) of the measurements using the model described in Section 2.4. Two fitting parameters were used in the model here: the O_2 concentration and the I_2 seeding level. The I^* quantum yield was taken to be 0.5 according to [41]. The fitting resulted in an O_2 concentration of 11.0% (mole fraction) and an I_2 seeding level of 0.224%. These results are in good agreement with the flow meter measurement of 11.5% for O_2 concentration and 0.225% for I_2 concentration, which confirms our model developed in Section 2.5. As can be seen from this comparison, the model accurately captures the major dynamics of the PDS. Note that the model fitting yields the mole fractions of all iodine-containing species. Based on such information, the measured TPLIF signal can be converted into the fraction of the I ($^2P_{3/2}$) atoms out of iodine atoms in both states (I and I^*) and all possible species (such as I_2, HI,

etc.), which is what Figure 3-2 actually reports. The rest of the experimental data are processed and reported in a similar manner.

As Figure 3-2 shows, there is a relatively large discrepancy between the data and the model at both short (within several nanoseconds) and long (after ~ 100 μs) delay times for several reasons. First, both the PD and TPLIF pulses have a temporal width of ~ 7 ns, resulting in a relatively large uncertainty in defining time zero at delay times shorter than a few ns. This effect is mostly responsible for the lower experimental data compared to model calculation at the first few nanoseconds. Second, the model does not consider all the physics involved during and immediately after the PD process. For instance, the nascent photofragments carry residual internal energy in the form of kinetic energy. Hence, they have a higher velocity than ambient gas molecules, resulting in a different lineshape compared to the "matured" photofragments. They also have preferred polarizations according to the polarization of the PD laser. Our model does not include these physics. However, such physics are peculiar to only the nascent photofragments, and quickly become insignificant within 1~2 ns after the nascent photofragments collide with ambient molecules [78]. Third, at long delay times, the jet flow can no longer be considered as "frozen". The flow velocity at the measurement location was ~ 70-90 cm/sec in our experiments. At a delay time of 200 μs, the fluid parcel that was photodissociated has been transported by more than ~ 0.14 mm, no longer negligible compared to the dimension of the photodissociate volume (~1mm diameter of the PD laser beam). Molecular diffusion of the photofragments also plays a comparable role as the advection at long delay times. Under our experimental conditions, the characteristic length of molecular diffusion was estimated to be 0.15 mm at a delay time of 200 μs, comparable to the 0.14 mm length scale due to advection. The molecular diffusion length scale was estimated according to a scaling law from the statistical theory, $\sqrt{\langle r^2 \rangle} = 6Dt$, where *r*

is the characteristic length of molecular diffusion, t is the delay time, and D the binary diffusion coefficient taken to be 0.3 cm^2/s. Such discrepancy was observed in other results for these same reasons.

Figure 3-3 shows a typical set of data obtained under low O_2 concentration. Model fitting yielded an oxygen concentration of 0.81%. Several observations can be noted in comparison to the case of high O_2 concentration. First, the signal rises more slowly with increasing delay time because the deactivation reaction occurs more slowly at lower O_2 concentration, confirming that O_2 is the major collisional partner to deactivate I^*. As a result, the plateau of the fraction of I atoms occurs at a different location. Second, the I fraction does not rise to 100% at low oxygen concentration. Our explanation for this is that the low O_2 concentration shifts the equilibrium of reaction (2.7) in Section 2.4 towards the reactants (i.e., less I^* atoms are deactivated). Equilibrium analysis of the reaction between I and O_2^* shows:

$$\left.\frac{[I]}{[I^*]}\right|_{Equilibrium} = K_{Eq} \cdot \frac{[O_2(X\,^3\Sigma_g^-)]}{[O_2(a^1\Delta_g^-)]} \tag{3.1}$$

where K_{Eq} respresents the equilibrium constant this reaction. Equation (3-1) suggests that a lower O_2 concentration (i.e., smaller $[O_2(X\,^3\Sigma_g^-)]$) causes the fraction of I atoms to decrease.

Experimental and model fitting of HI seeding cases are presented in Figure 3-4. The PD of HI generates H atoms, which trigger more chemical reactions than in the case of I_2 seeding. As discussed in Section 2.3, a variation in I^* quantum yield exists for HI [59-62]. Therefore, ϕ was also treated as a fitting parameter here. The model fit shown in Figure 3-4 yields, ϕ=0.5 (which is within the spread of existing data), HI seeding of 0.06% (mole fraction), and an O_2 concentration

of 6% and 0.3% for high and low oxygen cases, respectively. The data have the same trend as those observed for I_2, but the location and the peak value of the fraction of I atoms are different.

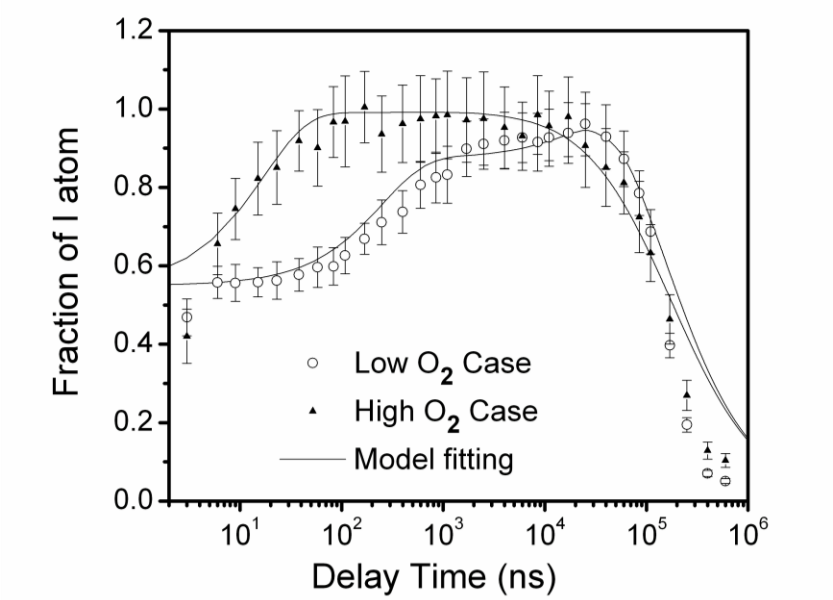

Figure 3-4. Fraction of I atoms in the case of HI seeding

Before we conclude this section, the calibration of the I atom fraction in our experiments is explained here. The I atom fraction in these experiments (e.g., in Figure 3-2 to Figure 3-4.) was calibrated differently for I_2 and HI. For the I_2 experiments, the ground state iodine fraction is calibrated by comparing the signal with that obtained with 532 nm PD laser, which generates solely ground state I atoms. However, this method does not work for HI because there is no wavelength that is able to photodissociate HI without producing I^*. Therefore, for HI experiments, the fraction of ground state iodine was calibrated by assuming the signal at a zero delay time corresponds to a quantum yield (of I^*) of 0.45 (i.e., the iodine fraction shown in Figure 3-4 at zero delay time equals 0.55).

To summarize this section, the results reported here suggest the approach of imaging the concentration of the I atoms alone to infer the iodine element concentration is possible, provided that the measurement is performed in the plateau region, i.e., the I^* atoms are effectively quenched into I. For instance, in the validation experiment in with air jet, at a delay time between 40 to 2000 ns after the PD is completed for the case of high O_2 concentration. In this plateau region, the I* atoms have been converted into I atoms but chemical reactions are not rapid enough to consume the I atoms significantly. The agreement between experiment and numerical simulation adds our confidence of applying the numerical procedure to flame conditions.

Under flame conditions, temperature and species composition change with location. Temperature comes into play through the equilibrium described in Equation (3-1). The equilibrium constant can be expressed as [66, 67]:

$$K_{Eq} = \frac{4}{3}\exp(-\frac{401\,K}{T}) \tag{3.2}$$

where T is temperature in unit of Kelvin. We expect the accuracy to improve at increasing temperatures because the equilibrium constant increases, i.e., the equilibrium shifts towards the products (I atoms) at increasing T. Species composition comes into play though the relative amount of O_2 compared to the amount of I^* generated. For the partially premixed flames considered in Chapter 2, O_2 concentration is sufficiently high for both fuel rich and air rich side of the flame. While in the flame front where O_2 concentration is low, temperature is high and I^* generated is lower due to lower amount of PD precursor. Numerical simulation in Section 2.4 provided more quantitative evaluation of accuracy in specific flame.

3.2 Demonstration of mixture fraction imaging in air jet

3.2.1 Experimental Set up

The experimental implementation of the PDS based mixture fraction imaging diagnostic using I_2 as the precursor is illustrated in Figure 3-5. Both laser pulses were transformed into laser sheets by sheet forming optics as shown, which were aligned to overlap spatially. The geometry of the two laser sheets are about 7 mm in height and 0.4 mm in thickness for the PD laser at 532 nm, and about 5 mm in height and 0.2 mm in thickness for the LIF laser at 298 nm, respectively. During the experiment, the PD pulse energy was maintain at ~170 mJ, while the LIF pulse energy was maintain at ~16 mJ. The camera was equipped with two opposed placed commercial 85 mm lens (Zeiss and Nikkor, *f*/1.4), both focusing to the infinite. This arrangement of collecting optics achieves high imaging quality in terms of MTF and high *f*/1.4 collection efficiency. The resulting 1:1 magnification leads to a 13.3×13.3 mm^2 field of view, and highest spatial resolution of 13 μm/pixel. A 2 by 2 binning was used, resulting a projected pixel size of 26.6 μm. A long-pass filter (Thorlabs, FGL780s) to block possible interference signals. The delay generator synchronized the operation of both lasers and the ICCD cameras. The delay between PD and LIF pulse was set to 500 ns. The ICCD gating was set to 100 ns, bracketing the LIF pulse.

Focusing of the lenses deserves further notes. Although commercial lenses have good achromatic correction, they are generally designed for visible wavelength range. Therefore, focusing under the visible light does not necessarily lead to the best focusing at the IR wavelength (804 nm) that we are interested in this particular research. In practice, a sharp signal is created by a knife edge that cuts in the incoming TPLIF laser sheet. Focusing is then achieved by making this edge as sharp as possible on the camera.

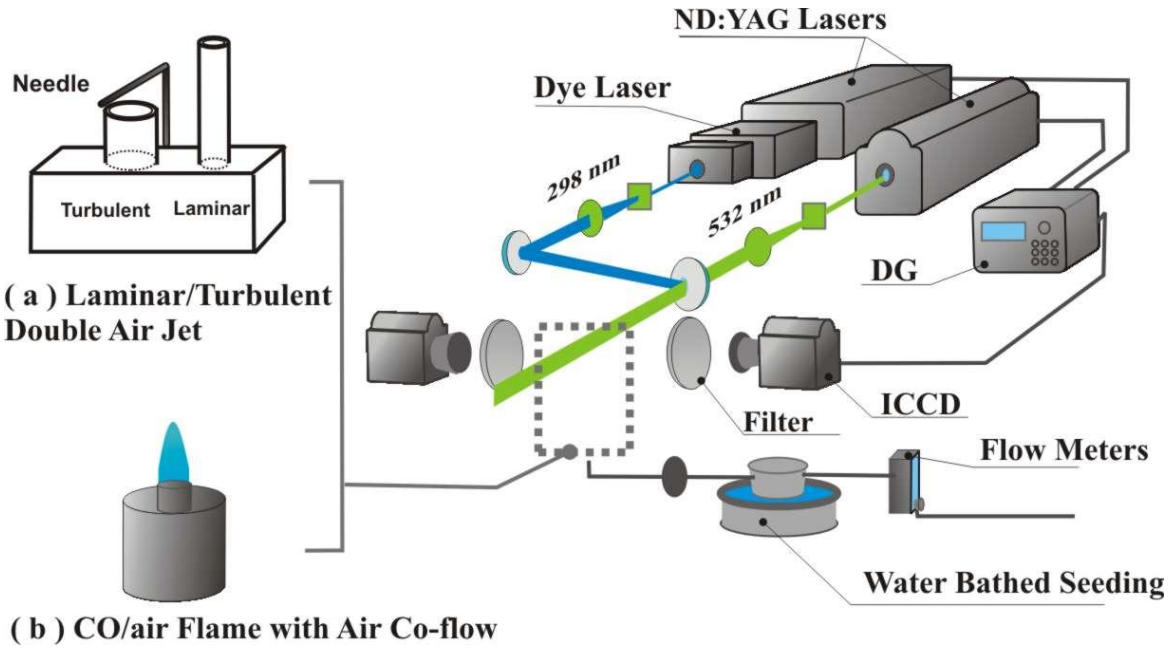

Figure 3-5. Experimental implementation of the diagnostic concept using I_2 as the percursor and atomic I as the target photofragment, for (a) air jet and (b) CO/air flame

Due to shot-to-shot variation between laser pulses, the non-uniform laser sheet profile of the LIF laser needs to be monitored and corrected *in situ*. In the demonstration experiment shown here, we adopted a simple twin jet configuration, as depicted in Figure 3-5 (a). A smaller diameter (d = 2 mm) reference jet is placed near the main jet (d = 4.6 mm) that we are interested in, with a 6 mm distance between their center lines. With this configuration, part of the laminar jet flow with a uniform distribution of the tracer is imaged into each image of the turbulent jet flow, which serves to correct the laser intensity on a shot-to-shot basis. A needle is placed right above the main jet exit to disturb the flow. The turbulent wake is imaged about 1 cm above the main jet exit. The flow rate is changed to observe different level of turbulence.

3.2.2 Data processing and noise reduction

Mixture fraction can be constructed through a conserved scalar, recalling the definition in Eq. (1.2). The conserved scalar β in our case is the local mass fraction (Y_I) of the iodine element. Because there is no iodine containing species in oxidizer stream, the mixture fraction takes the form of $\xi = Y_I / Y_{I,f}$, where subscript *I* and *f* denote the *iodine* and *fuel stream*, respectively.

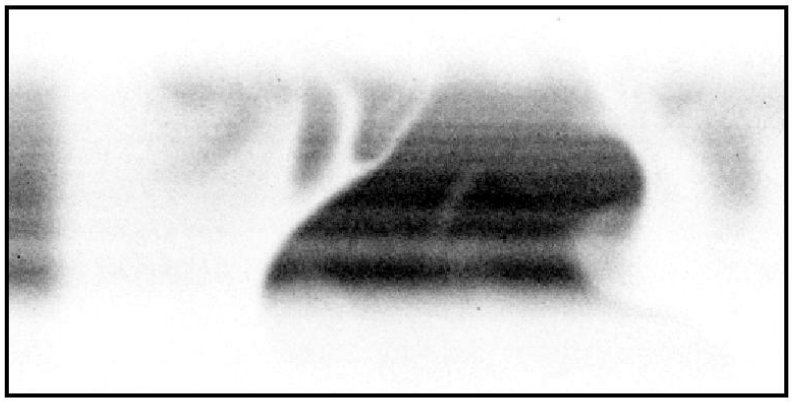

Figure 3-6. A sample raw image of mixture fraction at ~1 cm above the air jet.

The calculation of mixture fraction is straightforward for the air jet experiment. In this case, the mixture fraction, defined through the mass fraction of iodine element, equals to the iodine mole fraction at a certain location normalized by that in the pure fuel stream. Figure 3-6 displays the raw mixture fraction images at about 1 cm above the turbulent jet exit at a Reynolds number of ~2000. The peak signal in the images reads ~1.2×10^4 counts. According to the MCP used in this experiment and the specifications of the ICCD used, the count reading corresponds to 600 photon electrons per pixel. At this level of counts, the noise from the CCD chip is dominated by shot noise. Therefore, the SNR can be estimated to be ~25.

With the corrected mixture fraction images, we calculated the scalar dissipation rate (χ), which is defined as:

$$\chi = D\left[\left(\frac{\partial \xi}{\partial x}\right)^2 + \left(\frac{\partial \xi}{\partial r}\right)^2\right] \tag{3.3}$$

where D is the mass diffusivity, $\frac{\partial \xi}{\partial x}$ is the gradient of the mixture fraction in the axial-direction and $\frac{\partial \xi}{\partial r}$ is the gradient of the mixture fraction in the radial direction. For the flame measurements, D will be a function of temperature and local composition. In the air jet results demonstrated here, D will not be varying significantly. For simplicity, we report χ / D in Figure 3-8, calculating only the spatial derivative terms in Eq. (3.3), with a fourth-order central-difference scheme, as follows:

$$\begin{cases} \dfrac{\partial \xi}{\partial x} = \dfrac{-\xi_{i,j+2} + 8\xi_{i,j+1} - 8\xi_{i,j-1} + \xi_{i,j-2}}{12\Delta x} \\ \dfrac{\partial \xi}{\partial r} = \dfrac{-\xi_{i+2,j} + 8\xi_{i+1,j} - 8\xi_{i-1,j} + \xi_{i-2,j}}{12\Delta r} \end{cases} \tag{3.4}$$

Due to the spatial derivative terms, the calculated scalar dissipation rate is very sensitive to measurement noises, and image processing is usually required in order to obtain reasonable results. Figure 3-8 shows the original and the processed mixture fraction images on the left panels, together with corresponding scalar dissipation images calculated on the right panels.

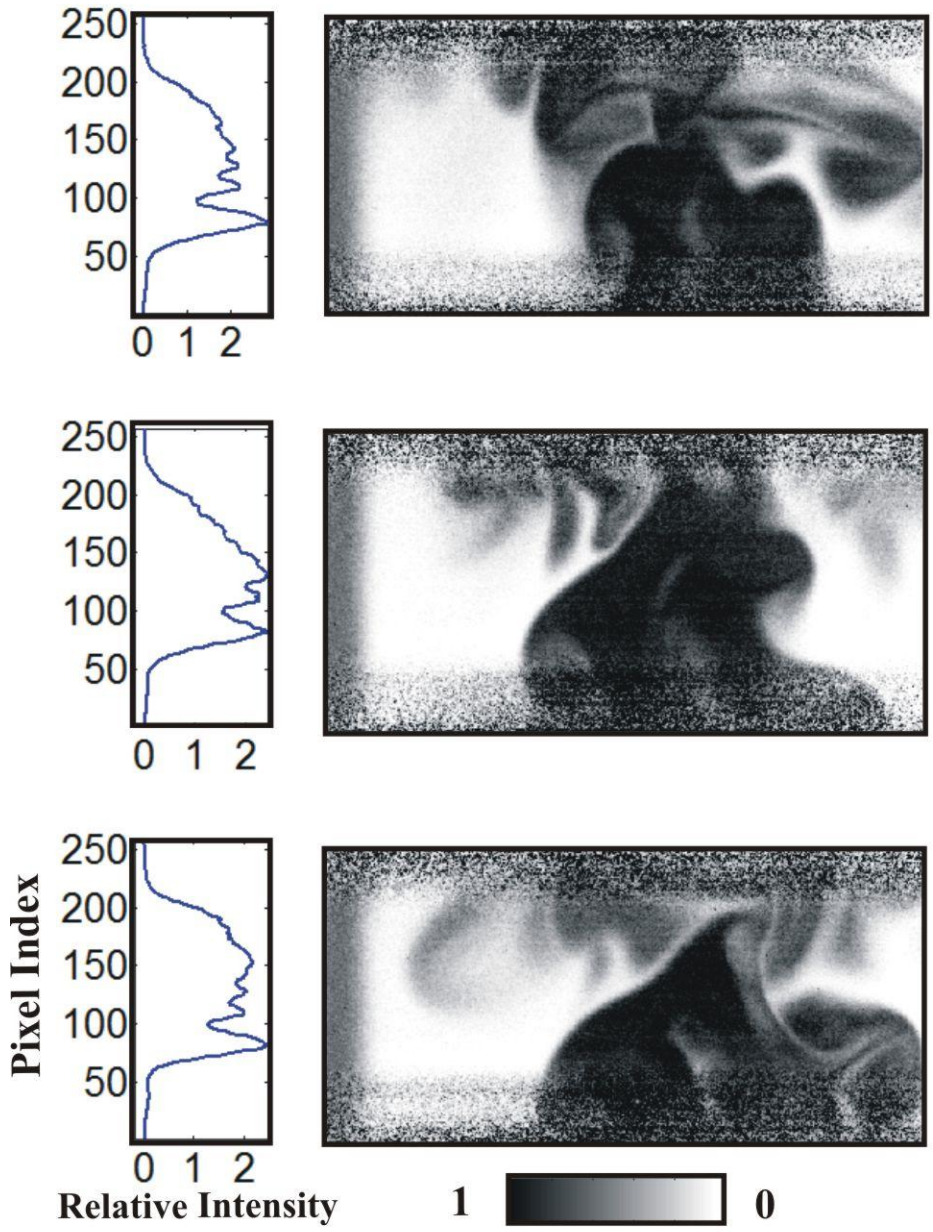

Figure 3-7. Three consecutive mixture fraction images of the turbulent jet with 0.5 second interval at ~1 cm above the twin jet, with laser intensity in the height direction corrected. The center image corresponds to the raw image presented in Figure 3-6.

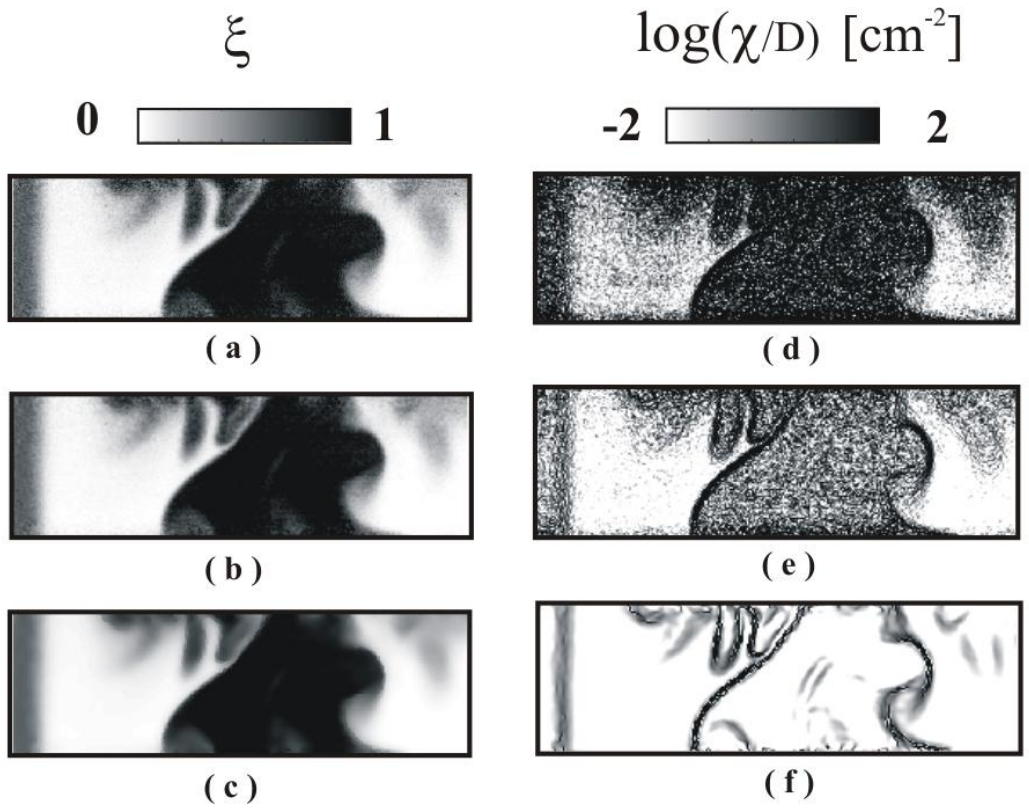

Figure 3-8. The mixture fraction images and diffusivity normalized scalar dissipation rate images. The left three panels show the mixture fraction images, of (a) original, (b) median filtered, and (c) Non-linear anisotropic diffusion filter filtered. Corresponding scalar dissipation images are shown in the right panels (d)–(f).

For the scalar dissipation rate image in panel (d) calculated from the unprocessed images, the inner edge of the scalar dissipation layer is mostly blended with the false results due to noise. The median filtered results in panel (e) shows considerable improvements, where a thin dissipation layer is discernable. Panel (c) shows the mixture fraction images processed with the non-linear anisotropic diffusion filter (NLDF) [79]. This filter is believed to effectively smooth noises while

preserving edges at the same time[17]. By applying this filter, the noise is in scalar dissipation rate images are effectively suppressed, as shown in the panel (f) of Figure 3-8.

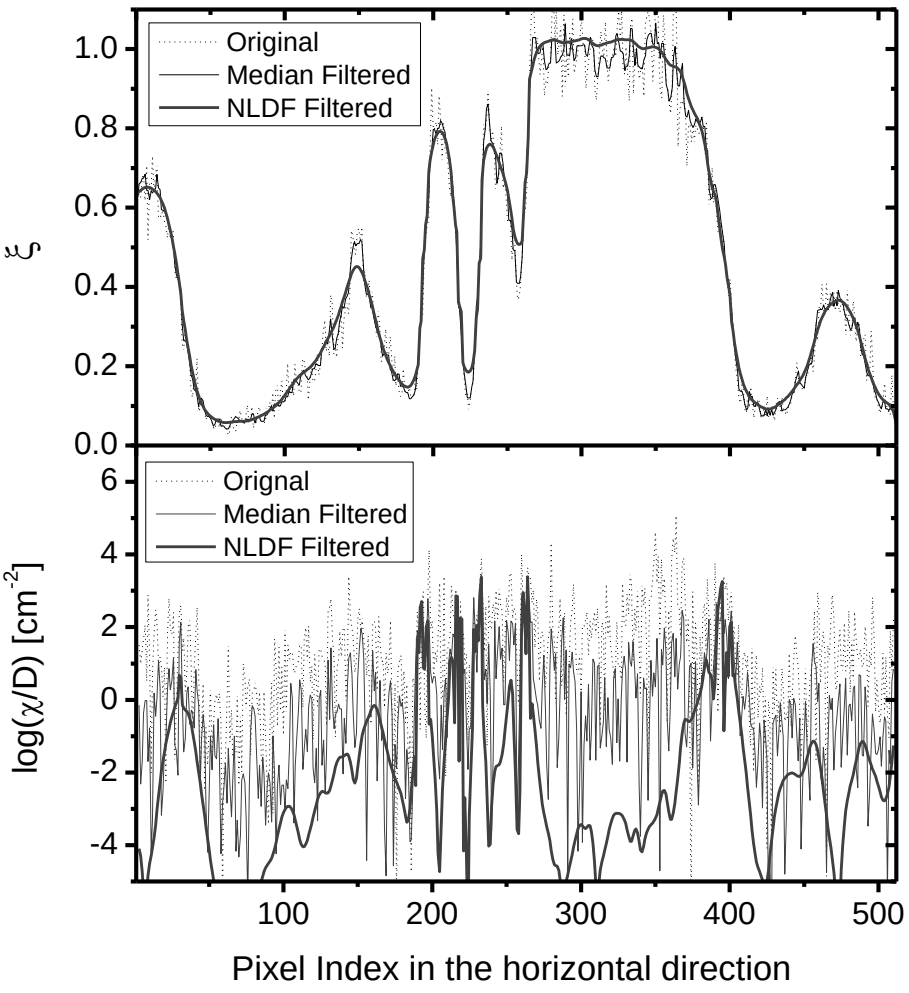

Figure 3-9. Close up view of 40th line of the images in Figure 3-8 to show the effect of image processing in obtaining scalar dissipation rate.

A close-up view of the differences is shown in Figure 3-9. Specifically, the 40^{th} lines of the images shown in Figure 3-8 are plotted. From the upper panel where mixture fraction data is plotted, we can see the NLDF filter preserves the edges quite well, while smoothing the noise at the center of the jet, where mixture fraction is close to 1. In the lower panel which shows the scalar dissipation rate data, the peak scalar dissipation rate is not reduced due to denoising. The peaks in the dissipation rate plot faithfully reflected the cliffs in the mixture fraction image. The false high magnitude of the dissipation rate near pixel index 100 and 300, which corresponds to flat low tracer region and the center of the jet, respectively, are effectively suppressed.

Nevertheless, it should be noted that all image processing selectively abstract and discard information from the image. For quantitative analysis, these processing tools should be tested using statistical theories, and should not be simply judged by the visual aids it offers. Recent researches [80] provided new insights on noise and resolution corrections for the purpose of evaluating scalar dissipation rate.

3.3 Demonstration of mixture fraction imaging in CO flame

3.3.1 Experimental setup

For the experiment in the CO/air flame, both the Rayleigh and TPLIF signal are required for data reduction. Besides the ICCD used for taking TPLIF signal, an interline transfer CCD camera (Apogee KX85) collected the Rayleigh scattering signal from the PD laser pulse at 532 nm. The camera was equipped with a commercial lens (Nikon 85 mm *f*/1.4) fitted onto an extension tube, a close up lens (*f*=1000 mm), and a band pass filter (Thorlabs, FL532-1) to block flame luminosity and the I_2 fluorescence. The flame luminosity was blocked mostly by the electronic shutter of the CCD, while the 1 nm narrow band pass filter blocked the broadband red-shifted I_2 fluorescence.

According to ideal gas law, the local number density of the tracer can be much lower in flame measurement than in air jet under the same seeding level, at locations where temperature is high. To increase signal levels, the lasers were focused more tightly than those in the air jet experiment. The first laser sheet (the PD Laser Pulse) had a thickness of ~0.4 mm and a height of ~4 mm; and the second one (the LIF Laser Pulse) a thickness of ~0.2 mm and a height of ~3 mm. In this case, the height of the second laser sheet is the limit of the size of the field-of-view, which can be enlarged by using a more powerful laser to generate the LIF Laser Pulse. With the collection optics described above, each pixel (with a pixel size of 6.7 μm) on the Rayleigh scattering image corresponded to a probed volume of 22.7 × 22.7 × 400 μm; and each pixel (with a pixel size of 13 μm) on the TPLIF image corresponded to a probed volume of 20.8 × 20.8 × 200 μm. Both of the Rayleigh and the TPLIF images used two-by-two binning. The Rayleigh and TPLIF images were mapped together on a pixel-by-pixel basis in a calibration experiment imaging the same designed target. All results were obtained from single-shot measurements.

I_2 vapor was seeded into the flow using the same device before, but passing CO fuel stream through the vessel. The vessel was kept above room temperature, achieving an I_2 seeding mole fraction of ~0.1% in the fuel stream. A flow meter controls CO flow rate, achieving a Reynolds number of about 500 at the burner exit.

3.3.2 Data reduction and results

For the CO/air flame, the conversion between mass fraction and mole fraction of iodine is more complicated, because the temperature and species composition are not uniform. Mixture fraction is related to the measured signals as follows:

$$\xi(r) = \frac{n_I(r)W_I \Big/ \sum W_i \cdot n_i(r)}{n_{I,f}W_I \Big/ \sum W_{i,f} \cdot n_{i,f}} = \frac{n_I(r)}{n_{I,f}} \cdot \frac{\sum W_{i,f} \cdot n_{i,f}}{\sum W_i \cdot n_i(r)} = S_I^N \cdot \frac{\sum W_{i,f} \cdot n_{i,f}}{\sum W_i \cdot n_i(r)} \tag{3.5}$$

where n is the number density, W is the molecular weight, S_I^N is the iodine TPLIF signal at a specific location (r) normalized by that of the fuel stream, and i is the index of species. In our current laminar flame experiment, the normalized signals are readily available. Because the imaging area spans from the fuel stream center to the pure ambient air region and the signal at the former location offers a normalization reference on a pulse-to-pulse basis. In a turbulent flame, however, a reference cell or jet is required.

As shown in Eq. (3.3), the mixture fraction is related to the local number densities, which is obtained with the help of a Rayleigh scattering signal. Normalizing Rayleigh scattering signal of a specific location relative to fuel stream, we have:

$$S_{Ray}^N = \frac{\sum \delta_i \cdot n_i(r)}{\sum \delta_{i,f} \cdot n_{i,f}} \tag{3.6}$$

where δ_i is the Rayleigh scattering cross section of species i.

Combining the above two equations, mixture fraction can be written as:

$$\xi(r) = \frac{S_I^N}{S_{Ray}^N} \cdot \frac{\sum \delta_i \Big/ \delta_f \cdot X_i(r)}{\sum W_i \Big/ W_f \cdot X_i(r)} \tag{3.7}$$

where $X_i(r)$ is the mole fraction of species i. In Eq.(3.7), ξ is implicitly determined because the local composition $X_i(r)$ is a function of ξ. An iterative scheme [13] is adopted to calculate ξ

based on the Rayleigh scattering image, the iodine TPLIF image, and $X_i(\xi)$ obtained through opposed-flow flame calculation.

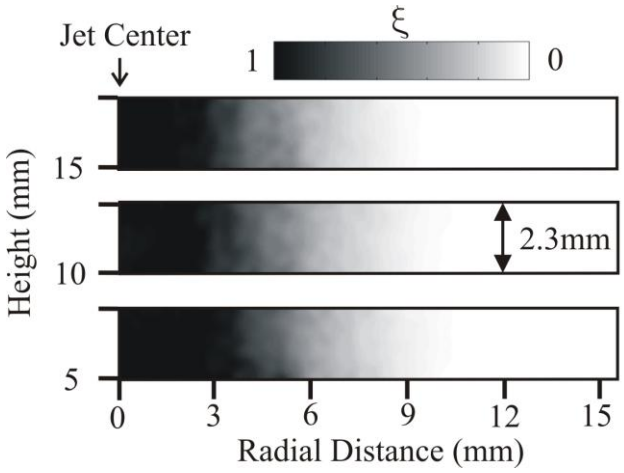

Figure 3-10. A set of sample imaging measurements of the mixture fraction.

A set of sample images for the mixture fraction is shown in Figure 3-10, measured at three different heights above the exit of the non-premixed CO/air jet flame. The height of each image is 2.3 mm, limited by the height of the excitation laser sheet at 298 nm. An image height of 2.3 mm provides a reasonably large field-of-view, and ways to enlarge it are discussed later in this chapter.

In our current experiment, the accuracy of the Rayleigh scattering measurement is restricted by two factors. Firstly, the fluorescence from molecular iodine was suspected for a ~3% interference on the Rayleigh scattering signal. Secondly, the background flame luminosity was not blocked effectively enough, due to the long exposure time of our CCD camera. However, an immediate elimination of above interferences can be achieved using a laser with higher pulse energy and a camera with faster gating. The higher laser power increases the Rayleigh scattering signal linearly but saturates the I_2 fluorescence or even decreases it due to the more effective dissociation of I_2.

The flame luminosity interference can be completely eliminated using the newer models of interline transfer CCD cameras whose gating time is about four orders of magnitude shorter than that of the current one. With such improvements, a SNR of more than 100 for Rayleigh scattering is obtainable under the spatial resolution used here[25]. Because this SNR greatly exceeds that of the TPLIF signal, we neglect the noise from Rayleigh scattering measurement in the following analysis. These updated experiments will be carried out soon.

3.4 Effect of flame chemistry

The above sections essentially assessed the optical (or spectroscopic) performance of the PDS-based technique. Two other aspects of the technique, 1) the influence of the flame chemistry, and 2) the influence of differential diffusion, which are addressed in this and the next section, respectively.

In the present experiment using CO as fuel, only I_2 is considered as the PD target. In a perfectly dry CO/air flame, the seeded I_2 is subject to only one possible chemical reaction, the thermal dissociation reaction, to form I atoms. When moisture (due to either water (H_2O) or hydrogen (H_2) impurities) exists in the fuel and/or air stream, the seeded I_2 becomes subject to other chemical reactions, which lead to another iodine containing species: HI[35-37], which is not photodissociated in the current experimental configuration. Therefore, strictly speaking, the concentration of I atoms does not form a conserved scalar unless HI can also be photodissociated completely. This problem is the first aspect of flame chemistry effect we consider in this section. We numerically evaluate the error caused by incomplete PD of HI, and find negligible errors in the experiments when the amount of moisture is below ~ 1000 ppm.

These numerical studies computed the mole fraction of HI in an opposed-flow flame, with various amount of H_2 in both the fuel (99% CO and 1% I_2 by mole fraction) and the oxidizer (21% oxygen and 79% nitrogen by mole fraction) streams. In these calculations, the reaction mechanism described in [35, 36] was combined with the GRI-MECH 3.0 [34]The results of these calculations are shown in Figure 3-11 and Figure 3-12, all obtained under a pressure of 1 atm. Figure 3-11 shows the fraction of I atoms existing in HI out of all I atoms in the flow as a function of mixture fraction, computed under conditions simulating the current experimental conditions (with 100 ppm H_2 present in both the fuel and oxidizer stream and a temperature of 343 K for both the fuel and the air streams). The computations were performed at three strain rates (10, 20, and 40 s^{-1}) to represent the experiments. The temperature profiles obtained under all strain rates are similar and that from the case with a strain rate of 20 s^{-1} is shown here. Figure 3-11 suggests that the peak HI concentration occurs in regions where $0 < \xi < 0.2$ and $0.6 < \xi < 0.8$; and in these regions, the fraction of I atoms existing in HI does not exceed 4%. Therefore, in the results presented in Figure 3-11, up to 4% of uncertainty need to be considered in addition to the shot-noise considered.

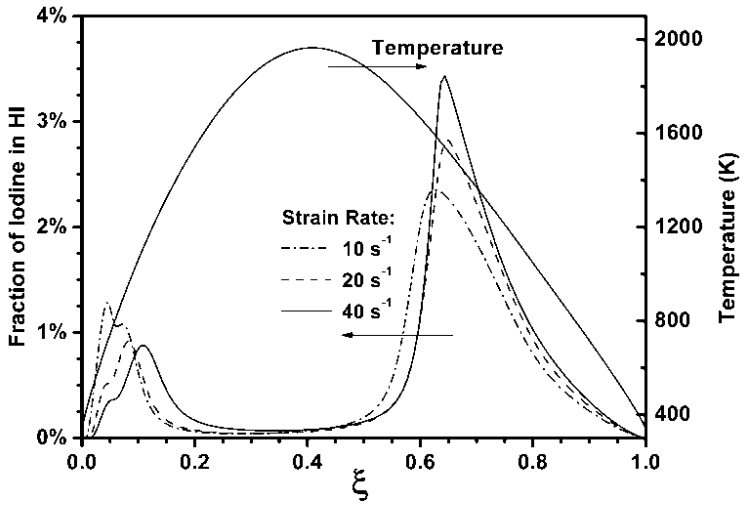

Figure 3-11. Profiles of the fraction of I atoms existing in HI molecules with 100 ppm H_2 in both the fuel and oxidizer streams, suggesting that the maximum error in ξ measurement due to the existence of HI occurs in regions where $0 < \xi < 0.2$ and $0.6 < \xi < 0.8$. The temperature shown corresponds to the case with a strain rate of 20 s^{-1}.

Similar computations as shown in Figure 3-11 were repeated at various levels of H_2 concentration, and the peak fraction of I atoms existing in HI was extracted and plotted in Figure 3-12. As can be seen, the peak fraction remains below ~5% when the H_2 mole fraction is below 1000 ppm. This relative insensitivity to moisture represent a practical advantage compared to the use of NO as a passive seed, which requires the flame to be strictly dry so that NO can indeed remain passive [17]. For application in which the influence of HI is not negligible (e.g., the seeding of I_2 in a moist CO/air flame or a hydrocarbon flame), a second PD Laser Pulse can be employed to photodissociate HI so that the concentration of I atoms still forms a conserved scalar. Both HI and I_2 can be simultaneously and effectively photodissociated with commonly available laser sources, e.g., the fourth harmonic output of Nd:YAG lasers at 266 nm or the output of KrF excimer lasers at 248 nm, as shown in the previous chapter[21]. Therefore, the production of HI does not pose a fundamental restriction for the use of I_2 as a precursor.

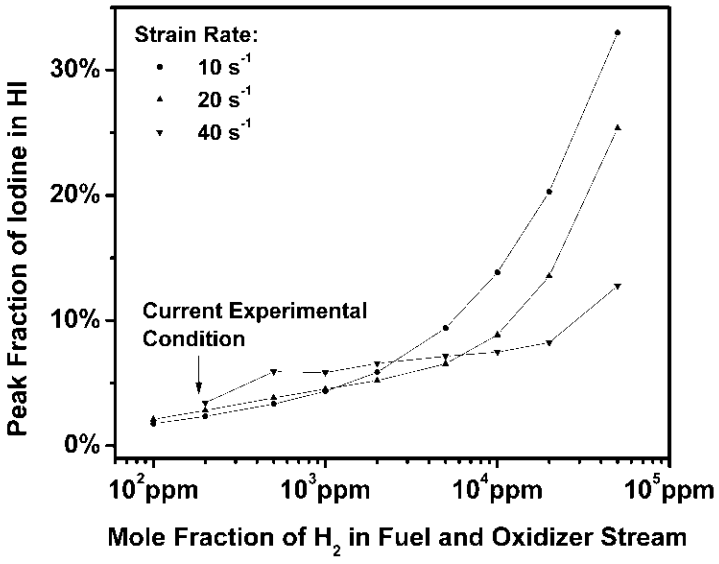

Figure 3-12. The peak fraction of I atoms existing in HI molecules when there are different levels of H_2 in both the fuel and oxidizer streams, illustrating the technique's resistance to impurities.

Alternatively, HI can be used as the precursor. When HI is seeded in typical hydrocarbon flames (e.g., methane (CH_4)-air or ethane (C_2H_6)-air flames), it reacts to form two predominate iodine-containing species: HI and I. Hence, only the PD of HI needs to be considered. The disadvantage of HI seeding, compared to I_2, involves mostly increased practical handling difficulties.

The other flame chemistry related problem to be discussed in this section is the interference of I_2 seeding to the radical pool. As with other seeding methods, the design of an optimal seeding level involves a tradeoff between the signal level and the interference to the flame chemistry, especially the radicals. The seeding of I_2 is expected to influence mainly three radicals: H, OH, and CH_3. Figure 3-13 shows the change of peak [H] and [OH] when I_2 is seeded at three different levels (0.1%, 0.5% and 1%) relative to the case without seeding obtained by OPPDIF calculations. The calculations were performed for strain rates ranging from 40 sec^{-1} to 320 sec^{-1},

representing a wide range of flame conditions from close-to-equilibrium to close-to-extinction. The results for another relative important radical CH_3 are similar and are therefore not shown here. Overall, at a seeding level of 0.1%, the change in radical concentration is minimal. While at a seeding level of 1%, the interference is appreciable with: [OH] changed by 7% to 13%, and [H] changed by 19% to 25%, depending on strain rate. As demonstrated in experiments in previous sections, an I_2 seeding level of 0.1%~0.5% should produce sufficient signal level for single-shot imaging [21, 22]. According to Figure 3-13, the interference is acceptable at this level of seeding.

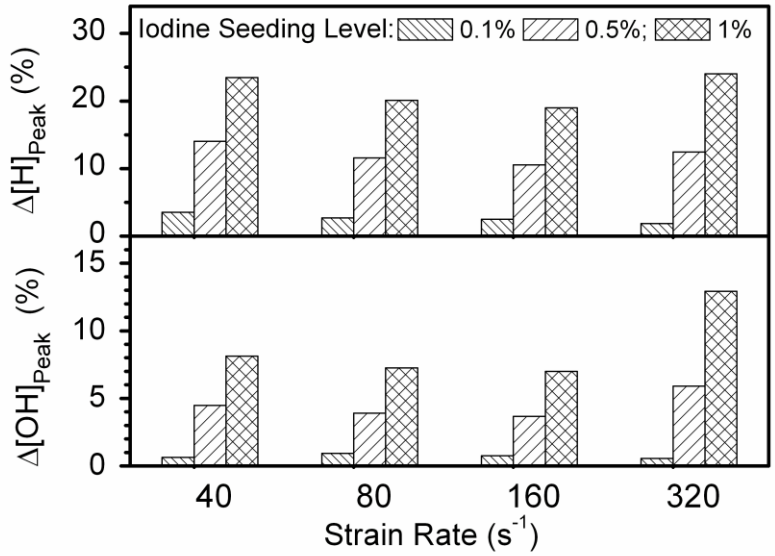

Figure 3-13. Relative change in radical concentrations due to I_2 seeding

3.5 Effect of differential diffusion

The mixture fraction measured by this technique is essentially that defined based on the iodine element, which could be different from mixtures fractions defined otherwise (e.g., based on a different element) due to differential diffusion. In many applications, it is desirable to use the iodine-based mixture fraction to approximate a mixture fraction defined otherwise, or to compare it to one defined otherwise. For example, the Bilger definition [7, 29] is commonly used in the study of combustion. In this case, it is highly desirable that the iodine-based mixture fraction (still denoted by ξ) can approximate that based on the Bilger definition (denoted by ξ_B) accurately. On the other hand, differential diffusion is historically quantified by the difference between two mixtures fractions defined based on different elements [29]. Therefore, it is desirable to maximize such difference for the quantitative study of differential diffusion.

Based on these considerations, the difference between the ξ measured by the PDS method could be either a disadvantage or an advantage, depending on the specific application. The influence of differential diffusion is investigated here to elucidate the applicability of the PDS technique. Computations were again performed using the configuration of an opposed-flow flame, with conditions similar to those used in Figure 3-12 (an inlet temperature of 343 K for both the fuel and oxidizer under atmospheric pressure). The transport properties of I_2 and HI were taken from[36]. The relative difference between the iodine-based ξ and ξ_B is shown in Figure 3-14 for three different flames: a CO flame, a CH_4 flame, and a C_2H_6 flame. The calculation of the CO flame was intended to simulate the experimental condition; therefore, the fuel stream was set to contain 100 ppm of H_2 and 0.1% of I_2. Figure 3-14 shows that the iodine-based ξ is different from ξ_B by more than ±15% across most of the regions in the flame. This distinct difference was

caused by the relatively slow diffusion of I_2 (because it is substantially heavier than other species) in the flame.

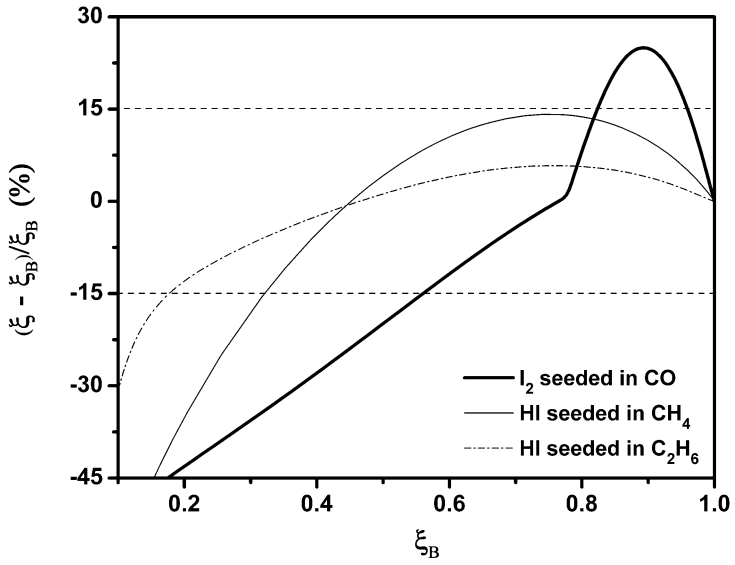

Figure 3-14. Analysis of the error in ξ measurement caused by differential diffusion when different precursors are used in different flames. The strain rate used was 40 s^{-1} for the CO flame, and 100 s^{-1} for both of the hydrocarbon flames.

Accordingly, this difference can be reduced by using a lighter precursor, e.g., HI; on the other hand, such pronounced difference can be exploited to study differential diffusion qualitatively.As shown with the calculations performed for the CH_4 and C_2H_6 flames, the seeding of HI results in smaller differential diffusion, because HI matches the diffusion properties of the species in the flame better than I_2. In both of the hydrocarbon flames, the use of HI results in a difference within ±15% for most of the regions in the flame, from the fuel-rich to fuel-lean regions (with ξ around 0.2 ~ 0.3). Note that the seeding of HI in the C_2H_6 flame results in less difference than in the CH_4 flame, because C_2H_6 is heavier than CH_4 and matches HI's diffusion properties better than CH_4.

Therefore, when the iodine-based ξ is intended to represent/approximate ξ_B, the use of HI as the precursor can provide reasonable accuracy across most regions in the flame, and the accuracy improves when larger hydrocarbons are used as the fuel.

Chapter 4

Study on ASE distortion in TPLIF measurement

In Chapter 2, TPLIF is analyzed at a spatial point, i.e., with 0D modeling. Such analysis is accurate when the fluorescence emission exits the probe volume without amplification. However, in some TPLIF experiments, such amplification may be significant and strong amplified spontaneous emission (ASE) field may be generated. The ASE field invalidates the 0D modeling approach, by coupling the florescence at different spatial locations in the entire probe volume. More elaborate models that consider 1D and 2D effects due to ASE become necessary in line and planar imaging. The objective of this chapter is to analyze the ASE distortion of the TPLIF signal, first using hyperbolic differential equation in line imaging, then using Monte Carlo simulation, which provides the first 2D analysis of this problem to the author's knowledge. The understanding gained on ASE distortion and the possible correction scheme proposed in this chapter is expected to enhance the applicability and accuracy of TPLIF technique in flow imaging.

4.1 ASE physics in TPLIF

ASE is widely observed in flame and plasma diagnostics using TPLIF [18, 32, 81-90]. It was often regarded as a complication to the LIF signal interpretation, but was also proposed as a diagnostic tool [82, 86-88]. The distortion of line imaging profile due to ASE was reported for O atom [84] and H atom [90]. Directly relevant to the focus of this research is the ASE effect in TPLIF imaging of krypton atom, for the purpose of 2D mixture fraction imaging. Specifically, under their seeding level of 1%, ASE is detectable but results in negligible distortion of the LIF profile over a length of 8 mm. With gradually increased krypton mole fraction, significant distortion in LIF signal was reported at a seeding level of 4%.

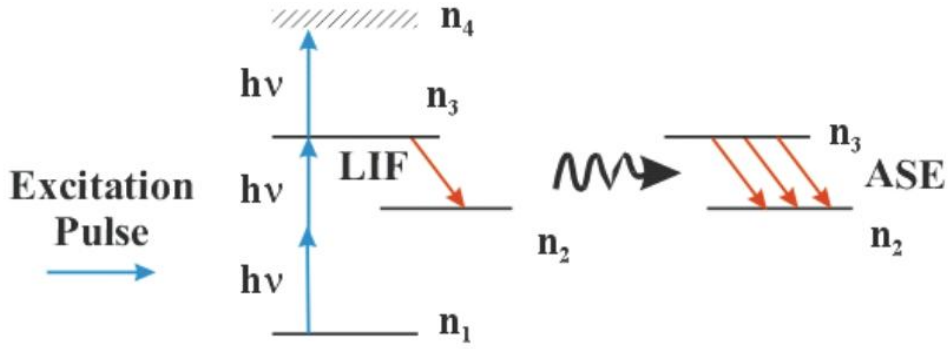

Figure 4-1. Concept of ASE in a TPLIF experiment

Compared to single-photon LIF, TPLIF is inherently prone to ASE interference. A conceptual energy diagram for a typical TPLIF measurement for atomic species is shown in Figure 4-1. The ground state *1* simultaneously absorbs two photons to reach the excited state *3*. And *3* state atoms may absorb an additional photon to be ionized into state *4*. Meanwhile, states *1* to *3* are coupled through collisional quenching. The LIF photons from the *3* state to *2* are collected to infer the number density of the species. Different from the single-photon LIF measurement, the excited

state *3* is optically coupled not to the ground state *1* due to selection rules, but to the initially unpopulated fluorescence destination state *2*. Therefore, population inversion is usually formed between *3* and *2*. From the perspective of photons, the spontaneous emission (fluorescence) will be amplified while traveling in such population inverted medium, due to the stimulated emission from state *3* to *2*, as shown in the right portion of Figure 4-1. From the perspective of atoms, the incoming ASE radiation de-excites atoms at state *3* to *2*, competing with other depopulation mechanisms including quenching and ionization, which have been discussed in Chapter 2. Such competition complicates the interpretation of the TPLIF signal.

The ASE interference to TPLIF signal is complicated for the following reasons. First, the interference is non-linear. Before saturation happens, ASE intensity (I_{ASE}) in a certain direction grows within the probe volume approximately following $\exp(C\int_0^X n_3(x) - n_2(x)\ dx)$, where the population n_3 and n_2 are functions of the distance *x*, and *C* is a factor related to the absorption cross section of the transition between n_3 and n_2. For this reason, I_{ASE} is a no-linear function to the excitation laser energy, and to the ground state atom number density which we usually seek to measure. Second, the interference is non-local. The LIF signal at a certain location relies on events at surrounding sites. For example, the LIF signal at the two ends in the line imaging volume would experience stronger ASE interference, because the ASE radiation has a longer path length to grow. In the following sections, models are developed to study such complex phenomenon quantitatively.

Another important observation is that the ASE interference sets an upper limit on the SNR of TPLIF signal for interference-free measurement under a specific experimental setup. The TPLIF signal level is determined by the number density of two-photon excited state n_3. When the setup is fixed, the path length and the laser duration are fixed. A high SNR necessarily means higher n_3,

for which a threshold exists for the onset of ASE considering its exponential growth over n_3. Suggestions to overcome this limitation are given in later sections.

4.2 1D modeling of ASE interference

The goal of model development is to incorporate all the physical processes described in the above section and to predict the temporal and spatial profiles of all the relevant physical properties, including the population at each level, the LIF photon flux, and the ASE radiation field.

Models based on the rate equation (RE) approximation represented a significant portion of past modeling work, due to their simplicity [21, 22, 88, 89, 91-94]. Although rigorous treatment should base on the density matrix formulation [95, 96] and the Maxwell-Bloch equations [97], the rate equation approach is sufficiently accurate if the rise time of the excitation pulse is sufficiently longer than the dephasing time and/or the excitation laser is multimodal [92, 95]. For the applications we are interested in this research, these conditions are satisfied. Under the RE approximation, we improve the previous 1D model in [89, 93] by: 1) simultaneously tracking the incident radiation field and the ASE radiation field, and 2) treating these fields as traveling waves. Now the equations yield the following form:

$$\frac{\partial}{\partial t}\begin{bmatrix} n_1 \\ n_2 \\ n_3 \\ I_L \\ I_{ASE,f} \\ I_{ASE,b} \end{bmatrix} = \frac{\partial}{\partial x}\begin{bmatrix} 0\cdot n_1 \\ 0\cdot n_2 \\ 0\cdot n_3 \\ -c\cdot I_L \\ -c\cdot I_{ASE,f} \\ c\cdot I_{ASE,b} \end{bmatrix} + \begin{bmatrix} -W_{13}\left(n_1 - \frac{g_1}{g_3}n_3\right) + \left(A_{21}+Q_{21}\right)n_2 + Q_{31}n_3 \\ \left(W_{32}^f + W_{32}^b\right)\left(n_3 - \frac{g_3}{g_2}n_2\right) - \left(A_{21}+Q_{2a}\right)n_2 + \left(A_{32}+Q_{32}\right)n_3 \\ W_{13}\left(n_1 - \frac{g_1}{g_3}n_3\right) - \left(W_{32}^f + W_{32}^b\right)\left(n_3 - \frac{g_3}{g_2}n_2\right) - \left(W_{34}+A_{32}+Q_{3a}\right)n_3 \\ c\left(-2W_{13}\left(n_1 - \frac{g_1}{g_3}n_3\right) - W_{34}n_3\right)\cdot h\nu_L \\ c\left(W_{32}^f\left(n_3 - \frac{g_3}{g_2}n_2\right) + A_{32}n_3\frac{\Delta\Omega_f}{4\pi}\right)\cdot h\nu_{ASE} \\ c\left(W_{32}^b\left(n_3 - \frac{g_3}{g_2}n_2\right) + A_{32}n_3\frac{\Delta\Omega_b}{4\pi}\right)\cdot h\nu_{ASE} \end{bmatrix} \quad (4.1)$$

The notations in these equations are defined as follows:

x and *t*: the space in the *x*-direction and time, respectively.

I_L: the radiance of the excitation laser pulse.

$I_{ASE,f}$ and $I_{ASE,b}$: the irradiance of the ASE photons in the forward (i.e., positive *x*) and backward (i.e., negative *x*) directions, respectively.

ν_L and ν_{ASE}: the frequency of the excitation photons and ASE photons, respectively.

Qs: the collisional quenching rates (with subscripts denoting the levels involved). Q_{2a} and Q_{3a} denote the collisional quenching rates from state 2 and 3 to all other states, respectively.

g_i (*i*=1, 2, 3, 4): the degeneracy of each level.

As: the Einstein A coefficients (with subscripts denoting the levels involved).

W_{13} *and* W_{34}: the transition rate coefficients (with subscripts denoting the levels involved). $W_{13} = \frac{\alpha_{TP} I_L^{\,2}}{h\nu_L} = \sigma_{TP}\left(\frac{I_L}{h\nu_L}\right)^2$ and $W_{34} = \frac{\sigma_{ion} I_L}{h\nu_L}$ where α_{TP} is the two-photon absorption

coefficient and σ_{TP} and σ_{ion} are the two-photon absorption and ionization cross sections, respectively.

W_{32}^{f} and W_{32}^{b}: the transition rate coefficients between levels 2 and 3 in the forward and backward direction, respectively. $W_{32}^{f} = \frac{B_{32} I_{ASE,f}}{c\Delta\nu_{ASE}}\Gamma$ and $W_{32}^{b} = \frac{B_{32} I_{ASE,b}}{c\Delta\nu_{ASE}}\Gamma$, where B_{32} is the Einstein B coefficient for stimulated emission from state 3 to state 2, $\Delta\nu_{ASE}$ is the linewidth of the ASE radiation, Γ the overlap integral defined as $\int_{-\infty}^{+\infty} g(\nu) f(\nu) d\nu$ with $g(\nu)$ and ($f(\nu)$ representing the line shape function of the absorption transition and the ASE radiation, respectively. In this work , B_{32} is calculated through $A_{32}c^3 / 8\pi h\nu_{ASE}{}^3$ [98]; and *f(ν)* and *g(ν)* were assumed to be Gaussian profile with the same linewidth, resulting in a Γ of 0.5. More details of the overlap integral, line shape functions, and their effects on LIF measurements, can be found in[99]. In this work, $\Delta\nu_{ASE}$ was taken to be 1 cm^{-1} [89]. The narrowing and rebroadening of ASE radiation linewidth was neglected in our temporally resolved analysis. More details in modeling these effects can be found in [100, 101].

$\Delta\Omega_f$ and $\Delta\Omega_b$: the solid angle formed by the incident and exit surface of the domain of interests (i.e., the measurement volume) relative to the point at which ASE photons are emitted. In this work, the measurement volume was modeled as a rectangular cuboid. In this case, $\Delta\Omega_f = 4\tan^{-1}\left(\frac{T}{2(L-x)}\right)\sin(\tan^{-1}\left(\frac{H}{2(L-x)}\right))$ and $\Delta\Omega_b = 4\tan^{-1}\left(\frac{T}{2x}\right)\sin(\tan^{-1}\left(\frac{H}{2x}\right))$, where *H*, *T* and *L* are the height, thickness, and length of the simulation domain.

Eq. (4.1) is a system of hyperbolic partial differential equations which is solved using the Lax-Wendroff scheme [102]. The first three equations in Eq. (4.1) describe the transitions among

levels 1-3 due to absorption, quenching, spontaneous and stimulated emission, and ionization. The fourth one describes the attenuation of the excitation laser pulse due to two-photon absorption and ionization as it propagates through the target atoms. The fifth and sixth equations describe the amplification of the ASE photons in the forward and backward directions, respectively. These equations are developed based on the assumption that the ASE photons only propagate along the *x*-axis, and therefore are only strictly applicable to 1D problem. Therefore, Eq. (4.1) approximates the scenario where ASE in one direction (e.g., in the *x*-direction) is sufficiently stronger than in all other directions. One practical situation for this scenario to occur is when the excitation laser pulse is focused into a long and thin beam. In this case, there is not sufficient gain length to amplify the ASE photons except in one direction (the *x*-direction).

Most previous TPLIF measurements were performed with a laser beam, therefore satisfied the condition of 1D problem. Here we compare the experimental data on the scaling relationships between the LIF signal, the ASE signal and the excitation laser pulse energy with our model predictions, as shown in Figure 4-2. This calculation simulated the two-photon LIF measurements of H atoms in a H_2/O_2/Ar flame[81]. Ground state H atoms are excited at 205 nm via two-photon absorption to emit LIF and ASE photons at 656 nm. The following parameters were assumed to match the experimental conditions in [81]. The number density of H atoms in the ground state (n_1) was assumed to be 8.5×10^{14} cm^{-3} from an equilibrium calculation, and was assumed to be uniform along the excitation laser path. The measurement volume was taken to be a rectangular cuboid with a length of 3 cm, and a width and height of 120 μm. The excitation laser pulse was assumed to have a Gaussian temporal profile with a FWHM of 3.5 ns and a total simulation duration of 10 ns. The quenching cross sections from level 2 and 3 were determined to be 8.1×108 s^{-1} according to [83], under the temperature and pressure used in the experiments. Other spectroscopic parameters are summarized in Table 4-1.

As can be seen in Figure 4-2, the scaling relationships between LIF/ASE signals with the excitation laser pulse energy are well predicted. For the LIF signal, it scales with E^2 below ~300 μJ, with E denotes the pulse energy; and scales with E at higher pulse energies, due to the onset of ionization and ASE depopulation. For the ASE signal, there exists a sharp onset near 150 μJ, after which saturation of ASE happens with a scaling of close to E^2 above ~400 μJ. The good agreement shown here validates our modeling using the system of hyperbolic PDEs in 1D cases.

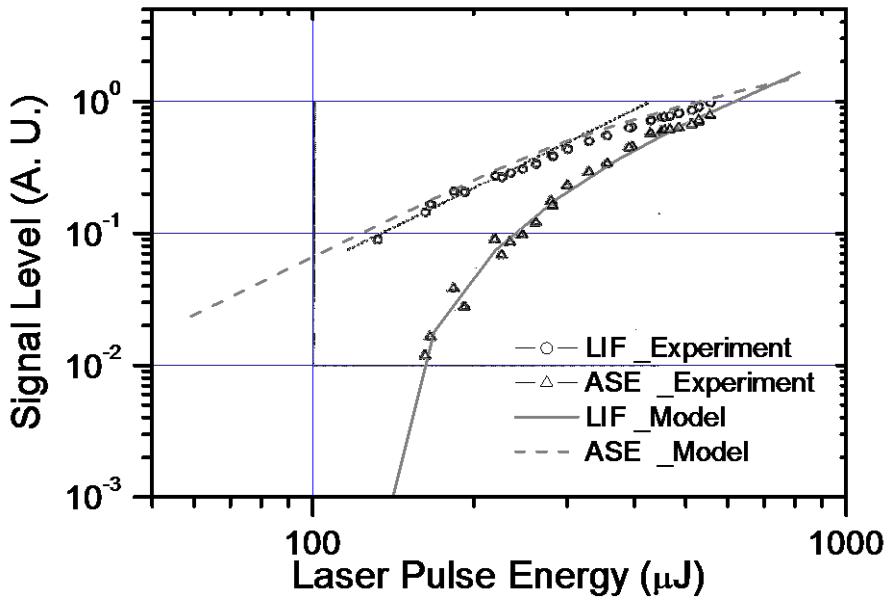

Figure 4-2. Comparison of experimental data and model predictions on TPLIF and ASE signals of H atom over a flat flame burner. Data points adapted from [81]

Parameters	Values	Units
Atomic H		
α_{TP}	1.17×10^{-28}	cm^4/W
σ_{ion}	7	cm^2
A_{32}	5.68×10^{7}	s^{-1}
A_{21}	4.7×10^{8}	s^{-1}
Atomic O		
σ_{TP}	4.85×10^{-46}	cm^4s
σ_{ion}	5.3×10^{-19}	cm^2
A_{32}	2.89×10^{7}	s^{-1}
A_{21}	5.4×10^{8}	s^{-1}

Table 4-1. Spectroscopic properties used during the calculation of TPLIF and ASE.

4.3 Evaluation of ASE distortion in 1D experiments

Although in our demonstration experiments the ASE distortion was not appreciable due to the small seeding level used, distortion was observed at higher seeding levels (4%) in the Kr based TPLIF planar imaging of mixture fraction [18]. Distortion was also analyzed in the line imaging of O and H atoms in laminar premixed flames using both nano- and pico-second excitation lasers. Specifically, for the O atom imaging [84], stronger distortion was observed under pico-second laser excitation, weak distortion was observed under nano-second excitation. The phenomenon of pico-second excitation does not fall into the applicable range of the rate equation approximation adopt in the model developed here. We attempt to explain the experimental observation under nano-second excitation. Calculation assumes an initial O atom concentration with a flame front like profile, which consists of two triangle shaped peaks. The peak oxygen concentration is 0.052 for this atmosphere pressure flame with a peak temperature of 2450K, as estimated in [84]. Excitation laser has a Gaussian temporal profile with a 3.5ns FWHM, and a top-hat spatial profile with a cross section of 0.01 mm^2.

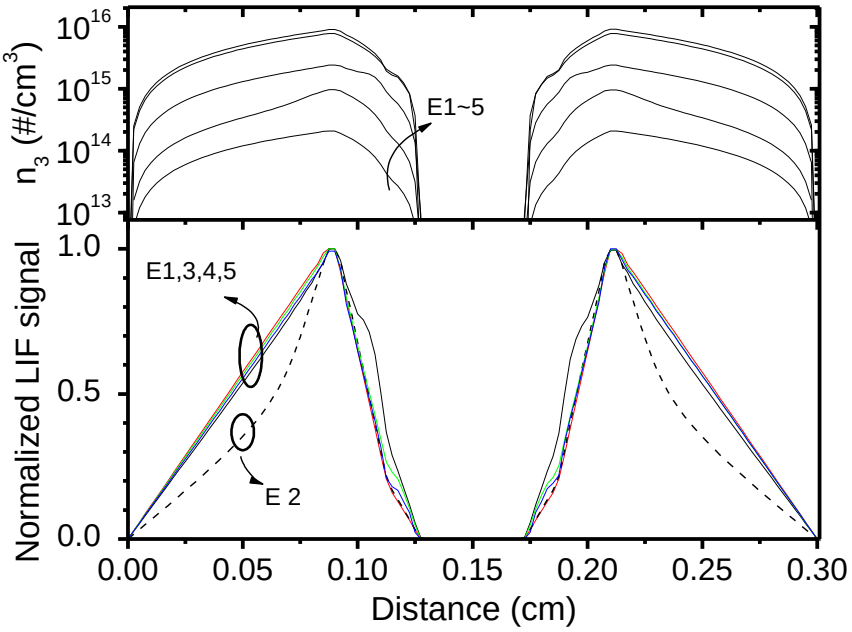

Figure 4-3. Calculation of ASE distortion in TPLIF imaging of O atom in a laminar jet flame, at different excitation energies.

The calculated LIF imaging results are shown in Figure 4-3 at different excitation laser energies, 0.02, 0.044, 0.1, 0.26 and 0.5 mJ, noted as E1~5 in the figure. E1 represent an excitation energy right before the onset of ASE, while E3 represents an excitation energy close to the saturation of ASE. At E1, the LIF profile accurately reflects the true O atom concentration profile. It turned out that the distortion is only significant during the fast increase of the ASE signal. The measurement results seem accurate again after the saturation of the ASE. A closer look, however, shows that the distortion exists all the time after the onset of ASE. However, the region of distortion shifts from the outer region of the line imaging volume, toward the inner region. For this specific initial profile, the distortion seems weaker when it happens primarily at the center of the profile (e.g.,

near location 0.12 cm and location 0.18 cm), where the O concentration is low. Significant distortion was not observed in the line imaging of O atom, probably mainly because the laser energies used are relatively high, i.e., close or above the saturation of ASE.

The result presented in Figure 4-3 also motivates a so called double pulse experimental scheme to monitor, or even correct, the effect of ASE distortion in the TPLIF line imaging. In practice, the probing laser may be split into two beams with a higher and lower pulse energy, and delayed for about 20 ns. Two TPLIF images can be taken and compared, as they were proving the same target, because the flow is essentially frozen in an interval of 20 ns. The ratio of the two profiles yields information on the distortion and the regime of the excitation energies. If ratio profile has a single peak and is lower at the outer edges, then the TPLIF image with the lower laser is taken at a pulse energy before the onset of ASE and yields the undistorted profile though with lower SNR. If the ratio has more than one peaks, then none of the two probe energies lies in the no-distortion regime.

4.4 2D modeling of ASE interference using Monte Carlo simulation

The inherent limitation of the above model is treating the ASE field as two counter propagating beams. This limits the analysis to one-dimensional (1D). With the continuing advancement in high power lasers, it has now become feasible to perform multi-photon LIF experiments in 2D[16, 18, 22]. These considerations motivate a multidimensional model to 1) quantify the applicable range and accuracy of previous 1D models, and 2) facilitate the development and application of 2D imaging diagnostics based on multi-photon LIF techniques. In this section, we develop a Monte Carlo (MC) based method, which enables several key virtues, including the simplicity in

implementation and the flexibility for application in complicated geometry. The MC method has been demonstrated as a powerful and flexible tool to solve radiative transfer problems in various disciplines, ranging from the dust emission from interstellar clouds [103] to the light scattering by biological tissues [104].

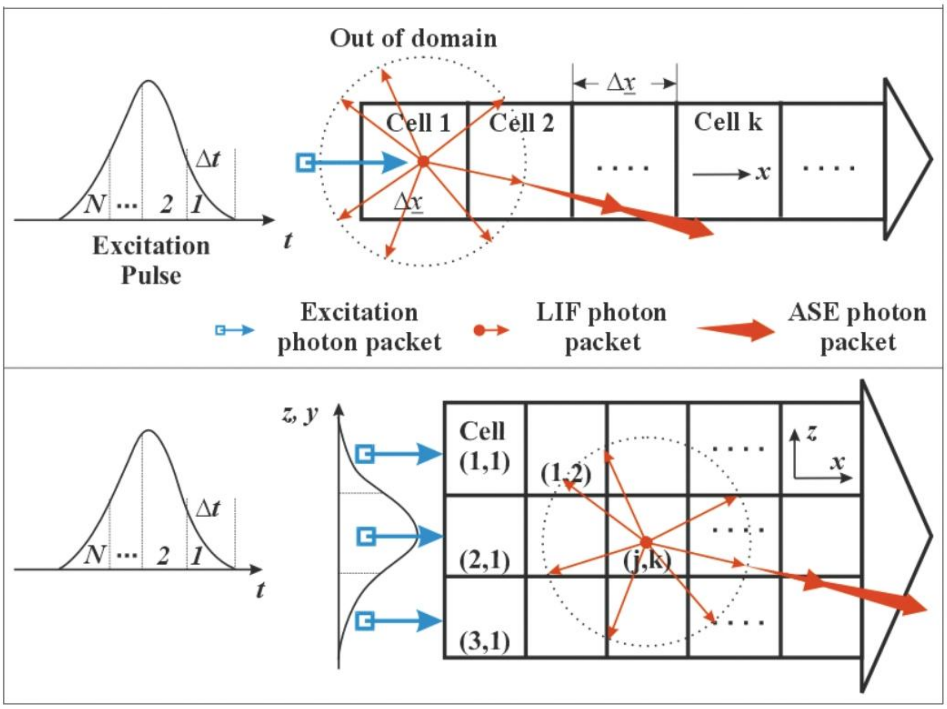

Figure 4-4. Upper panel: schematic of the MC model in 1D; Lower panel: schematic of the MC model in multi-dimensional.

The problem of concern is still illustrated as Figure 4-1, which involves a four-level system interacting with a laser pulse. We first explain the model in 1D with the aid of the upper panel in Figure 4-4., and it is straightforward to explain the model in multidimensional based on the 1D explanation. First, the duration of the excitation pulse (denoted as T) is discretized with a step size of Δt, and the pulse is modeled as N photon packets where $N=T/\Delta t$. The number of photons in the

j^{th} ($i=1, 2, 3, \ldots, N$) packet is then given by $I_L(j\cdot\Delta t)\cdot\Delta t$, where $I_L(t)$represents the temporal profile of the excitation pulse. The 1D computational domain is discretized in the x-direction into grids with width $\Delta x = c\cdot\Delta t$. The model starts by sending the 1st excitation photon packet into the 1st grid, and the absorption of this packet in the first grid is calculated by solving the following equation:

$$\frac{dn_{1,1}}{dt} = W_{13}\left(n_{1,1} - \frac{g_1}{g_3}n_{3,1}\right) \tag{4.2}$$

where $n_{i,k}$ represents the population of atoms on level i in cell k. The initial conditions are $n_{1,k}\,|_{t=0} = n_{1,k}^0$, and $n_{i,k}\,|_{t=0} = 0$ for $i = 2, 3, 4$.

The time step considered here is on the order of sub-picosecond, hence the transition rate coefficients for the two photon absorption W_{13} and ionization W_{34} are so small that linear discretization of these process is sufficiently accurate. Hence, Eq. (4.2) is solved by the following discretization at a step size of Δt:

$$n_{1,1}\Big|_{t=\Delta t} = n_{1,1}\Big|_{t=0} - W_{13}\left(n_{1,1} - \frac{g_1}{g_3}n_{3,1}\right)\Bigg|_{t=0}\Delta t \tag{4.3}$$

And the number density change in state 3 and the excitation laser packets are updated correspondingly, as follows:

$$n_{3,1}\Big|_{t=\Delta t} = n_{3,1}\Big|_{t=0} + \left[W_{13}\left(n_{1,1} - \frac{g_1}{g_3}n_{3,1}\right) - W_{34}n_{3,1}\right]\Bigg|_{t=\Delta t}\Delta t \tag{4.4}$$

and,

$$n_{L,1}\Big|_{t=\Delta t} = n_{L,1}\Big|_{t=0} - 2W_{13}\left(n_{1,1} - \frac{g_1}{g_3}n_{3,1}\right)\Big|_{t=0}\Delta t - W_{34}n_{3,1}\Big|_{t=0}\Delta t \tag{4.5}$$

Then the quenching and spontaneous emission processes are considered, and the populations of atoms are updated as follows:

$$n_{3,1}\Big|_{t=\Delta t} = n_{3,1}\Big|_{t=\Delta t} + \left(Q_{3a} + A_{32}\right)n_{3,1}\Big|_{t=\Delta t}\Delta t \tag{4.6}$$

$$n_{2,1}\Big|_{t=\Delta t} = \left[n_{2,1}\cdot\left(1 - Q_{2a}\cdot\Delta t - A_{21}\cdot\Delta t\right) + n_{3,1}\cdot Q_{32}\cdot\Delta t\right]\Big|_{t=\Delta t} \tag{4.7}$$

After the population of atoms on level 2 is calculated using Eq.(4.7), the number of LIF photons emitted (N^{LIF}) is calculated by:

$$N^{LIF} = n_{2,1}\Big|_{t=\Delta t}\cdot A_{21}\cdot\Delta t \tag{4.8}$$

These LIF photons are emitted randomly in all directions. Our MC model tracks these photons by 1) randomly generating *M* directions, and 2) dividing these LIF photons into *M* packets with each packet propagating in a direction generated in step 1 (with the number of LIF photons in each the m^{th} packet denoted as N_m^{LIF}). Note that in step 2, the LIF photons could simply be divided into packets with equal number of photons (i.e., equal N_m^{LIF} for all *m*). However, this work we adapted the algorithm described in [105] to determine N_m^{LIF} depending on its propagation angle to reduce variation. At this point, the MC model updates the population in all cells, and the number and direction of each LIF photon packet.

Then the 2nd packet of excitation photons is sent into the 1st cell, the calculations described in Eqs. (4.2) to (4.8) are performed to determine the absorption, population change, and LIF photons caused by the 2nd excitation photon packet in cell 1. All these calculations are performed for the

2nd time step (i.e., for time $t=2\Delta t$). For the remaining photons in the 1st excitation packet (i.e., those transmitted through cell 1), the MC model advances their position into the cell 2 and performs the calculations described in Eqs. (4.2) to (4.8) on these photons in cell 2. For the LIF photon packets generated by the 1st excitation packet, the MC model advances their position by Δx in the directions generated above and determines whether if they exit the computation domain (as shown in the upper panel of Figure 4-4). If a packet exits the computational domain, the MC model stops tracking it, and delete the photon to save computer memory. If not, the new location of the LIF packet is determined. In this 1D case, for the LIF packets generated by the 1st excitation packet, the new location can only be in cell 2. But in a multidimensional case (e.g., lower panel), the new location could also be in a neighboring cell. Here, the ASE photons (N^{ASE}) generated by the m^{th} LIF packet in cell 2 over a gain length of Δx is calculated by solving the following equations:

$$\begin{cases} \dfrac{dn^{ASE}}{dt} = \dfrac{B_{32} I_{effective}}{c\Delta\nu_{ASE}} \left(n_{3,1} - \dfrac{g_3}{g_2} n_{2,1} \right) \text{ and } I_{effective} = \dfrac{N_m^{LIF} \cdot \Delta x \cdot h\nu}{\Delta t} \\ \dfrac{dn^{ASE}}{dt} = \dfrac{dn_{2,1}}{dt} = -\dfrac{dn_{3,1}}{dt} \end{cases} \tag{4.9}$$

where $I_{effective}$ is the effective radiance generated by a number of N_m^{LIF} LIF photons.

The Δt used in this work (sub-picosecond) is not sufficiently-small to allow a linear discretization of the above equations; therefore the MC model uses the analytical solution of Eq. (4.9)

$$n^{ASE}\Big|_{t=2\Delta t} = \frac{[2n^{ASE} - (n_{3,2} - n_{2,2}\, g_3/g_2)]\cdot n^{ASE}}{2n^{ASE} - (n_{3,2} - g_3/g_2\, n_{2,2})\cdot \exp[-\Delta x\cdot\sigma_{23}\cdot(n_{3,2} - g_3/g_2\, n_{2,2} - 2n^{ASE})]}\Bigg|_{t=\Delta t} \quad (4.10)$$

Note that in Eq.(4.10), $n^{ASE}\big|_{t=\Delta t}$ equals N_m^{LIF} numerically, but we use n^{ASE} in Eq. (4.10) because the LIF photons are conventionally no longer called LIF photons once ASE occurs. Define the 2nd term on the right hand of Eq. (4.10) as Δn^{ASE}. The population changed on level 2 and 3 in cell 2 caused by this ASE effect are:

$$n_{3,2}\Big|_{t=2\Delta t} = n_{3,2}\Big|_{t=\Delta t} + \Delta n^{ASE} \quad (4.11)$$

$$n_{2,2}\Big|_{t=2\Delta t} = n_{2,2}\Big|_{t=\Delta t} + \Delta n^{ASE} \quad (4.12)$$

At this point, the MC model updates the population on each level and each cell ($n_{i,k}$), the LIF photon packets (N_m^{LIF}) and their directions, and the ASE photon packets (N^{ASE}) and their directions. Temporally, such updates register the cumulative effects due to the 1st and 2nd packets of excitation photons; and spatially, such effects are limited within the first two cells (in a multidimensional case, within a sphere of radius $2\Delta x$).

Then the 3rd packet of excitation photons is sent into the 1st cell, and the calculations described in Eqs. (4.2) to (4.8) are performed for time $t=2\Delta t$ for it in the 1st cell. For the remaining photons in the 1st and 2nd packets of excitation photons, the MC model advances their location by one cell, and performs the calculations described in Eqs. (4.2) to (4.8) for them in the new cells (i.e., cell 3 and 2, respectively). For the LIF/ASE photons generated by the 1st and 2nd packets of excitation photons, the MC model advances their locations by Δx in their corresponding direction, and then determines whether they exit the computation domain. If not, the calculations described in Eqs. (4.10) to (4.12) are performed at the new location.

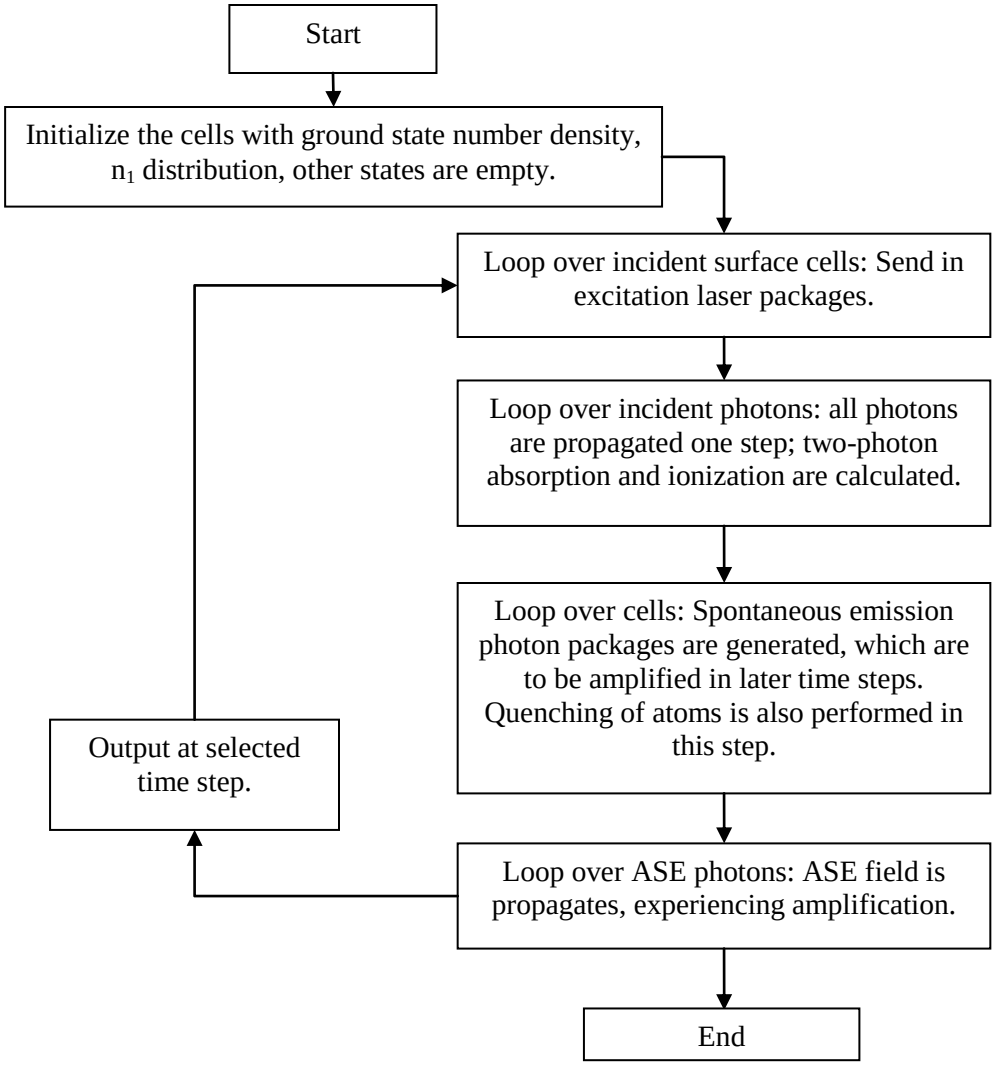

Figure 4-5. Flow chart of the MC code

In this manner, subsequent packets of excitation photons are sent in one packet at a time. With the incident of each new excitation packet, the MC model 1) advances the spatial positions of the remaining photons of and the LIF/ASE packets caused by previous excitation packets by Δx, 2) determines whether a packet exits the computation domain, and 3) if not, performs the calculations in Eqs. (4.10) to (4.12). The MC model terminates when all packets of excitation, LIF, and ASE photons have exited the computation domain. For implementation, as shown in

Figure 4-5, the MC model can be programmed into two main loops: an outer loop that advances one Δt at a time (the temporal loop) and an inner loops that advances one Δx at a time (the spatial loop) for the different fields: incident radiation field, ASE radiation field, and the number density field.

Extension to multidimensional domain is straightforward (as illustrated in the lower panel) via the following three modifications. First, the computational domain is discretized into 2D or 3D arrays of cells of size Δx. Second, the excitation packets are divided into multiple sub-packets according to the spatial intensity profile of the excitation pulse, and these sub-packages are sent into multiple cells at the same time. And finally, when the MC model makes a spatial advancement of Δx, it determines not only whether a photon packet still remains in the computational domain, but also the location (i.e., index of the new cell) of the packet after the advancement. As to implementation, one more loop is added (in addition to the temporal and spatial loop mentioned above) to cycle through all the cells.

To validate the MC model, we applied the MC model to example problems and compared the results to those obtained from the rate equations and documented experimental results. These example problems include the two-photon LIF measurement of O and H atoms in flames and plasmas [81, 84, 93]. Good agreements were obtained in all example calculations, and here we report the validation calculations for the case of H atoms in flame experiments. This calculation again simulated the two-photon LIF measurements of H atoms in a $H_2/O_2/Ar$ flame [81] which was reported in Figure 4-2. We solved this problem using both the rate equations shown in Section 4.2 and the MC model described here. The temporal evolution of LIF signal and the ASE signal are reported in the upper and lower panels of Figure 4-6, respectively, showing the

agreement of two models. A laser pulse energy of 220 μJ is chosen, where the ASE signal is appreciable but not yet saturated.

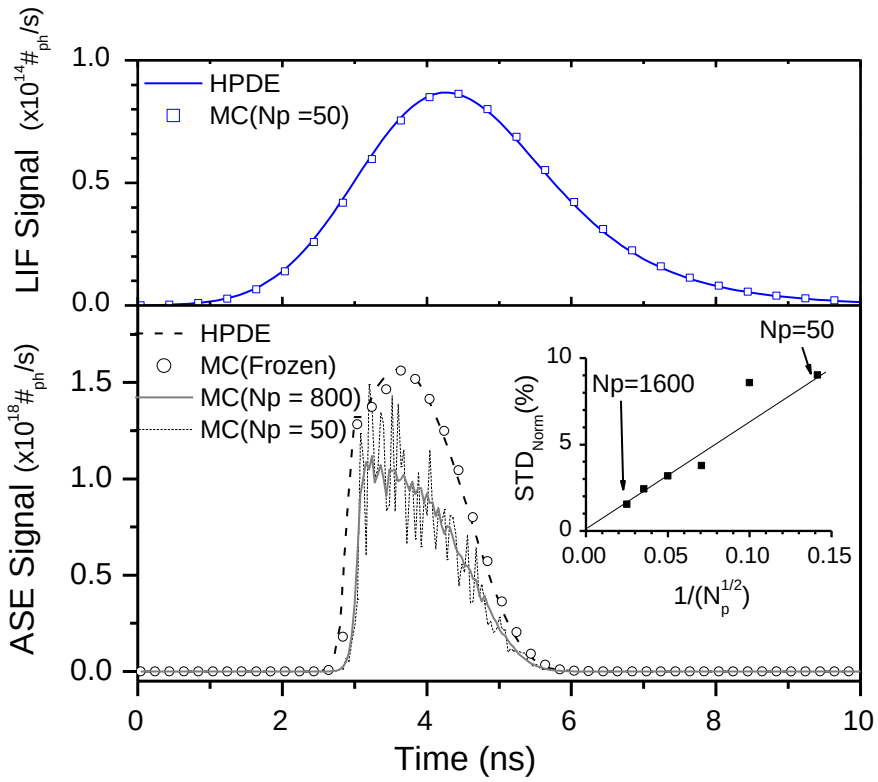

Figure 4-6. Comparison between HPDE and MC calculations in a 1D geometry.

In these calculations, the intensity profile was assumed to have a top-hat spatial distribution, so that Eq. (4.1) can be solved using the solver of hyperbolic partial differential equations as described in [102]. In the MC model, the time step Δt was set to be 0.4 ps, resulting in a total number of temporal steps (N) of 2.5×10^4 and a spatial step size (Δx) of 120 μm. The measurement volume was therefore discretized into 250 cubic cells in the x-direction, each with a size of 120×120×120 μm. For the LIF calculation, the LIF photons emitted from the 50 cells at

the center of the measurement volume were counted, with an assumed collection efficiency of 0.1%. For the ASE calculation, the ASE photons exited from the front surface (i.e., the front surface of the 250th cell) were counted. Because Eq. (4.1) assumes ASE photon only propagates along the x-axis, the MC model also restricted the ASE photons to be in the x-axis. We therefore termed this MC calculation a zero-dimensional (0D) MC model, since the calculations were made 1) for cells only in the x-direction, 2) for a laser pulse with a top-hat spatial profile, and 3) with ASE photons restricted in the x-direction. The MC calculations when condition 3) is removed were termed 1D MC model. Eq. (4.1) and the 0D MC model are based on the exactly the same assumptions and yields the same results as shown in Figure 4-6. Both Eq. (4.1) and the 0D MC model reveal that the onsite of the ASE signal lags behind that of the LIF signal, and the duration of the ASE is shorter than that of the LIF signal, which have both been experimentally observed[106]. The reasons are that the ASE signal does not become appreciable until there is sufficient population inversion built up between level 2 and 3, explaining the later onset of the ASE signal. Once equilibrium is reached between level 3 and 2, the population inversion becomes insufficient to produce ASE signal, explaining the shorter duration of the ASE signal.

Also reported in Figure 4-6 is the evaluation of statistical noise of Monte Carlo method, as shown in the inset figure of the lower panel. Statistical theory shows that the error of Monte Carlo should scale with the number of photons sent in the system as $\sim N_p^{-0.5}$, where N_p is the number of photons generated in a cell at each time step. We therefore performed used a series of calculations with N_p ranging from 50 to 1600. The error is evaluated by the standard deviation of a noisy temporal evolution curve at a certain N_p with respect to a median filter smoothed curve calculated from the highest N_p. The expected $N_p^{-0.5}$ scaling relationship is well reproduced as shown in the inset figure.

A quantity typically measured in practice is the number of LIF and ASE photons generated during an excitation pulse. This quantity can be obtained by integrating the temporal profiles shown in Figure 4-6 and the results are shown in Figure 4-7 at various excitation energies, denoted as *E*. The comparison in Figure 4-7 again shows the close agreement between Eq. (4.1) and the MC model in both the integrated LIF and ASE signals. Both methods reveal the well-known trend of the LIF and ASE signals observed in previous studies [81, 84, 86, 89, 93]. The calculations also reasonably agree with the experiments. For example, the experiments in [81] showed a 20~30× increase in the ASE signal when the excitation energy increased from 200 to 600 μJ, compared to a ~20× increase predicted by the calculations. The discrepancy is partially due to the uncertainties in the parameters assumed in the calculations.

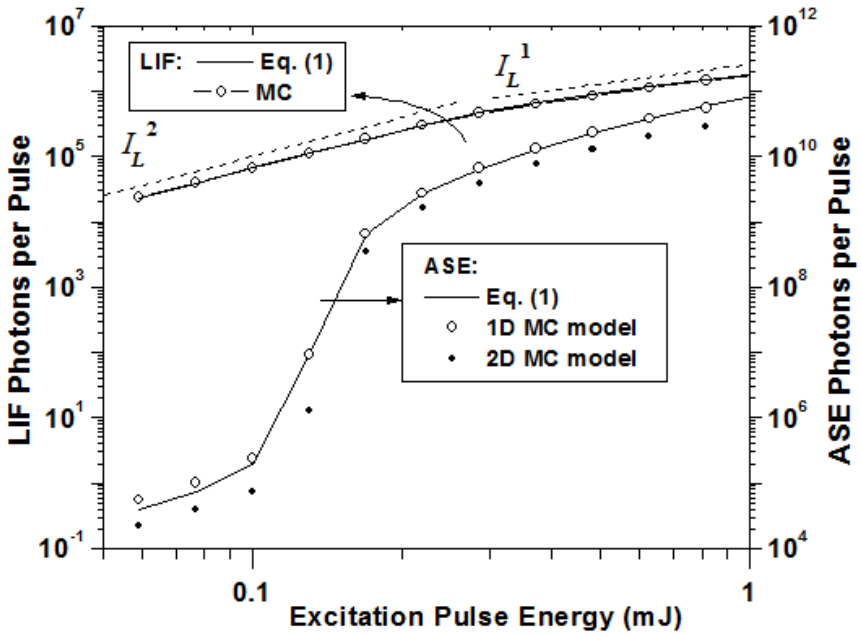

Figure 4-7. Comparison of the integrated number of LIF and ASE photons by Eq. (4.1)and the MC model.

In summary, the MC model was validated in various example problems studied previously. The results obtained from the MC model were compared to both those obtained from the well-established rate equations and experiments, and agreements were demonstrated.

4.5 Evaluation of ASE distortion in 2D experiments

In this section, the MC model is applied to quantify the 1D assumption made in the rate equations. As discussed in Section II, this assumption can be justified when the measurement volume is long and thin. The aspect ratio, defined as the ratio of length (*x*-scale) to the height (*z*-scale) of the measurement volume, can be used to characterize the shape of the measurement volume. The 1D rate equations are therefore expected to be accurate when the aspect ratio of the measurement volume is high, which is examined by the results shown in Figure 4-6. We next applied the MC model to investigate the cases where the measurement volume has a lower aspect ratio and can no longer be approximated as a 1D volume.

Figure 4-8 and Figure 4-9 show the LIF and ASE signals, respectively, obtained when the measurement volume is a rectangular cuboid with a length of 3 cm, a height of 0.3 cm, and a width (thickness) of 300 μm. Such a measurement volume has an aspect ratio of 10, and resembles a quasi-2D measurement with a laser sheet. The calculations were made for O atoms, with a uniform mole fraction of 1.2% at 1 atm and 2490 K. These conditions were determined by an equilibrium calculation of a CH_4/air premixed flame with an equivalent ratio of 0.7 to simulate a typical flame measurement over a flat burner. The excitation pulse was assumed to have a Gaussian temporal profile with FWHM of 3.5 ns, a Gaussian spatial profile in the *z*-direction with a FWHM of 2.23 mm, and a top-hat spatial profile in the *y*-direction. The total excitation duration

was taken to be 7 ns, and the pulse energy taken to be 2.2 mJ. The spectroscopic data of O atoms used were summarized in Table 4-1. The quenching cross sections from level 2 and 3 are taken as $2\times10^{9}s^{-1}$, according to [85].

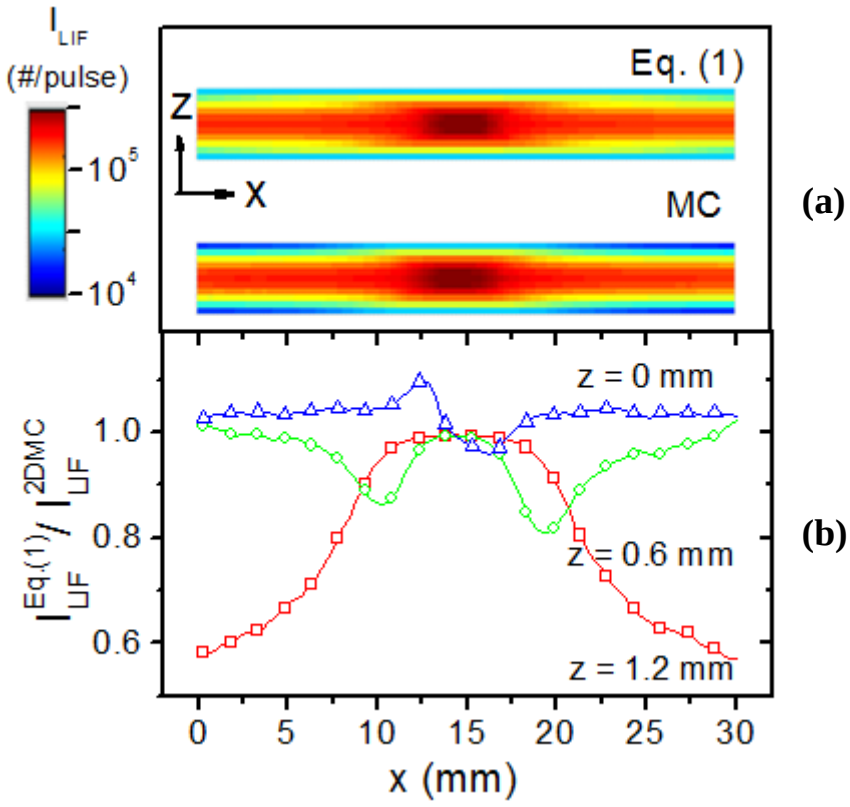

Figure 4-8. Comparison of the LIF signal obtained from Eq. (4.1) and 2D MC model at an aspect ratio of 10. Panel (a). the LIF signal fields. Panel (b). the ratio of the LIF signal calculated from the rate equations and the 2D MC model at selected *z*'s.

In the MC model, the time step Δt was set to be 1 ps, resulting in a number of temporal steps (N) of 7×10^{3}, and a spatial step size (Δx) of 300 μm. The measurement volume was therefore discretized into an array of 300 (x) ×10 (z) ×1 (y) cubic cells. The excitation profile was discretized into 10 bins in the z-direction, and the pulse intensity in each bin was used to

determine the number of photons in each sub-packet to be sent into the corresponding cell. In the rate equation calculations, the computation domain was discretized into 10 strips along the *x*-direction, each strip with a height of 300 μm. Eq. (4.1) was then solved for each strip at the laser intensity in the corresponding bin, a common practice used in past work[93]. Such practice essentially assumes the complete decoupling of the ASE effects along the *z*-direction, so that the 1D rate equations can be solved independently for at different *z*.

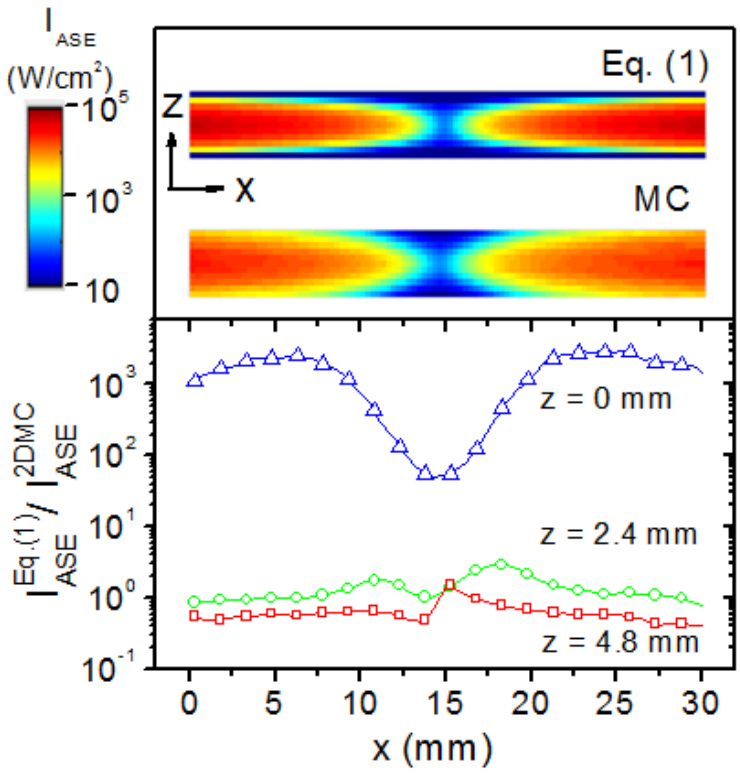

Figure 4-9. Comparison of the ASE signal obtained from Eq. (4.1) and 2D MC model at an aspect ratio of 10. Panel (a). ASE radiation fields. Panel (b). the ratio of the ASE signal calculated from the rate equations and the 2D MC model at selected *z*'s.

As shown in Panel (a) of Figure 4-8, the distribution of the LIF photons agree qualitatively between the rate equations (RE) and the 2D MC model. As shown in Panel (b), the quantitatively agreement is reasonable near the center of the measurement domain (e.g., when z = 1.2 mm); however, large deviation is observed at the edge of the measurement domain. Similar observations are made for the ASE signal (or the radiation field), as shown in Figure 4-9.

Figure 4-10 and Figure 4-11 show the results for a measurement volume of an aspect ratio of 2.5 (the dimension of the measurement volume is 3 cm (x) × 1.2 cm (z) × 300 μm (y). The calculations were made in a similar fashion as those in Figure 4-8 and Figure 4-9, except that 1) the pulse energy was taken to be 8.8 mJ in this case and the spatial FWHM in the z-direction taken to be 8.9 mm, 2) the measurement volume was discretized into 40 cells in the z-direction, and 3) the excitation pulse was discretized into 40 bins in the z-direction. As shown in Panel (a) of Figure 4-10, the LIF distribution still agree qualitatively; however, quantitative disagreement can be observed in Panel (b) of Figure 4-11. As can be seen from Figure 4-10, at this aspect ratio, the rate equations and the MC model disagree both qualitatively and quantitatively. Panel (a) shows that the radiation field is along the x-direction, because of the 1D assumption. However, the MC model shows that at such aspect ratio, the radiation field also exists substantially along other directions because there is sufficient gain length in other directions to amplify the ASE photons.

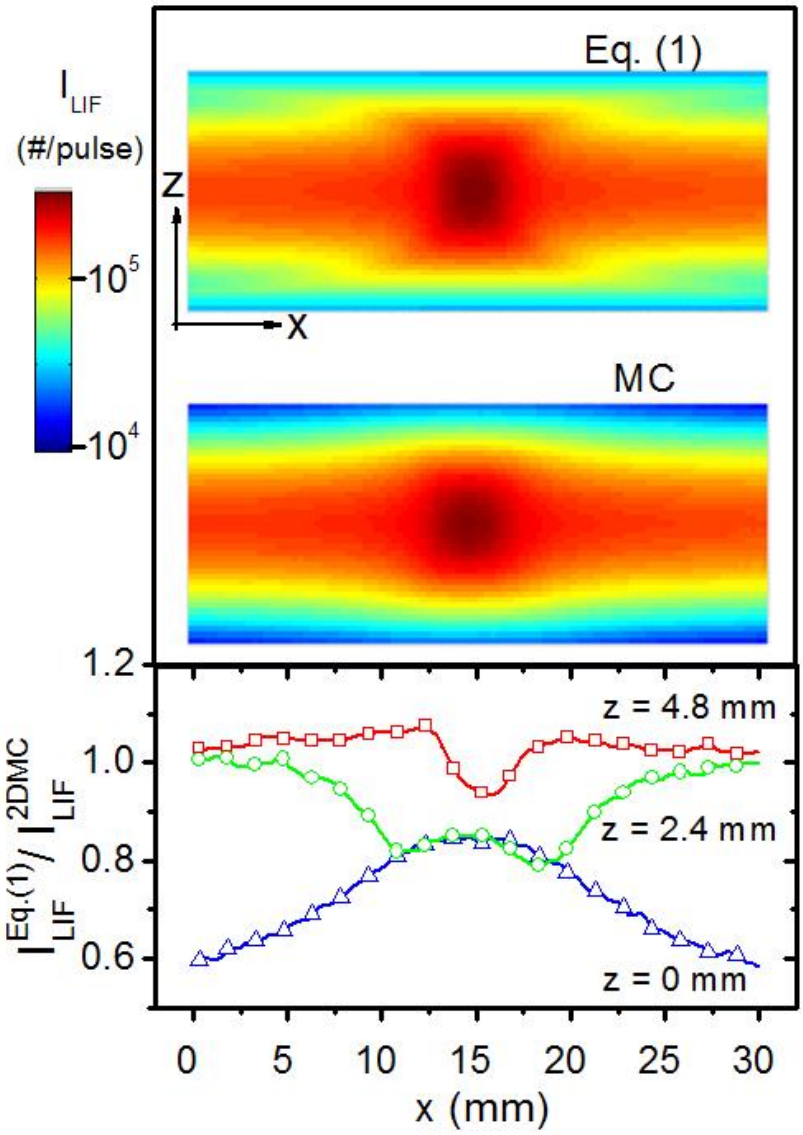

Figure 4-10. Comparison of the LIF signal obtained from Eq. (1) and 2D MC model at an aspect ratio of 2.5. Panel (a). the distribution of the LIF signal at each cell. Panel (b). the ratio of the LIF signal calculated from the rate equations and the 2D MC model at selected *z*'s

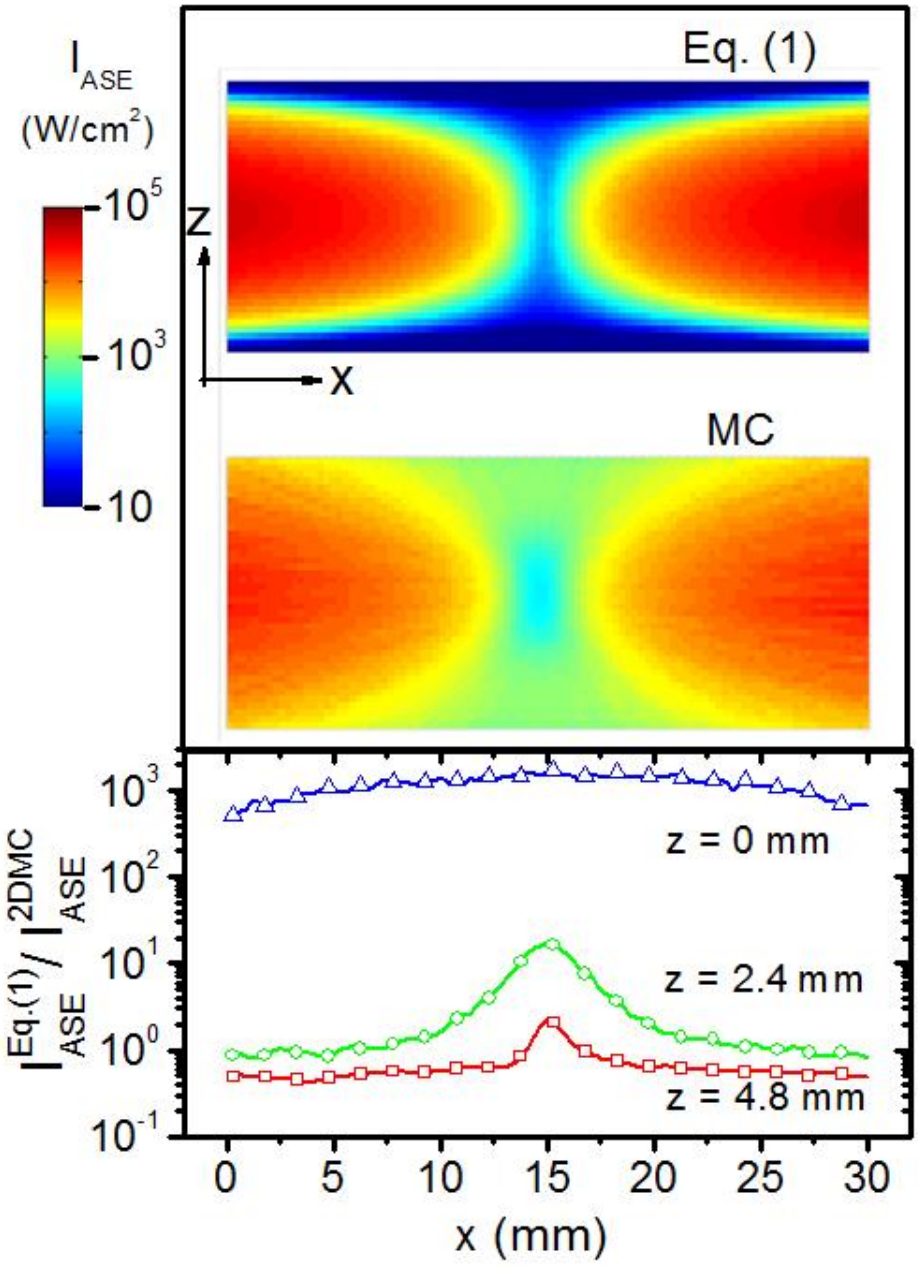

Figure 4-11. Comparison of the ASE signal from Eq. (1) and 2D MC model at an aspect ratio of 2.5. Panel (a). the distribution of the ASE signal at each cell. Panel (b). the ratio of the ASE signal calculated from the rate equations and the 2D MC model at selected *z*'s.

In summary, this section reports the application of the MC model to quantify the accuracy of the rate equations and to investigate the 2D measurement of two-photon LIF. The results from the MC model suggest that 1) the 1D assumption in rate equations causes noticeable error even when the measurement volume has a large aspect ratio, 2) the error becomes larger, both qualitatively and quantitatively, when the aspect ratio decreases. We expect these results and observations to be valuable for the design of experiments involving two-photon processes, and for the quantitative interpretation of the two-photon LIF signal. For example, the nonlinear effects caused by the ASE represent a major challenge in the applicant of two-photon LIF, complicating the inference of the concentration of the target species from the LIF signal.

Our ongoing work attempts to seek approaches to overcome this challenge. On possible approach involves an iterative process using the MC model developed. This approach 1) starts by guessing a concentration of the target species, 2) then calculates the LIF (or ASE) signal based on this guess using the MC model and compare the calculated signals to the measurements, and finally 3) adjust the guess based on this comparison and iterate until the calculated signals agree with the measurements

.

Chapter 6

Conclusion and outlook

In this final chapter, the results from this work are summarized, followed by the suggested future work and a discussion of the outlook of the PDS technique.

This work introduced a new diagnostic technique based on PDS for the multidimensional measurements of mixture fraction in reactive flows. This technique utilizes the complete PD of the precursor and its products to represent mixture fraction. It exploits the friendly spectroscopic properties of the target photofragment to overcome the limitations of existing techniques and to enable multidimensional imaging of mixture fraction. An experimental demonstration of the technique, conducted in a non-premixed jet flame with molecular I_2 as the precursor and atomic I as the target photofragment, was presented. The results obtained suggest that the PDS-based technique enables several attractive advantages. It circumvents the need to simultaneously monitor multiple species, enjoys higher signal strength due to the strong LIF transitions of atomic I compared to the Raman scattering used in existing techniques, and avoids the usual complexity in interpreting LIF signals due to the simple structure of atoms and the relatively large photoionization cross section of atomic I. The performance of the measurements was analyzed,

suggesting the potential to provide 2D imaging of ξ with good SNR across a reasonably large field-of-view.

The TPLIF technique used to probe the photofragment was studied, with the focus on the possible ASE distortion. Besides analysis in 1D using a system of hyperbolic differential equations, a Monte Carlo simulation approach is applied for 2D problems. These models are able to explain the scaling of LIF and ASE signals, and the distortion of LIF signal due to ASE observed in previous experiments. The simulation also suggests the possibilities of correcting ASE distortion using certain experimental schemes; therefore enhance the applicable range and accuracy of TPLIF technique for flow imaging purposes.

Future research includes the following directions: 1) Test the technique to hydrocarbon flames in line imaging, using 266 nm PD laser which is available in our lab. The demonstration of 2D imaging in hydrocarbon flame requires KrF laser. 2) Develop 2D models for analyzing ASE in TPLIF with enhanced accuracy by include the line shape modeling. Experimental validate of the models are underway using iodine to quantify the onset and magnitude of ASE distortion, although such distortion was not observed the current experiments at low seeding levels.

A limitation of the iodine-based diagnostics is the inherent differential diffusion effect. This limitation is fundamental due to the mismatch between the transport properties of I_2 and those of the typical species in flames. On the one hand, differential diffusion is expected to be smaller in heavier hydrocarbon flames; on the other hand, the PDS-based technique can potentially provide a method to study differential diffusion quantitatively in reactive flows. Different precursors can be used to adjust and control the magnitude of the differential diffusion effects.

The potential application areas of the PDS-based technique are not limited to mixture fraction measurements. For example, temperature measurement can possibly be performed based on the target photofragment. Compared with traditional two-line LIF thermometry, such PDS-based thermometry has the potential to enable stronger signals and simplify the interpretations of the signals. A key aspect for all the above applications (mixture fraction measurement, study of differential diffusion, and PDS-based thermometry) involves the selection of a proper precursor with proper PD characteristics, desired transport properties, and attractive spectroscopic properties for the measurements of the target property.

Reference

1. *http://www.eia.doe.gov/pub/international/iealf/table18.xls* Energy Information Administration, U.S. Department of Energy., 2008.

2. Bilger, R.W., et al. *Paradigms in turbulent combustion research*. 2005.

3. Barlow, R.S., *Laser diagnostics and their interplay with computations to understand turbulent combustion.* Proceedings of the Combustion Institute, 2007. **31**: p. 49-75.

4. Kohse-Hoinghaus, K., et al., *Combustion at the focus: laser diagnostics and control.* Proceedings of the Combustion Institute, 2005. **30**: p. 89-123.

5. Eckbreth, A.C., *Laser Diagnostics for Combustion Temperature and Species*. 1996, New York: CRC.

6. Kohse-Hoinghaus, K. and J.B. Jeffries, eds. *Applied Combustion Diagnostics.* 2002, Taylor & Francis: New York.

7. Bilger, R.W., *Structure of diffusion flames.* Combustion Science and Technology, 1976. **13**(1-6): p. 155-170.

8. Masri, A.R., R.W. Dibble, and R.S. Barlow, *The structure of turbulent nonpremixed flames revealed by Raman-Rayleigh-LIF measurements.* Progress in Energy and Combustion Science, 1996. **22**(4): p. 307-362.

9. Frank, J.H. and R.S. Barlow. *Simultaneous Rayleigh, Raman, and LIF measurements in turbulent premixed methane-air flames*. in *Proceeding of Combustion Institute*. 1998.

10. Karpetis, A.N. and R.S. Barlow, *Measurements of scalar dissipation in a turbulent piloted methane/air jet flame.* Proceedings of the Combustion Institute, 2003. **29**: p. 1929-1936.

11. Barlow, R.S. and A.N. Karpetis, *Measurements of scalar variance, scalar dissipation, and length scales in turbulent piloted methane/air jet flames.* Flow Turbulence and Combustion, 2004. **72**(2-4): p. 427-448.

12. Karpetis, A.N., et al., *Laser imaging system for determination of three-dimensional scalar gradients in turbulent flames.* Optics Letters, 2004. **29**(4): p. 355-357.

13. Starner, S.H., et al., *Measurement of conserved scalars in turbulent-diffusion flames.* Combustion Science and Technology, 1992. **86**(1-6): p. 223-236.

14. Starner, S.H., et al. *Multispecies measurements and mixture fraction imaging in turbulent-diffusion flames*. 1994.

15. Frank, J.H., et al., *Mixture fraction imaging in furbulent nonpremixed hydrocarbon flames*, in *Proceedings of the 25th International Symposium on Combustion*. 1994, Combustion Institute: Pittsburgh, PA. p. 1159-1166.

16. Frank, J.H., S.A. Kaiser, and M.B. Long, *Multiscalar imaging in partially premixed jet flames with argon dilution.* Combustion and Flame, 2005. **143**(4): p. 507-523.

17. Sutton, J.A. and J.F. Driscoll, *A method to simultaneously image two-dimensional mixture fraction, scalar dissipation rate, temperature and fuel consumption rate fields in a turbulent non-premixed jet flame.* Experiments in Fluids, 2006. **41**(4): p. 603-627.

18. Hsu, A.G., et al., *Mixture fraction imaging in turbulent non-premixed flames with two-photon LIF of krypton.* Proceedings of the Combustion Institute, 2011. **33**: p. 759-766.

19. Fielding, J., A.M. schaffer, and M.B. Long, *Three-scalar imaging in turbulent non-premixed flames of methane*, in *Proceedings of the 27th International Symposium on Combustion* 1998, Combustion Institute: Pittsburg, PA. p. 1007-1014.

20. Fielding, J., et al. *Polarized/depolarized Rayleigh scattering for determining fuel concentrations in flames*. in *Proceedings of the Combustion Institute*. 2002.

21. Zhao, Y., C.N. Tong, and L. Ma, *Assessment of a Novel Flow Visualization Technique Using Photodissociation Spectroscopy.* Applied Spectroscopy, 2009. **63**(2): p. 199-206.

22. Zhao, Y., C.N. Tong, and L. Ma, *Demonstration of a New Laser Diagnostic Based on Photodissociation Spectroscopy for Imaging Mixture Fraction in a Non-premixed Jet Flame.* Applied Spectroscopy, 2010. **64**(4): p. 377-383.

23. Laurendeau, N.M., *Temperature-measurements by light-scattering methods.* Progress in Energy and Combustion Science, 1988. **14**(2): p. 147-170.

24. Miles, R.B., W.R. Lempert, and J.N. Forkey, *Laser Rayleigh scattering.* Measurement Science & Technology, 2001. **12**(5): p. R33-R51.

25. Frank, J.H. and S.A. Kaiser, *High-resolution imaging of dissipative structures in a turbulent jet flame with laser Rayleigh scattering.* Experiments in Fluids, 2008. **44**(2): p. 221-233.

26. Barlow, R.S. and P.C. Miles, *A shutter-based line-imaging system for single-shot Raman scattering measurements of gradients in mixture fraction.* Proceedings of the Combustion Institute, 2000. **28**: p. 269-277.

27. Daily, J.W., *Laser induced fluorescence spectroscopy in flames.* Progress in Energy and Combustion Science, 1997. **23**(2): p. 133-199.

28. Peters, N., *Turbulent Combustion*. 2000, Cambridge, UK: Cambridge University Press.

29. Bilger, R.W. and R.W. Dibble, *Differential molecular-diffusion effects in turbulent mixing* Combustion Science and Technology, 1982. **28**(3-4): p. 161-172.

30. Chen, Y.C. and M.S. Mansour, *Measurements of scalar dissipation in turbulent hydrogen diffusion flames and some implications on combustion modeling.* Combustion Science and Technology, 1997. **126**(1-6): p. 291-313.

31. Sutton, J.A. and J.F. Driscoll, *Imaging of local flame extinction due to the interaction of scalar dissipation layers and the stoichiometric contour in turbulent non-premixed flames.* Proceedings of the Combustion Institute, 2007. **31**: p. 1487-1495.

32. Boogaarts, M.G.H., et al., *Quantitative two-photon laser-induced fluorescence measurements of atomic hydrogen densities, temperatures, and velocities in an expanding thermal plasma.* Review of Scientific Instruments, 2002. **73**(1): p. 73-86.

33. Zhao, Y., C. Tong, and L. Ma, *Kinetics of I_2 and HI photodissociation with implications in flame diagnostics.* Applied Physics B: Lasers and Optics: p. 1-10.

34. Smith, G.P., et al. *GRI-MECH3.0*. [cited; Available from: http://www.me.berkeley.edu/gri_mech/

35. Babushok, V., et al., *Influence of CF3I, CF3Br, and CF3H on the high-temperature combustion of methane.* Combustion and Flame, 1996. **107**(4): p. 351-367.

36. Noto, T., et al., *Inhibition effectiveness of halogenated compounds.* Combustion and Flame, 1998. **112**(1-2): p. 147-160.

37. Luo, C., B.Z. Dlugogorski, and E.M. Kennedy. *Influence of CF3I and CBrF3 on methanol-air and methane-air premixed flames*. 2008.

38. Sato, H., *Photodissociation of simple molecules in the gas phase.* Chemical Reviews, 2001. **101**(9): p. 2687-2725.

39. Saiz-Lopez, A., et al., *Absolute absorption cross-section and photolysis rate of I_2.* Atmospheric Chemistry and Physics, 2004. **4**: p. 1443-1450.

40. Tellinghuisen, J. and L.F. Phillips, *Kinetics of I_2 following photolysis at 1930 A : Temperature dependence of A'-state quenching.* Journal of Physical Chemistry, 1986. **90**(21): p. 5108-5120.

41. Clear, R.D. and K.R. Wilson, *Assignment of continuous spectra by photofragment spectroscopy: C state of I_2.* Journal of Molecular Spectroscopy, 1973. **47**(1): p. 39-44.

42. Mulliken, R.S., *Iodine Revisited.* Journal of Chemical Physics, 1971. **55**(1): p. 288-309.

43. deJong, W.A., L. Visscher, and W.C. Nieuwpoort, *Relativistic and correlated calculations on the ground, excited, and ionized states of iodine.* Journal of Chemical Physics, 1997. **107**(21): p. 9046-9058.

44. Tellinghuisen, J., *Transitions strength in the visible-infrared absorption-spectrum of I_2.* Journal of Chemical Physics, 1982. **76**(10): p. 4736-4744.

45. Macdonald, L.H. and R.L. Strong, *Excited-states in Bromine photoexcitation and recombination.* Journal of Physical Chemistry, 1991. **95**(18): p. 6940-6945.

46. Rosker, M.J., M. Dantus, and A.H. Zewail, *Femtosecond clocking of the chemical-bond* Science, 1988. **241**(4870): p. 1200-1202.

47. Capelle, G.A. and H.P. Broida, *Lifetimes and quenching cross sections of I^2 ($B\,^3\Sigma 0_u^+$).* journal of chemical physics, 1973. **58**: p. 11.

48. Broadben.Tw and A.B. Callear, *Quantum yields for collisionally induced dissociation of excited I_2 B to I ($5\,^2P_{1/2}$) + I ($5\,^2P_{3/2}$) - nonequilibrium effects in combination of atoms.* Journal of the Chemical Society-Faraday Transactions Ii, 1972. **68**: p. 1367-&.

49. Tellingh.J, *Resolution of visible-infrared absorption-spectrum of I_2 to 3 contributing transitions.* Journal of Chemical Physics, 1973. **58**(7): p. 2821-2834.

50. Herzberg, G., *Molecular spectra and molecular structure. Volume I - spectra of diatomic molecules*. 1950, Florida: Kerieger Publishing Company.

51. Kireev, S.V. and S.Z. Shnyrev, *Rotational relaxation of the levels of the B state in I-127 and I-129 molecular iodine isotopes excited by 633-nm radiation of a He-Ne laser.* Laser Physics, 1999. **9**(3): p. 614-625.

52. Lawrence, W.G., et al., *Inelastic collision dynamics of vibrationally excited I-2(X).* Journal of Chemical Physics, 1997. **106**(1): p. 127-141.

53. Masiello, T., N. Vulpanovici, and J.W. Nibler, *Fluorescence lifetime and quenching of iodine vapor*. Journal of Chemical Education, 2003. **80**(8): p. 914-917.

54. Hiller, B. and R.K. Hanson, *Properties of the iodine molecule relevant to laser-induced fluorescence experiments in gas-flows.* Experiments in Fluids, 1990. **10**(1): p. 1-11.

55. Hwang, H.J. and M.A. Elsayed, *Symmetry and product-state correlation of the C-state of I_2 in the 304 nm region.* Journal of Physical Chemistry, 1991. **95**(21): p. 8044-8047.

56. Alekseyev, A.B., et al., *On the ultraviolet photofragmentation of hydrogen iodide.* Journal of Chemical Physics, 2000. **113**(15): p. 6174-6185.

57. Waschewsky, G.C.G., R. Horansky, and V. Vaida, *Effect of dimers on the temperature-dependent absorption cross section of methyl iodide.* Journal of Physical Chemistry, 1996. **100**(28): p. 11559-11565.

58. Mulliken, R.S., *Intensities in Molecular Electronic Spectra X. Calculations on Mixed - Halogen, Hydrogen Halide, Alkyl Halide, and Hydroxyl Spectra.* Journal of Chemical Physics, 1940. **8**: p. 14.

59. Gendron, D.J. and J.W. Hepburn, *Dynamics of Hl photodissociation in the A band absorption via H-atom Doppler spectroscopy.* Journal of Chemical Physics, 1998. **109**(17): p. 7205-7213.

60. Langford, S.R., et al., *On the UV photodissociation dynamics of hydrogen iodide.* Chemical Physics, 1998. **231**(2-3): p. 245-260.

61. Regan, P.M., et al., *The UV photodissociation of HI revisited: REMPI measurements of I($P_{1/2}$) atom spin-orbit branching fractions.* Chemical Physics Letters, 1999. **315**(3-4): p. 187-193.

62. Kitsopoulos, T., et al. *Application of ion imaging to the study of unimolecular and bimolecular reactions*. in *SPIE*. 1993.

63. Le Roy, R.J., G.T. Kraemer, and S. Manzhos, *1 potential, 2 potentials, 3 potentials-4: Untangling the UV photodissociation spectra of HI and DI.* Journal of Chemical Physics, 2002. **117**(20): p. 9353-9369.

64. Chichinin, A.I., *Chemical properties of electronically excited halogen atoms X($^2P_{1/2}$) (X=F,Cl,Br,I).* Journal of Physical and Chemical Reference Data, 2006. **35**(2): p. 869-928.

65. Bannister, J.J., et al., *self-induced transparency and resontant self-focusing in atomic iodine vapor*. Physical Review Letters, 1980. **44**(16): p. 1062-1065.

66. Carroll, D.L., *Chemical laser modeling with genetic algorithms.* Aiaa Journal, 1996. **34**(2): p. 338-346.

67. Kaledin, A.L., M.C. Heaven, and K. Morokuma, *Theoretical prediction of the rate constant for I+O-2(a(1)Delta(g)) electronic energy transfer: A surface-hopping trajectory study.* Journal of Chemical Physics, 2001. **114**(1): p. 215-224.

68. Bourig, A., et al., *Numerical modeling of H-2-O-2 flames involving electronically-excited species O-2(a(1)Delta(g)), O(D-1) and OH((2)Sigma(+)).* Proceedings of the Combustion Institute, 2009. **32**: p. 3171-3179.

69. Alekseyev, A.B., H.P. Liebermann, and R.J. Buenker, *An ab initio study of the CH_3I photodissociation. I. Potential energy surfaces.* Journal of Chemical Physics, 2007. **126**(23).

70. Jung, Y.J., et al., *Photoelectron imaging spectroscopy for (2+1) resonance-enhanced multiphoton ionization of atomic iodine produced from A-band photolysis of CH_3I.* Journal of Chemical Physics, 1997. **107**(18): p. 7187-7193.

71. Baklanov, A.V., et al., *Vacuum ultraviolet oscillator strengths of iodine atoms in the I($^2P_{1/2}$) and I($^2P_{3/2}$) states.* Journal of Physics B-Atomic Molecular and Optical Physics, 1997. **30**(8): p. L259-L264.

72. Brewer, P., et al., *Measurement of the relative populations of I($^2P_{1/2}$) and I($^2P_{3/2}$) by laser-induced vacuum ultraviolet fluorescence* Journal of Chemical Physics, 1983. **79**(2): p. 720-723.

73. Tiee, J.J., et al., *Two-photon laser-induced fluorescence studies of HS radical, DS radicals, and I atoms.* Chemical Physics Letters, 1983. **96**(4): p. 422-425.

74. Lokhman, V.N., D.D. Ogurok, and E.A. Ryabov, *Multiphoton ionization of iodine atoms and CF_3I molecules by XeCl laser radiation.* European Physical Journal D, 2008. **46**(1): p. 59-67.

75. Fiechtner, G.J. and J.R. Gord, *Absorption and the dimensionless overlap integral for two-photon excitation.* Journal of Quantitative Spectroscopy & Radiative Transfer, 2001. **68**(5): p. 543-557.

76. Davis, S.J., et al., *Measurements of pressure-broadening coefficients for the F '=3 <- F ''=4 hyperfine line of the ($^2P_{1/2}$) and ($^2P_{3/2}$) transition in atomic iodine.* Journal of Physical Chemistry A, 2002. **106**(36): p. 8323-8327.

77. Robicheaux, F. and C.H. Greene, *Regularities in calculated photoionization cross-sections for the halogens.* Physical Review A, 1992. **46**(7): p. 3821-3833.

78. Hancock, G., et al., *Diode laser based studies of the UV photolysis of molecular iodine.* Physical Chemistry Chemical Physics, 2009. **11**(30): p. 6415-6423.

79. Perona, P. and J. Malik, *Sclae-space and edge-detection using anisotropic diffusion.* Ieee Transactions on Pattern Analysis and Machine Intelligence, 1990. **12**(7): p. 629-639.

80. Cai, J. and C.N. Tong, *A conditional sampling-based method for noise and resolution corrections for scalar dissipation rate measurements.* Physics of Fluids, 2009. **21**(6).

81. Goldsmith, J.E.M., *Two photon-excited stimulated-emission from atomic-hydrogen in flames.* Journal of the Optical Society of America B-Optical Physics, 1989. **6**(11): p. 1979-1985.

82. Tserepi, A.D., E. Wurzberg, and T.A. Miller, *Two-photon-excited stimulated emission from atomic oxygen in rf plasmas: Detection and estimation of its threshold.* Chemical Physics Letters, 1997. **265**(3-5): p. 297-302.

83. Niemi, K., V. Schulz-von der Gathen, and H.F. Dobele, *Absolute calibration of atomic density measurements by laser-induced fluorescence spectroscopy with two-photon excitation.* Journal of Physics D-Applied Physics, 2001. **34**(15): p. 2330-2335.

84. Frank, J.H., et al., *Comparison of nanosecond and picosecond excitation for two-photon laser-induced fluorescence imaging of atomic oxygen in flames.* Applied Optics, 2004. **43**(12): p. 2588-2597.

85. Frank, J.H. and T.B. Settersten, *Two-photon LIF imaging of atomic oxygen in flames with picosecond excitation.* Proceedings of the Combustion Institute, 2005. **30**: p. 1527-1534.

86. Alden, M., U. Westblom, and J.E.M. Goldsmith, *2-photon-excited stimulated-emission from atomic oxygen in flames and cold gases.* Optics Letters, 1989. **14**(6): p. 305-307.

87. Auyeung, R.C.Y., et al., *Stimulated-emission atomic-hydrogen at 656 nm.* Optics Communications, 1990. **79**(3-4): p. 207-210.

88. Bergstrom, H., H. Lundberg, and A. Persson, *Investigations of stimulated-emission on B-A lines in CO.* Zeitschrift Fur Physik D-Atoms Molecules and Clusters, 1991. **21**(4): p. 323-327.

89. Amorim, J., et al., *2-photon laser-indeced fluorescence and amplified spontaneous emission atom concentration measurements in O_2 and H_2 dischargers.* Journal of Applied Physics, 1994. **76**(3): p. 1487-1493.

90. Kulatilaka, W.D., et al., *Comparison of nanosecond and picosecond excitation for interference-free two-photon laser-induced fluorescence detection of atomic hydrogen in flames.* Applied Optics, 2008. **47**(26): p. 4672-4683.

91. Casperson, L.W., *Rate-equation approximations in high-gain lasers.* Physical Review A, 1997. **55**(4): p. 3073-3085.

92. Daily, J.W., *Use of rate equations to describe laser excitation in flames.* Applied Optics, 1977. **16**(8): p. 2322-2327.

93. Amorim, J., G. Baravian, and J. Jolly, *Laser-induced resonance fluorescence as a diagnostic technique in non-thermal equilibrium plasmas.* Journal of Physics D-Applied Physics, 2000. **33**(9): p. R51-R65.

94. Huang, Y.L. and R.J. Gordon, *The effect of amplified spontaneous emission on the measurement of the multiplet state distribution of ground-state oxygen-atoms.* Journal of Chemical Physics, 1992. **97**(9): p. 6363-6368.

95. Settersten, T.B. and M.A. Linne, *Modeling pulsed excitation for gas-phase laser diagnostics.* Journal of the Optical Society of America B-Optical Physics, 2002. **19**(5): p. 954-964.

96. Allen, L. and G.I. Peters, *Amplified spontaneous emission and external signal amplification in an inverted medium.* Physical Review A, 1973. **8**(4): p. 2031-2047.

97. Riley, M.E., *Growth of parametric fields in (2+1)-photon laser ionization of atomic oxygen.* Physical Review A, 1990. **41**(9): p. 4843-4856.

98. Hilborn, R.C., *Einstein coefficients, cross-sections, F values, dipole-moments, and all that.* American Journal of Physics, 1982. **50**(11): p. 982-986.

99. Partridge, W.P. and N.M. Laurendeau, *Formulation of a dimensionless overlap fraction to account for spectrally distributed interactions in flurescence studies.* Applied Optics, 1995. **34**(15): p. 2645-2647.

100. Casperson, L.W., *Threshold characteristics of mirrorless lasers.* Journal of Applied Physics, 1977. **48**(1): p. 256-262.

101. Pert, G.J., *Collisional cross relaxation effects in amplified spontaneous emssion lasers.* Physical Review A, 1994. **50**(5): p. 4412-4414.

102. Shampine, L.F., *Solving Hyperbolic PDEs in MATLAB.* Applied Numerical Analysis & Computational Mathematics, 2005. **2**(3): p. 13.

103. Juvela, M. and P. Padoan, *Dust emission from inhomogeneous interstellar clouds: Radiative transfer in 3D with transiently heated particles.* Astronomy & Astrophysics, 2003. **397**(1): p. 201-212.

104. Gandjbakhche, A.H., et al., *Photont path-length distributions for transmission through optically turbid slabs.* Physical Review E, 1993. **48**(2): p. 810-818.

105. Juvela, M., *Efficient Monte Carlo methods for continuum radiative transfer.* Astronomy & Astrophysics, 2005. **440**(2): p. 531-U78.

106. Agrup, S., F. Ossler, and M. Alden, *Measurements of collisional quenching of hydrogen-atoms in an atmospheric pressure hydrogen oxygen flame by picosecond laser-induced fluorescence.* Applied Physics B-Lasers and Optics, 1995. **61**(5): p. 479-487.